

Measurements of Quarkonia with the central detectors of ALICE

Dissertation
zur Erlangung des Doktorgrades
der Naturwissenschaften

vorgelegt beim Fachbereich Physik
der Johann Wolfgang Goethe-Universität
in Frankfurt am Main

von

Wolfgang Sommer
aus Friedberg (Hessen)

Institut für Kernphysik Frankfurt

D30

26. März, 2008

vom Fachbereich Physik (13) der Johann Wolfgang Goethe-Universität als Dissertation
angenommen.

Dekan: Prof. Dr. Dirk-Hermann Rischke

Gutachter: Prof. Dr. Christoph Blume, Prof. Dr. Harald Appelshäuser

Datum der Disputation:

Zusammenfassung

Im Laufe der letzten Jahrzehnte vertiefte sich das Verständnis von der uns umgebenden Materie zunehmend. Die Weiterentwicklungen im Bereich der Hochenergiephysik erlaubten einen immer genaueren Blick auf die kleinsten Teile unserer Welt und die zwischen ihnen herrschenden Kräfte. Alle Beobachtungen und theoretischen Erklärungen verdichteten sich zu einem einfachen Schema, dem Standard Modell. Im Standard Modell können nahezu alle bisherigen Beobachtungen der Hochenergiephysik innerhalb eines Schemas aus 12 Elementarteilchen und 3 zwischen diesen Teilchen wirkenden Wechselwirkungsarten erklärt werden. Die 12 Elementarteilchen sind 6 Leptonen und 6 Quarks. Die Wechselwirkungen sind die elektromagnetische, die schwache und die starke Wechselwirkung. Jeder Wechselwirkung werden ein oder mehrere Austauschteilchen zugeordnet, das masselose Photon der elektromagnetischen, die W- und Z-Bosonen der schwachen und acht unterschiedliche Gluonen sind die Austauschteilchen der starken Wechselwirkung. Ein weiteres Boson im Standard Modell ist das Higgs-Boson, man erklärt die unterschiedlichen Massen der Elementarteilchen durch eine unterschiedlich starke Kopplung an das Higgs-Boson.

In der uns umgebenden Materie sind die Quarks fest in den Nucleonen gebunden, auf die Existenz von Quarks kann man nur durch Streuexperimente schließen. Jedoch sagt die Theorie der starken Wechselwirkung, die Quantenchromodynamik, einen Übergang von normaler, gebundener Kernmaterie zu einem Zustand quasi-freier Quarks und Gluonen voraus. In diesem Quark-Gluon-Plasma ist es möglich, dass sich Quarks und Gluonen frei innerhalb eines mehreren fm großen Bereiches bewegen. Es wird angenommen, dass ein solcher Zustand kurz nach dem Urknall existierte, das heutige Universum mit allen Nucleonen konnte erst entstehen, nachdem das Quark-Gluon-Plasma genügend abgekühlt und ausgefroren war. Demnach erhofft man sich von der Beobachtung und der Erforschung der Eigenschaften des Quark-Gluon-Plasmas Rückschlüsse auf die Entwicklung unseres Universums.

Die Erzeugung und der zweifelsfreie Nachweis des Quark-Gluon-Plasmas ist seit langem der Hauptforschungsgegenstand der Schwerionenphysik. Da das Quark-Gluon-Plasma nur eine Lebensdauer von etwa 1 fm/c hat und nur indirekt über die Ausfrierprodukte nachzuweisen ist, müssen geeignete Sonden verwendet werden, um das Quark-Gluon-Plasma zu erforschen. Diese Sonden sollten möglichst früh im Verlauf der Kollision entstehen, sensitiv auf die besondere Umgebung im Plasma sein und dann möglichst einfach nachzuweisen sein. Eine Art von Meson

erfüllt alle die eben genannten Kriterien: Quarkonium. Als Quarkonium bezeichnet man den gebundenen Zustand zweier schwerer Quarks. Leichte Quarks sind das *up*, *down* und *strange* Quark. Sie werden aufgrund ihrer relativ geringen Masse während der ganzen heißen Phase der Reaktion, und noch bis zum sogenannten chemischen Ausfrierpunkt, dem Punkt nach dem keine weitere Teilchenproduktion mehr erfolgt, produziert. Man kann also bei diesen leichten Quarks keine Aussage darüber treffen, zu welchem Zeitpunkt sie produziert wurden und demnach ist auch nicht klar, ob oder ob sie nicht von einem Quark-Gluon-Plasma beeinflusst wurden. Schwere Quarks sind das *charm*, das *beauty* und das *top* Quark. Aufgrund ihrer hohen Masse von mehr als einem GeV/c^2 können sie in einer Schwerionenkollision nur während der ersten besonders energiereichen Streuprozesse erzeugt werden. Demnach bieten die schweren Quarks einen Einblick in die ersten Augenblicke der Reaktion. Weiterhin gehen das *charm* und das *beauty*-Quark gebundene Zustände mit ihrem jeweiligen Antiteilchen ein. Diese gebundenen Zustände nennt man Quarkonium, sie sind sehr energiescharf und relativ langlebig. Weiterhin zerfallen diese Zustände zu etwa 6% in Dileptonen.

Während einer Schwerionenkollision entstehen je nach Kollisionsenergie mehrere tausend Teilchen, größtenteils Pionen und Kaonen. Elektronen und Myonen entstehen nur zu einem kleinen Prozentsatz. Leptonen kann man durch geeignete Detektoren von Pionen und anderen Hadronen relativ zuverlässig, mit hoher Effizienz trennen, demnach bietet sich über den dileptonischen Zerfallskanal eine einfache Möglichkeit Quarkonium zu messen. Ein weiterer Vorteil der Dileptonen ist, dass sie als Leptonen nicht der starken Wechselwirkung unterliegen und somit vom eventuell entstandenen Quark-Gluon-Plasma nicht beeinträchtigt werden.

Das Quarkonium selbst ist, so lange es eben noch im Plasma existiert, sensitiv auf den Zustand seiner Umgebung. Sollte während einer Kollision ein Quark-Gluon-Plasma entstehen, so bedeutet das, dass ein großer Bereich freier Quarks und Gluonen entsteht. Quarks und Gluonen tragen jeweils eine beziehungsweise zwei Farbladungen, es sind also jede Menge freier Farbladungsträger vorhanden. Diese Farbladungen können nun das bindende Potential zwischen den beiden schweren Quarks im Quarkonium abschirmen. Der Effekt ist analog der Debye-Abschirmung, die man für elektrische Ladungen beobachten kann. Die Abschirmung der Bindungspartner voneinander führt zur Aufspaltung der Bindung, das heißt, dass in einem Quark-Gluon-Plasma kein gebundenes Quarkonium existieren kann. Im Gegensatz dazu existieren in einem heißen Gas aus Nukleonen keine freien Farbladungsträger und demnach sollte Quarkonium beobachtbar sein.

Im Laufe der letzten Jahre wurden umfangreiche Messungen am SPS Beschleuniger am CERN und am RHIC in Brookhaven durchgeführt. Dabei wurde im Wesentlichen der am häufigsten auftretende Zustand des Quarkoniums, das J/ψ , gemessen. Bei mehreren durchgeführten Experimenten mit unterschiedlichen Kollisionssystemen und unterschiedlicher Kollisionsenergie konnte man ein Unterdrückung des J/ψ -Signals relativ zu einer nicht beeinträchtigten Referenzgröße beobachten. Die Stärke Unterdrückung war dabei abhängig von der Energiedichte, die während der Kollision erreicht wurde. Jedoch wurde durch eine sorgfältige

Analyse und dem Vergleich mit theoretischen Modellen klar, dass das Bild von der reinen Unterdrückung von Quarkonia nicht aufrecht erhalten werden konnte. Zum Einen wurde durch Messungen von Kollisionen in denen kein Quark-Gluon-Plasma erwartet wurde klar, dass Quarkonium zu einem gewissen Anteil auch innerhalb gebundener Kernmaterie aufgespalten wird. Zum Anderen besteht gerade bei höheren Kollisionsenergien die Möglichkeit, dass ungebundene schwere Quarks relativ spät im Verlauf der Kollision, also kurz vor dem Punkt des chemischen Ausfrierens, eine Bindung eingehen, die dann nicht mehr vom Quark-Gluon-Plasma aufgespalten wird.

Momentan existieren mehrere theoretische Modelle, die die existierenden Daten beschreiben, die jedoch die eben beschriebenen Effekte mehr oder weniger stark in Betracht ziehen. Dies führt zu unterschiedlichen Vorhersagen bezüglich der zu erwartenden Messungen am LHC. Die Messungen, die am LHC durchgeführt werden, werden also zur weiteren Verfeinerung der Modelle beitragen und damit ermöglichen über Quarkonium mehr über die Eigenschaften des Quark-Gluon-Plasmas zu erfahren.

Die vorliegenden Studien beschäftigen sich mit der Möglichkeit Quarkonia mit den zentralen Detektoren des ALICE Experimentes zu messen. ALICE ist das einzige der vier großen Experimente am LHC, das sich speziell mit Fragestellungen der Hochenergie-Schwerionenphysik beschäftigt. Das ALICE Experiment ist in zwei wesentliche Bestandteile unterteilt, dem Central Barrel und dem Muon Arm. Beide Detektorteile werden in der Lage sein, Quarkonia zu messen, das Central Barrel um die zentrale Rapidität ($|y| < 0.9$) und der Muon Arm in Rückwärtsrichtung ($-2.4 < y < -4.0$). Vor dem Muon Arm ist ein massiver Hadron-Absorber angebracht, der eine nahezu untergrundfreie Messung von Myonen ermöglicht. Das Central Barrel wurde ausgelegt, um möglichst viele verschiedene Teilchenarten von Impulsen ab 100 MeV/c zu messen. Demnach wurde bei allen Detektoren auf eine möglichst leichte Bauweise geachtet. Um elektronische Zerfälle des Quarkoniums messen zu können wurde dem Experiment der Übergangsstrahlungsdetektor (TRD) hinzugefügt, der nicht nur für die Identifikation von Elektronen verwendet wird, sondern die Impulsauflösung aller geladenen Teilchen verbessert und darüberhinaus als Triggerdetektor für Teilchen mit hohem Impuls dient. Für die Messung von Quarkonium werden insgesamt drei Detektoren des Central Barrel verwendet, das Inner Tracking System (ITS), die Time Projection Chamber (TPC) und der bereits erwähnte TRD. ITS dient zur Rekonstruktion des Primär- und eventuell vorhandener Sekundärvertices, die TPC ist der Hauptdetektor für die Spurrekonstruktion und bestimmt so hauptsächlich die Impulsmessung.

Um die erwartete Leistung des Central Barrel bezüglich der Messung von Quarkonium zu studieren, wurden die erwarteten Signale und die zu erwartenden Untergundprozesse in realistischen Raten zueinander simuliert. Dabei wurden die oben beschriebenen Effekte, die zu einer Aufspaltung von Quarkonium führen, nicht berücksichtigt, um eine von theoretischen Modellen möglichst unabhängige experimentelle Studie zu erhalten. Die vollständige Simulation eines Ereignisses im Central Barrel dauert aufgrund der hohen Teilchenzahl von bis zu 20000 gelade-

nen Teilchen pro Ereignis mehrere Stunden. Die zu erwartende Anzahl von relevanten Ereignissen wird auf 200 Millionen pro Jahr geschätzt. Anhand dieser Zahlen wird klar, dass eine vollständige Simulation aller Ereignisse nicht möglich ist. Daher wurde der langwierigste Teil der Simulationen, der Transport der Teilchen durch den Detektor, durch Parametrisierungen der Effizienz, der Auflösung und der Teilchenidentifikation ersetzt. Dadurch gelang es, die benötigte Zeit pro Ereignis von mehreren Stunden auf unter eine Sekunde zu reduzieren, so dass letztlich die volle zu erwartende Statistik für ein Jahr simuliert werden konnte.

Das Ergebnis dieser Studien ist, dass beide Quarkonium-Familien mit dem Central Barrel mit guter Signal zu Untergrund Rate ($S/B_{J/\psi} = 1.23$, $S/B_{\Upsilon} = 1.4$) und großer Signifikanz ($SGN_{J/\psi} = 274$, $SGN_{\Upsilon} = 28$) innerhalb einer Messperiode messbar sind. Ferner wurde gezeigt, dass die Massenauflösung ausreichend gut ist, um die Grundzustände des Υ von den angeregten schwereren Zuständen zu trennen. Um die Robustheit der getroffenen Aussagen zu zeigen wurden die verwendeten Anfangsparameter innerhalb der erwarteten Grenzen variiert. Die Abhängigkeit der Leistungsparameter von der Multiplizität der Ereignisse, vom elementaren Produktionsquerschnitt für Charm- und Beauty-Hadronen, und von der Güte der Elektron-Pion Separation wurde geprüft. Für keine der studierten Variationen ergab sich eine kritische Verschlechterung der Leistungsparameter, so dass anzunehmen ist, dass mit dem momentan gewählten Detektoraufbau die anvisierten Messungen nach nur einem Jahr Datennahme durchführbar sind.

Als Erweiterung zu den oben beschriebenen Studien sollte gezeigt werden, dass das momentan existierende Analyseschema ausreichend ist, um die Quarkonium Messungen durchzuführen. Dazu wurde ein Analyseprogramm entwickelt, das auf das ALICE Daten-Format (ESD) angewendet werden kann. Dazu wurden die im ESD-Format verfügbaren Möglichkeiten zur Selektion der einzelnen Teilchenspuren nach der Qualität der Rekonstruktion untersucht. Zusätzlich zu den Messungen von Quarkonium sollte ein Algorithmus zur Rekonstruktion sekundärer Vertices entwickelt werden, um eine Unterscheidung zwischen primär und sekundär produzierten J/ψ s zu ermöglichen. Sekundäre J/ψ s entstehen aus Zerfällen von B-Mesonen, aufgrund der relativ langen Lebensdauer von $c\tau \approx 500\mu\text{m}$, sollte der sekundäre Vertex deutlich vom Hauptvertex unterscheidbar sein. Die Hoffnung ist, eine Möglichkeit zur Messung des B-Quark Produktionsquerschnittes zu bekommen, die aufgrund der Einfachheit der Messung (ein über ein Elektron-Positron-Paar rekonstruiertes J/ψ mit einem deutlich vom Hauptvertex unterscheidbaren Sekundärvertex) schnell nach den ersten Datennahmen verfügbar ist. Als Unterscheidungsparameter wurde der rekonstruierte Abstand r zwischen Primär- und Sekundärvertex verwendet, als weiterer Unterscheidungsparameter wurde der minimale Abstand zwischen der rekonstruierten Fluglinie von J/ψ und dem Hauptvertex untersucht, jedoch hat dieser Parameter kaum Potential klar zwischen primärer und sekundärer J/ψ -Produktion zu unterscheiden.

Bei den beschriebenen Studien zur Rekonstruktion von sekundären J/ψ s wurde besonderes Augenmerk auf die Einflüsse des Elektron-spezifischen Energieverlustes im Detektor und von unkorrelierten Dileptonen im Untergrund gelegt. Es

wurde gezeigt, dass der spezifische Energieverlust der Elektronen durch Bremsstrahlung starke Auswirkungen, sowohl auf die Messung des Impulses, als auch auf die Bestimmung der Vertexkoordinaten hat. Beide Effekte lassen sich auf den verwendeten Rekonstruktionsalgorithmus, den Kalman-Filter zurückführen. Der Kalman-Filter ist als iterativer Algorithmus in der Lage eine Teilchenspur sowohl auf die Ungenauigkeit der Einzelmessung, als auch auf physikalische Effekte wie Vielfachstreuung zu korrigieren. Bedingung dabei ist, dass die Verteilung der Störung möglichst nahe an der Normalverteilung ist. Der Energieverlust von Elektronen wird allerdings durch die stark asymmetrische Bethe-Heitler-Verteilung beschrieben, weshalb der Algorithmus keine dementsprechende Korrektur vornehmen kann. Momentan ist es nur möglich Dileptonen aufgrund der rekonstruierten invarianten Masse zu selektieren. Verliert ein oder beide Partner Energie durch Bremsstrahlung, so weicht die rekonstruierte invariante Masse teilweise stark von der nominellen Masse des J/ψ ab, was eine Unterdrückung von Paaren mit hohem Energieverlust ermöglicht, so dass die Verlässlichkeit der Information über die Vertexkoordinaten gewährleistet ist. Allerdings wird die Effizienz der Messung dadurch um etwa 35% reduziert, so dass eine bessere Behandlung des spezifischen Energieverlustes von Elektronen versucht werden sollte.

Als weitere Quelle für Untergrund zur Messung von sekundären J/ψ s wurde der zu erwartende Anteil von unkorrelierten Leptonpaaren untersucht. Dazu wurden insgesamt 30 000 Blei-Blei Kollisionen simuliert und vollständig rekonstruiert, davon beinhalteten jeweils 10 000 Ereignisse entweder jeweils ein primäres oder sekundäres J/ψ , oder reinen Blei-Blei Untergrund. Um nun den Anteil der unkorrelierten Paare in der r -Verteilung abzuschätzen wurden die unterschiedlichen Beiträge mit gleichen Kriterien analysiert und die verbleibenden Einträge entsprechend der erwarteten Häufigkeit normiert. Demnach ist der Beitrag der unkorrelierten Lepton-Paare vergleichbar dem Beitrag von Paaren aus sekundärer J/ψ -Produktion. Allerdings ist bei diesem Ergebnis die statistische Unsicherheit aufgrund der verwendeten Normierung relativ hoch, weshalb für eine verlässliche Abschätzung eine größere Anzahl von Untergrundereignissen erforderlich wäre.

Innerhalb der hier vorliegenden Studien wurden also zwei wichtige Punkte bezüglich der zu erwartenden Messungen von Quarkonium behandelt: Die prinzipielle Möglichkeit und die zu erwartende Signifikanz der Quarkonium-Messungen im ALICE Central Barrel und als zweiter Punkt die Möglichkeit mit dem vorhandenen ALICE Software und Analyse-Paket, die Messung durchzuführen und darüberhinaus primäre von sekundärer J/ψ -Produktion mit Hilfe der Zerfalls-Topologie zu unterscheiden.

Contents

1	Introduction	1
1.1	Forces and particles in the standard model	1
1.2	Heavy ion collisions	3
2	Quarkonia measurements in heavy ion collisions	7
2.1	The discovery of quarkonia	7
2.2	Quarkonia production	9
2.3	Quarkonia in hot quark matter	11
2.4	Experimental status	14
2.4.1	SPS measurements	16
2.4.2	RHIC measurements	19
2.4.3	Theoretical interpretation	22
3	Heavy Ion Collisions at the Large Hadron Collider	27
3.1	The Large Hadron Collider: LHC	27
3.2	A Large Ion Collider Experiment: ALICE	28
3.3	The central barrel	31
3.3.1	Inner Tracking System – ITS	31
3.3.2	Time Projection Chamber – TPC	32
3.3.3	Transition Radiation Detector – TRD	36
3.3.4	Trigger and data acquisition	41
4	Quarkonia measurements with the ALICE central barrel	45
4.1	Simulation framework	45
4.2	Expected quarkonia yields	46
4.3	Event cocktail	52
4.4	Evaluation of the detector performance	54
4.5	Quarkonia acceptance	61
4.6	Quarkonia performance	61
4.6.1	Dielectron analysis	61
4.6.2	Invariant mass spectrum	62
4.6.3	Background estimation	63
4.6.4	Performance of the quarkonia measurements	66

4.6.5	Transverse momentum dependent J/ψ production	68
4.6.6	Multiplicity dependence	71
4.6.7	Influence of the TRD electron identification	71
4.6.8	Dependence on elementary charm and beauty production cross section	73
4.7	Suppression and enhancement	74
5	Analysis of primary and secondary J/ψ's with ALICE	77
5.1	Idea of the analysis	77
5.2	ALICE analysis framework	78
5.3	Data samples	80
5.4	Track quality cuts	81
5.5	Physics cuts	87
5.5.1	Transverse momentum cut	87
5.5.2	Particle identification	89
5.5.3	Topological cuts	91
5.6	Reconstruction of secondary J/ψ 's	93
5.6.1	Secondary vertex determination	94
5.6.2	Primary – secondary J/ψ separation using r and b	95
5.6.3	Impact of the electron energy loss	97
5.6.4	Impact of the uncorrelated background in lead-lead collisions	99
5.7	Conclusion	103
6	Summary and outlook	107
A	Kinematic variables in heavy-ion collisions	109
B	TRD production in Frankfurt	113
B.1	TRD readout chamber production	113
B.2	TRD pad plane production	119
	Bibliography	125

Chapter 1

Introduction

1.1 Forces and particles in the standard model

During the last decades huge progress has been made on the understanding of the fundamental forces and building blocks of the universe. All observations and theoretical approaches condensed into a relatively easy and beautiful theory called the Standard Model. In this model the large variety of our surrounding nature is reduced to sixteen elementary particles (see table 1.1) and three forces determining the interplay between these particles. The three forces are the strong force, the weak force and the electromagnetic force. The gravitation is often quoted as the fourth force, although it could not be described within the Standard Model. The interaction between elementary particles can be described as the exchange of bosons, according to this picture each fundamental force is associated with one or more exchange-boson. The electromagnetic force is mediated by the photons and the weak force by the experimentally found W^\pm and Z^0 -Bosons [Arn83, Ban83]. Eight gluons are the exchange bosons for the strong interaction. Postulated, but so far not seen is the Higgs-Boson, creating the masses of the elementary particles. The Higgs mechanism describes the creation of mass as coupling to the Higgs-Boson. Although it cannot explain the large mass differences between the elementary particles ($m_u \approx 3 \text{ MeV}/c^2$ compared to $m_t \approx 186 \text{ GeV}/c^2$), the detection of the Higgs-Boson is seen as a strong confirmation of the Standard Model and one of the reasons to build a new collider, the Large Hadron Collider at CERN, exceeding the highest collision energies by a factor of 7.

The description of the electromagnetic and the weak force is done within the so-called electro-weak theory, unifying the electromagnetic and the weak forces. The theory describing the strong interaction is Quantum-Chromo-Dynamics (QCD), reflecting the fact that the charge of the quarks and gluons is called color charge. Large efforts have been made to unify the strong with the electroweak interaction to a Grand Unified Theory, describing all Standard Model interactions within one framework. Until now a commonly accepted description could not be found.

The coupling constant α_S of the strong interaction depends on the momentum

Table 1.1: Elementary particles in the standard model. The interaction between these particles is described by the exchange of bosons.

Elementary particles				Interactions	Bosons
	Flavor				
Quarks	up	charm	top	strong weak electromagnetic	8 gluons Z, W [±] γ
	down	strange	bottom		
Leptons	ν_e	ν_μ	ν_τ		
	e	μ	τ		

transfer in a specific collision. α_S is close to or even larger than one for small momentum transfers and small or close to zero for momentum transfers $Q^2 \gtrsim 2 \text{ GeV}/c^2$. For this reason perturbation theory can only be applied to processes with large momentum transfers, for soft processes perturbative calculations cannot be performed.

A unique feature of Quantum-Chromo-Dynamics is that the gluons are not only the mediators between the quarks, but since each gluon carries one color and one anti-color charge, they interact strongly with each other. This self-interaction of the gluons is seen as the reason for confinement. Confinement denotes the fact that quarks cannot be observed as free particles. As a consequence of the gluon-gluon interaction and in contrast to the other forces like the electromagnetic force or the gravitation the energy to separate two quarks from each other is not decreasing with increasing distance but linearly increasing. This means that with increasing quark distance more and more energy is stored in the system. At some point the stored energy is high enough to create a new quark-antiquark pair. The created quark and antiquark now bind to the initial quarks and thus instead of two individual quarks two mesons are produced. For this reason individual quarks have never been observed, the existence of quarks can only be confirmed indirectly in scattering experiments.

Nevertheless it is possible to observe quarks in quasi-free states. Within a nucleon or other bound hadrons the influence of the strong interaction on the individual quarks is small. Therefore quarks act, within a hadron, like free particles. Only when the distance between the quarks increases by more than the size of a hadron ($\sim 1 \text{ fm}$), confinement sets in and the quarks are bound by the strong interaction.

If nuclear matter is either heated up, or its density is increased, QCD calculations predict a transition between confined hadrons and deconfined quarks and gluons. Within the deconfined volume quarks and gluons are quasi-free. Due to the presence of free color charges, the deconfined matter is called Quark-Gluon-Plasma (QGP) [Shu78]. Lattice QCD calculation predict a transition line (see figure 1.1) between hadronic and deconfined matter. The transition depends on the temperature T and the baryon density (baryo-chemical potential μ_B).

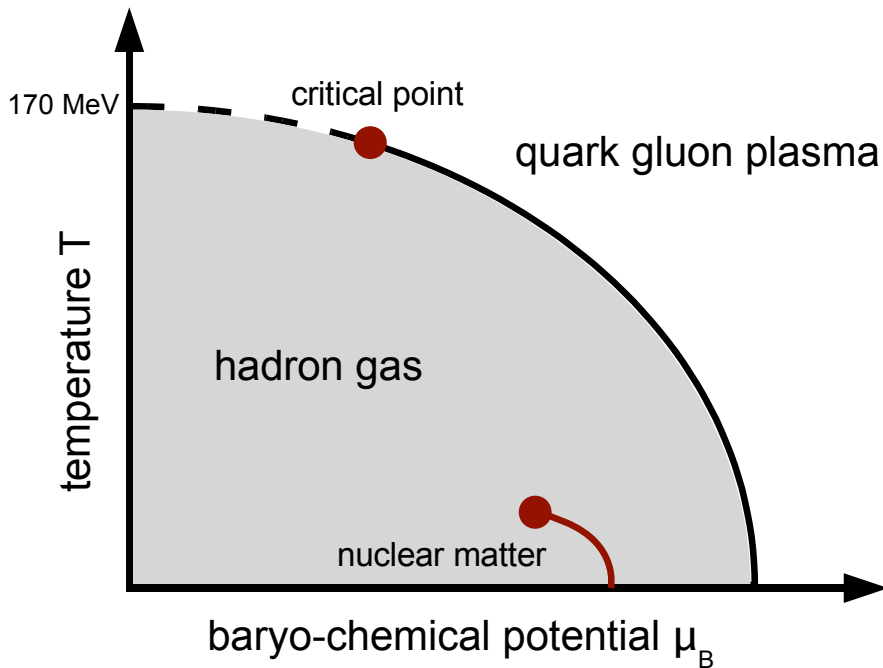


Figure 1.1: A sketch of the QCD phase diagram in the plane of temperature T and brayo-chemical potential μ_B . The transition line between the deconfined and the hadronic phase as predicted from lattice QCD is shown [Kar95, All03], ending in a critical point [Fod01]. The critical temperature of 170 ± 20 MeV ($\mu_B = 0$) is also predicted by lattice QCD [Sus79, Kut80].

According to cosmological models a QGP was formed shortly after the Big Bang. Thus our universe can be seen as a freeze-out product of a large QCD-plasma. Therefore the distribution of matter in the universe, as the basis for the formation of galaxies and stars, is determined by the characteristics of the QGP.

As it will be shown later (see chapter 2.4) strong indications have been found in experiments at the SPS and RHIC that a Quark-Gluon-Plasma is produced in heavy-ion collisions. With the startup of the Large Hadron Collider – LHC – with its unprecedented collision energy of 5.5 TeV per nucleon pair in heavy-ion collisions – which is roughly a factor of 30 larger than the highest achievable collision energies at former accelerator experiments – the Quark-Gluon-Plasma will be explored using a large variety of observables.

1.2 Heavy ion collisions

To verify the existence of the phase transition and to prove the formation of the Quark-Gluon-Plasma within heavy-ion collisions, physical observables have to be

identified, providing information on the state of the produced medium. In general one divides these probes into two groups: soft probes and hard probes. Hard probes denote processes with high momentum transfers. These processes happen only during the early stages of the collisions. Due to the high momentum transfers the cross sections can be calculated in perturbative QCD (pQCD). The scattering products are influenced by the traversed medium, thus they carry information on the physical properties of the medium. The following probes are regarded as hard probes:

- Quarkonia production: The production of quarkonia¹ can be described in pQCD (see section 2.2). Due to Debye-screening in the deconfined medium the produced state is split up depending on the temperature of the surrounding medium.
- High- p_T particles: High- p_T particles are produced in primordial $q\bar{q}$, gg or qq reactions with high momentum transfer. Due to the hot and dense QCD-medium these particles are attenuated by gluonic bremsstrahlung ($q + q \rightarrow q + q + g$), resulting in a high- p_T suppression.

A variant of this is the suppression of dijets. Two quarks or gluons are produced in a hard collision, one of them leaves the medium directly, the other one has to traverse the whole medium and is thus attenuated. The undisturbed parton hadronizes and forms a jet, the other one is absorbed in the Quark-Gluon-Plasma and is, for this reason not detected. (see [Adc01, Adl02, Adl03])

The soft probes arise from processes happening at later production stages. At these stages no more hard processes take place, the average momentum transfer is low. Thus the cross sections of these probes cannot be calculated in a perturbative approach. The information on the medium is not carried by single particles, but by the bulk properties of all particles created in the collision. According to their subsequent formation the following soft probes can be observed:

- Directed and elliptic flow. Flow denotes the observed anisotropies in particle emission. The anisotropies reflect the initial collision geometry. Hydrodynamical models showed that the elliptic flow can be sensitive to a phase transition.
- Relative particle abundances. Relative yields of particles are fixed at the so-called *chemical freeze-out*². The ratio between the different particle species is determined by the freeze-of temperature and baryon density, thus the particle abundances carry information on these two quantities.
- Fluctuations. If the conditions within the heavy-ion collisions are such that the state of the produced matter is close to the critical point, the hadron multiplicity is expected to fluctuate heavily from one event to another.

¹Bound state of two heavy quarks, see chapter 2

²Chemical freeze-out denotes the point in a heavy-ion collisions, where no further particles are produced and the relative abundances of particles remain constant.

- Particle correlations. Particles emitted from the point of *kinetic freeze-out*³ undergo quantum mechanical interference effects and therefore reveal information on the space-time evolution of the collision zone.

Historically the accessible probes were determined by the energy of the collision. Especially hard probes are only produced in measurable quantities at higher collider energy. Consequently the study of the hard probes started at the SPS⁴ with a collision energy of $\sqrt{s_{NN}} = 17$ GeV with detailed studies on charmonium ($c\bar{c}$) suppression. The RHIC⁵ increased the collision energy to $\sqrt{s_{NN}} = 200$ GeV and enabled especially the measurement on high- p_T suppression. With the further increase of the collision energy at the Large Hadron Collider to $\sqrt{s_{NN}} = 5500$ GeV in lead-lead collisions, hard probes will be abundantly produced and for the first time the bottomonium ($b\bar{b}$) is produced in sufficiently high statistics.

³Kinetic freeze-out denotes the phase of a heavy-ion collision where the produced particles do not interact any more, and for this reason do not change their kinematics.

⁴Super-Proton-Synchrotron

⁵Relativistic-Heavy-Ion-Collider

Chapter 2

Quarkonia measurements in heavy ion collisions

2.1 The discovery of quarkonia

In November 1974 a narrow resonance at $3.1 \text{ GeV}/c^2$ in the $\mu^+\mu^-$ invariant mass spectrum was observed [Aug74, Aub74] in proton-beryllium and electron-positron collisions. The particle was named J/ψ . At that time the world was expected to consist of up, down and strange quarks plus electrons and muons. In addition a fourth quark was predicted by the GIM mechanism¹. Soon after the first observation it became clear that the newly discovered particle consisted of the predicted quark species, the so called charm quarks. This discovery added a new particle to the fundamental building blocks of nature. In addition the description of the small width of the observed peak, $93.4 \pm 1.2 \text{ keV}$ [Yao06], was one of the first big successes of Quantum-Chromo-Dynamics (QCD), a theory still relatively new at that time.

Three years later another sharp resonance in the dimuon² spectrum was discovered in proton-nucleus collisions [Her77], the Υ . This time the surprise in the physics community was not as large since the third lepton, the τ , was discovered in the mean-time and for symmetry reasons one expected a third quark family.

The heaviest quark, the top quark, was discovered in 1995 [Abe95]. This discovery completed the three quark families. Up, down and strange quarks are commonly called light quarks, while the charm, bottom and top are referred to as heavy quarks. The bound state of these heavy quarks with their corresponding anti-particle is called quarkonia. The top quark cannot form a bound state, due

¹ The branching ratio of $K^0 \rightarrow \mu^+\mu^-$ observed as $\Gamma(K^0 \rightarrow \mu^+\mu^-)/\Gamma(K^0) \simeq 10^{-7}$ was smaller than expected from theoretical models around 1970. The Glashow-Iliopoulos-Maiani (GIM) mechanism [Gla70a] describes the decay as the destructive interference between two indistinguishable decay channels. The destructive interference explains the small branching ratio. The additional decay channel implied the existence of a fourth quark.

²Dimuon spectrum denotes the invariant mass spectrum of muons and anti-muons. In general the combination of two leptons is called dilepton.

to its short lifetime of less than 10^{-24} s.

A heavy quark-anti-quark pair is able to form more than one bound state. Apart from the J/ψ and the Υ more higher excited states exist, forming the so-called J/ψ and Υ families. The description of the observed term schemes (figure 2.1 and 2.2) is another validation of QCD.

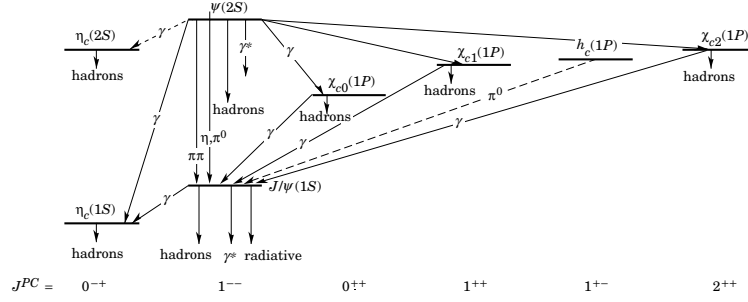


Figure 2.1: Term scheme of the J/ψ family [Yao06].

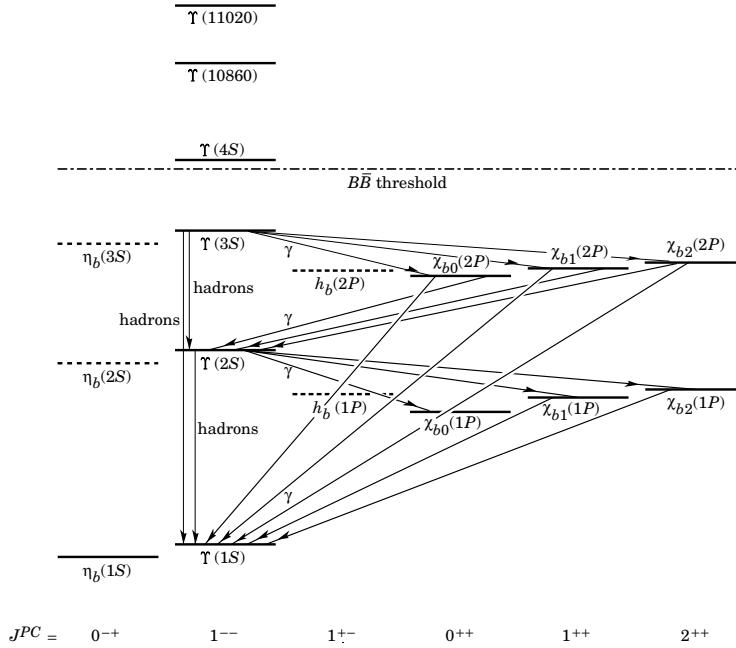


Figure 2.2: Term scheme of the Υ family [Yao06].

Given the mass of the charm quark of $1.3 \text{ GeV}/c^2$ and the QCD coupling constant $\alpha_{QCD} = 0.3$, the system can be studied in a simplistic non-relativistic approach starting from the Schrödinger equation for the charm-anti-charm system

$$\left(2m_c - \frac{1}{m_c} \nabla^2 + V(r)\right) \Phi_i(r) = M_i \Phi_i(r) \quad (2.1)$$

with a simple approach for the binding potential

$$V(r) = \sigma r - \frac{\alpha}{r}. \quad (2.2)$$

This so called *Cornell* potential was proposed in [Eic78, Eic80]. It consists of a Coulomb like term proportional to $\frac{\alpha}{r}$ with r being the distance between the quarks, $\alpha = \alpha_{QCD}$ and a linear term accounting for the specific feature of QCD that with increasing distance the potential energy also increases. σ denotes the so-called string tension, measured as 0.16 GeV^2 . Using this potential and the uncertainty principle $\langle p^2 \rangle \langle r^2 \rangle \simeq 1$ one can determine the energy of the bound states to be:

$$E(r) \simeq 2m_c + \frac{1}{m_c r^2} + \sigma r - \frac{\alpha_{QCD}}{r} \quad (2.3)$$

Minimizing $E(r)$ with respect to r gives the radius of the ground state:

$$\frac{dE(r_0)}{dr} \stackrel{!}{=} 0 = -\frac{2}{m r_0^3} + \sigma + \frac{\alpha}{r_0} \quad (2.4)$$

With $\alpha_{QCD} = 0.3$ and $\sigma = 0.16 \text{ GeV}^2$ and the charm quark mass $m_c = 1.3 \text{ GeV}/c^2$, one obtains the radius of the ground state $r_0 = 0.36 \text{ fm}$. With this radius the mass of the ground state is calculated as $M_0 = E(r_0) = 2.95 \text{ GeV}/c^2$ close to the measured mass of $3.096 \text{ GeV}/c^2$.

More detailed models, including non-relativistic potential theory, calculate the mass, the binding energy ($\Delta E = 2m_{D,B} - M_0$) and the radius of different quarkonia states (table 2.1). In addition the difference between the theoretical mass and the measured mass is given (ΔM).

Table 2.1: Radius, mass and binding energy of quarkonia calculated with a non-relativistic theory [Sat06a].

state	J/ψ	ψ'	Υ	Υ'	Υ''
mass [GeV/c^2]	3.10	3.68	9.46	10.02	10.36
ΔE [GeV]	0.64	0.05	1.10	0.54	0.20
radius [fm]	0.25	0.45	0.14	0.28	0.39
ΔM [GeV/c^2]	0.02	0.03	0.06	-0.06	-0.07

2.2 Quarkonia production

Now that the discovery and some of the characteristics of quarkonia have been discussed, the production of quarkonia shall be described. We will especially focus on predictions for production cross sections at LHC energies. These predictions are later used as an input to the presented simulations. In general one can subdivide the production process into two major parts:

1. Production of a heavy quark pair in hard collisions
2. Formation of quarkonia out of the two heavy quarks

Due to the high mass of the heavy quarks ($m_{charm} \simeq 1.3 \text{ GeV}/c^2$, $m_{bottom} \simeq 4.7 \text{ GeV}/c^2$) the first process can happen only during the first phase of a collision. Only at that time the elementary collisions with sufficiently high momentum transfers to create such high masses take place. For this reason the heavy quark production is a hard process that can be treated perturbatively. In next-to-leading order (NLO) calculations the available experimental data at different energies and collision system [Bai06] [Vog04] were described. The obtained parameters were then used to predict the total production cross section in proton-proton collisions at LHC energies. The charm production cross section is predicted to be 6.3 mb and the bottom production cross section 0.19 mb [Vog01]. To obtain upper and lower limits for this cross sections the parameters have been varied leading to a relatively large range for the charm production cross section of 4-15 mb and 0.08-0.34 mb for the bottom production cross section.

The second part, namely the formation of quarkonia out of the quark-anti-quark pair can a priori not be treated perturbative. Due to the high quark masses and the small relative velocities in the quarkonium system, the formation can be described using non-relativistic QCD (NRQCD). This allows the factorization into a perturbative small-range and high-momentum part and a long-ranged and low-momentum part. In the past years especially three models were developed, namely the Color Singlet Model (CSM) [Ber80, Cac96], the Color Octet Model [Bra94, Cho95a, Cho95b] and the Color Evaporation Model (CEM) [Fri77, Amu95, Amu96].

The quarkonia formed out of the two quarks has to be color neutral. Since in principal the two heavy quarks are not necessarily carriers of one color and the corresponding anti-color, the combination might be colored³. The Color Singlet Model rejects all color octet states, in the NRQCD factorization the produced quarkonium has the same quantum numbers as the quark-anti-quark pair. Predictions by the CSM for the production of quarkonium in $p\bar{p}$ at Tevatron underestimated the data by an order of magnitude, thus it was clear that the color octet states cannot be neglected.

The Color Octet model considers the octet states, within the model quarkonium is only produced in an octet and thus colored state. The pre-resonant colored state neutralizes its color by the emission of a soft gluon. The Color Octet Model was able to reproduce the production cross section but failed in the description of the observed J/ψ polarization [Aff00].

³The symmetry group of QCD is the SU(3). The fundamental description of this group are the color triplets R , G , B and their adjunct descriptors \bar{R} , \bar{G} , \bar{B} . Out of these triplets one can form $3 \otimes 3 = 8 \oplus 1$ combinations, one octet and one singlet. The colored octet states are: $R\bar{G}$, $R\bar{B}$, $G\bar{R}$, $G\bar{B}$, $B\bar{R}$, $B\bar{G}$, $\sqrt{\frac{1}{2}}(R\bar{R} - G\bar{G})$, $\sqrt{\frac{1}{6}}(R\bar{R} + G\bar{G} - 2B\bar{B})$. The color neutral singlet is: $\sqrt{\frac{1}{3}}(R\bar{R} + G\bar{G} + B\bar{B})$.

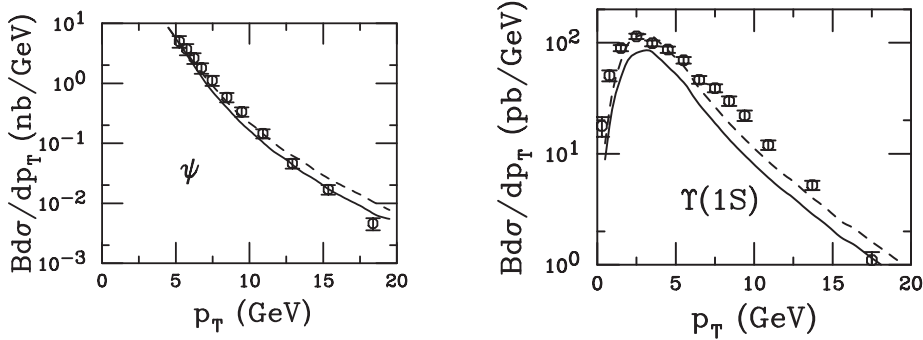


Figure 2.3: p_T -dependent production of J/ψ and Υ s as measured by the CDF experiment [Abe97a, Abe97b, Aco01] (circles) and compared to predictions by the Color Evaporation Model with two different parameter sets (solid+dotted).

As an expansion the Color Evaporation Model was developed from the Color Octet Model. The *evaporation* of the surplus color happens via many different processes, not only by the emission of a soft gluon. This large number of processes results in a relatively large number of parameters, that have to be determined by the comparison to existing data. Although the tuning of the model to the data works well (see figure 2.3), the large number of free parameters limit the predictive power of the CEM. Nevertheless it is the best available approach for describing the available measurements and it is used for the predictions of the cross sections for LHC energies.

In this approach the parameter sets matching the CDF data are taken to extrapolate the cross sections to LHC energy of 14 TeV (pp) and 5.5 TeV/A (PbPb). The resulting cross sections as they will be further used in this thesis are given in table 2.2. The production cross sections include two effects, that have not been discussed so far: the expected feed-down and the branching ratio into dielectrons. Feed-down denotes the effect that the observed cross section of, for example of the J/ψ , is a composite of directly produced J/ψ s and J/ψ s originating from decays of heavier particles (e.g. $B_0^s \rightarrow J/\psi + \pi^0$). Since quarkonia are usually measured via the decay to dileptons, the probability to decay into dielectrons, or dielectron branching ratio, is included. Although uncertainties are not given at this point one should keep in mind that these production cross sections vary as much as the elementary charm-anti-charm and bottom-anti-bottom production cross sections.

2.3 Quarkonia in hot quark matter

In 1986 for the first time quarkonia were suggested to be used as a probe for the matter created in heavy-ion collisions [Mat86]. One can distinguish two different scenarios for the created matter. The first scenario assumes that the energy density was not sufficient to dissolve the hadrons, contained in the colliding nuclei, this

Table 2.2: Predictions for the cross sections for quarkonia at the LHC by the CEM. The cross sections include the branching into dielectrons as well as feed down from higher states. All numbers are given in μb [Ale06b].

System	\sqrt{s}	J/ψ	ψ'	Υ	Υ'	Υ''
proton-proton	14 TeV	3.18	0.057	0.02	0.005	0.003
proton-proton	5.5 TeV	1.83	0.033	0.009	0.002	0.0013
lead-lead	5.5 TeV	48930	879	304	78.8	44.4

scenario is called the *hadron gas*, since the system is expected to behave similar to an hot gas. The second scenario is the so-called Quark-Gluon-Plasma, here the energy density is large enough to dissolve the hadrons and a relatively large zone of free quarks and gluons is created, similar to an electromagnetic plasma containing free electrons and ions. The aim is to find a probe which is sensitive to the surrounding matter. The measurement of quarkonia production is seen as an almost ideal probe for three reasons: Quarkonia are, due to the high quark masses, produced within the first stages of the collision, such that the initial production is not affected by the produced medium. The second reason is that some quarkonia states have a rather large probability to decay into dileptons, which do not interact strongly and are thus not modified by the medium they traverse. And the third and dominant reason is that quarkonia are expected to be highly sensitive on whether the surrounding medium consists of deconfined matter or not, which is described in the following.

A hadron gas is, since it consists of hadrons, color neutral and one would expect quarkonia to be produced in a comparable way as observed in proton-proton or proton-nucleus collisions. The dominant interactions between produced quarkonia and the medium would be scattering off nucleons and pions. These scattering processes can lead to the dissociation of the quarkonium state. Since the cross sections of these processes are hardly known and also the theoretical predictions range from 0.1 to 8 mb, the effect of these processes has to be evaluated by comparison to collisions of smaller systems and extrapolation to heavy-ion collisions. All of these effects are usually called Cold-Nuclear-Matter effects.

Assuming that a Quark-Gluon-Plasma was created means that the hadrons melt and deconfined quarks and gluons are able to move freely within a volume of a few fm^3 . This medium is not color neutral, since a lot of free color charges exist, it is a color conductor. For this reason one expects similar effects to the ones observed within an electromagnetic plasma: due to the existence of free charge carriers the potential between two charges gets screened and thus any binding is weakened or split. Analogous to a Coloumb potential where this effect is called Debye screening

the previously mentioned Cornell potential (2.3) of the form

$$V(r) = \sigma r - \frac{\alpha}{r} \quad (2.5)$$

is modified to

$$V(r) = \sigma r_D \left\{ \frac{1 - e^{-\frac{r}{r_D}}}{\frac{r}{r_D}} \right\} - \frac{\alpha}{r} e^{-\frac{r}{r_D}} \quad (2.6)$$

with r_D as Debye screening radius. The value of this radius depends on the temperature of the produced system. Qualitatively one could say that as soon as the DeBroglie wave-length of a charge carrier ($\lambda = \frac{h}{p}$) is comparable to the radius of the bound object, the potential gets screened and the binding starts to break up. The wave-length of the charge carriers depends on the average kinetic energy and thus on the temperature of the medium. More quantitative approaches study the screening in lattice calculations [Dig01]. In these calculations a different approach for the potential is used:

$$V(r, T) = U(r, T) = F(r, T) - T(\partial F/\partial T) \simeq F(r, T) \quad (2.7)$$

With $U(r, T)$ as the internal energy of a $Q\bar{Q}$ pair, $F(r, T)$ as the free quark energy and $-T(\partial F/\partial T)$ as entropy term, for which lattice calculations suggest that it can be neglected. Using this approach the corresponding Schrödinger equation can be solved. The results are shown in figure 2.4. By increasing the temperature of the surrounding medium the slope of the linear part of the free quark energy decreases and the radius of the bound states increases until no more bound states exist.

As already shown in table 2.1 the radius of the various quarkonia states is inverse proportional to the binding energy – weakly bound states have a large radius and vice versa. Given the dependence of the screening radius on the temperature of the medium, one expects the various quarkonia states to melt depending on the temperature of the medium. Indeed lattice calculations [Kar05] imply that different quarkonia states melt at different temperatures. In this respect the measurement of the individual states is referred to as a *QCD thermometer*. The calculated quarkonium dissociation temperatures with respect to the critical temperature are shown in table 2.3.

Table 2.3: Quarkonium dissociation temperatures T_d with respect to the critical temperature T_c [Dig06].

state	J/ψ	χ_c	ψ'	Υ	χ_b	Υ'	χ_b'	Υ''
T_d/T_c	2.10	1.16	1.12	>4.0	1.76	1.60	1.19	1.17

From this table one can see that except from the ground states, J/ψ and Υ , the quarkonia states vanish at temperatures close to the critical temperature. Since the total cross section of the quarkonia ground state consists of the production of the ground state plus the feed-down from the decay of heavier quarkonia, the measured

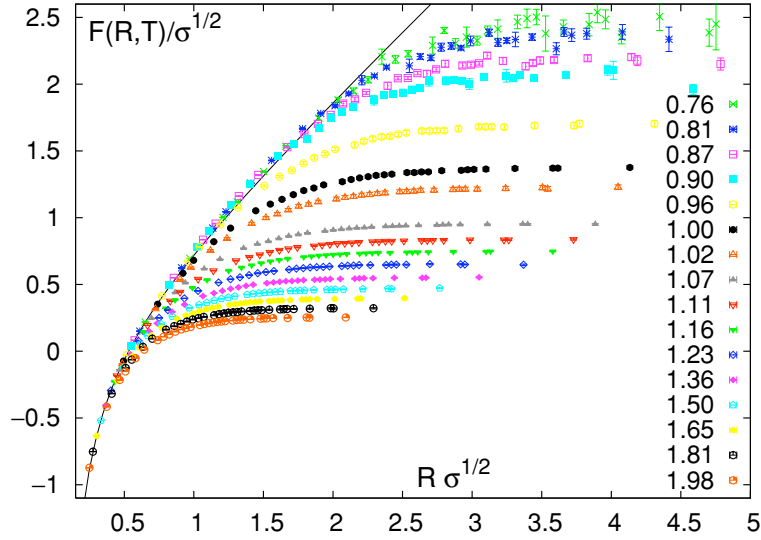


Figure 2.4: The free quark energy $F(R, T)$ versus the distance times the string tension between the quarks $R \sigma^{1/2}$ for different temperatures. The slope of the linear part of the potential decreases with increasing temperature and thus reflects the expected screening of the two heavy quarks by the existence of free color charge carriers [Kac03].

cross section of the ground state is affected as soon as the higher excited states are affected by the plasma.

Another effect that can influence quarkonia production in heavy-ion collisions, is the recombination of individually produced charm and anti-charm quarks. Due to the large yield of about 100 $c\bar{c}$ pairs, produced in one central lead-lead event at the LHC, there is a certain probability that charm quarks form quarkonia at the last stage of the collision, were the temperature drops below the critical one and the hadrons freeze-out (chemical freeze-out). This effect will be discussed in more detail in section 2.4.3.

2.4 Experimental status

Currently measurements of quarkonium in heavy-ion collisions are only available for the lighter $c\bar{c}$ systems J/ψ and ψ' . Production cross sections for $b\bar{b}$ states could not be measured since the collision energy at available colliders was not sufficient to produce these states in measurable quantities. Only one attempt was made to measure Υ 's at the STAR experiment using the High Level Trigger system to enhance the rate of measured Υ 's [Kol06]. This situation will change significantly with the start-up of the LHC. For comparison the expected yields per central collision of $c\bar{c}$ and $b\bar{b}$ at SPS, RHIC and LHC are given in table 2.4. This yield is proportional to the amount of produced quarkonia, thus one can expect to detect

Table 2.4: Number of heavy quark-anti-quark pairs per central collision ($b=0$) for SPS, RHIC and LHC energies.

	SPS $\sqrt{s}=17$ AGeV	RHIC $\sqrt{s}=200$ AGeV	LHC $\sqrt{s}=5500$ AGeV
$N_{c\bar{c}}$ ($b=0$)	0.2	10	120
$N_{b\bar{b}}$ ($b=0$)	—	0.05	5

Υ 's in a similar way as J/ψ 's at RHIC.

The aim is to observe a suppression that can be interpreted as a result of quarkonium dissociation in the deconfined medium. Since the amount of deconfined matter should be proportional to the energy density of the produced system, a suppression should be visible with respect to a quantity representing the energy density. Most of the measurements relate the quarkonium production with either the number of participants N_{part} or with a parameter L , representing the length of the way from the parton collision point through the nuclear matter. Both quantities can be determined via Glauber model calculations (see section 4.2) and reflect the energy density achieved in the collision.

To observe a deviation a reference process defining the *normal* or expected behaviour has to be chosen. Basically there are two different approaches for this reference process: The first approach relates the observed quarkonia production to a different process measured simultaneously. An example is the Drell-Yan process ($q\bar{q} \rightarrow l^+l^-$) as it is used as a reference at the SPS experiments. The Drell-Yan process is a hard process, meaning that it includes large momentum transfers of more than 1 GeV/c. The necessary momentum transfers only take place during the first phases of the collision, thus the cross section of the Drell-Yan process is expected to scale with the number of initial binary collisions. Since the Drell-Yan process is in addition expected not to be affected by a deconfined medium, the ratio between the two processes shall be constant if the charmonium production is not affected by the medium. If charmonium production is affected, the ratio is expected to decrease with increasing centrality.

The second approach, followed at RHIC, reflects the general question underlying any heavy-ion research: How do the observations change when comparing binary proton-proton collisions to the collision of two nuclei? A naive model would predict, that the cross sections for hard processes of two colliding nuclei A and B can be described as $A \times B$ proton-proton collisions. More refined models include the geometry of the colliding nuclei and use the number of collisions as a scaling variable. For charmonium production the nuclear modification factor is defined:

$$R_{AA} = \frac{\frac{dN_{AA}^{J/\psi}}{dydp_T}}{\langle N_{coll} \rangle \cdot \frac{dN_{pp}^{J/\psi}}{dydp_T}} \quad (2.8)$$

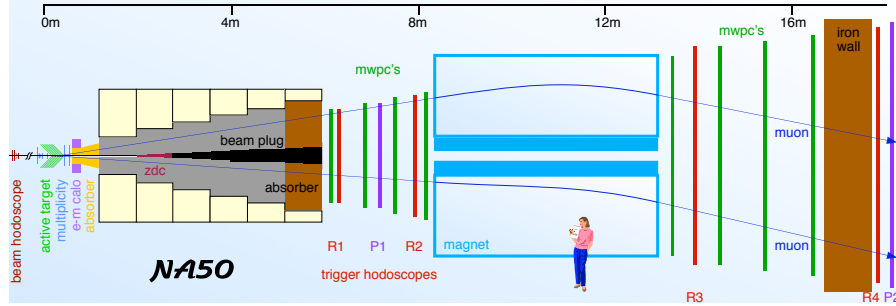


Figure 2.5: Setup of the NA50 experiment located in the north area of CERN. The spectrometer consists of a target region, a hadron absorber to remove almost all hadronic background, a dipole magnet to bend the muon tracks and of course trigger and tracking chambers for muons. The setup of the NA60 experiment is almost identical the most important change was the installation of a silicon pixel detector in front of the absorber.

It denotes the ratio of J/ψ production in nuclear collisions $dN_{AA}^{J/\psi}$ and proton-proton collisions $dN_{pp}^{J/\psi}$. The proton-proton yield is scaled by the averaged number of collisions $\langle N_{coll} \rangle$ estimated by Glauber model calculations [Gla87]. By definition if no nuclear modification, meaning no medium effect, is present, one expects $R_{AA} = 1$. Any deviation from one can then be attributed to the produced medium.

The existing experimental status of J/ψ and ψ' shall be described in the following. The measurements performed by the three fixed target experiments NA38 [Hug92], NA50 [Abr91] and NA60 [Bal00] and the measurements of the collider experiment PHENIX [Adc03] are briefly described and the most prominent theoretical models and their possible implications for the LHC will be discussed.

2.4.1 SPS measurements

Charmonium production in heavy-ion collisions has been measured at the SPS at three experiments, NA38, NA50 and NA60, over a period starting from 1986 (NA38) until today (NA60). All of the three experiments are designed to measure charmonium via its dimuon decay channel. Since NA50 is the successor of NA38 and NA60 the successor of NA50, the experimental setups are very similar (even the NA38 muon spectrometer was inherited from NA10). In figure (2.5) the setup of the NA50 detector is shown.

The main parts of the original NA38 experiment are a hadron absorber, to suppress any non-muonic background, a toroid magnet for momentum measurement, a muon trigger in front of the magnet and tracking chambers behind. For the NA50 experiment a Zero-Degree-Calorimeter (ZDC) inside and in front of the absorber

an electromagnetic calorimeter were added to improve the selection on centrality. With the transition to the NA60 experiment a silicon pixel detector was installed in front of the absorber to enable a precise measurement of the interaction vertex (resolution $200 \mu\text{m}$ in z and $20 \mu\text{m}$ in xy -direction). Finally a vacuum target cell was added to suppress beam gas interactions which could be mistaken as peripheral collisions.

1989 a J/ψ suppression was reported by the NA38 experiment [Bag90]: Here oxygen-uranium (O-U) collisions with an incident energy of the oxygen beam of 200 GeV per nucleon, resulting in a collisions energy of $\sqrt{s} = 20$ GeV per nucleon were examined. Figure 2.6 shows the measured J/ψ yield normalized to the number of dimuons in the mass region $m=2.7\text{-}3.5 \text{ GeV}/c^2$ as a function of the measured transverse energy (E_T) as a measure for centrality.

A similar pattern was observed later in sulphur-uranium (S-U) collisions [Bag91]. In the picture of charmonium dissociation one would expect this ratio to remain constant with centrality if charmonium is not suppressed. With increasing centrality, the nuclear matter is more and more compressed, at some point a volume of deconfined matter forms, containing free color charges. Due to these charges the charmonium binding potential is screened and the bound state is dissolved and the measured J/ψ production decreases with respect to the reference process.

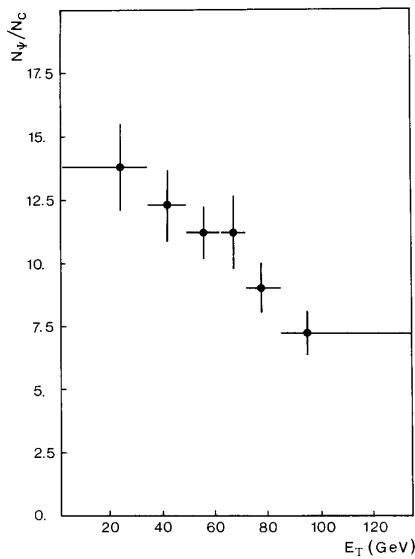


Figure 2.6: The evolution of the ratio of produced J/ψ s and produced dimuons as a function of the transverse energy as measured by NA38 [Bag90].

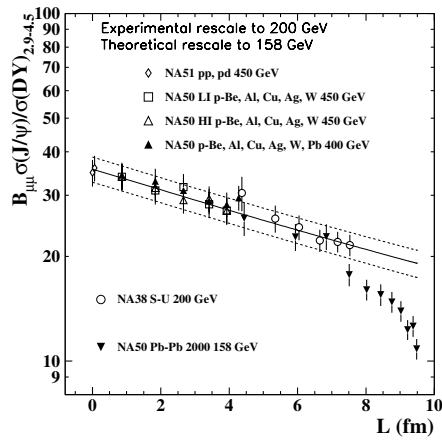


Figure 2.7: The J/ψ suppression pattern as measured by the NA50 experiment [Ale04]. The solid line indicates the *normal* nuclear absorption as expected from comparison to proton nucleus data. A clear *anomalous* suppression is observed for $L > 7.5$ fm.

Not only the dissociation due to deconfined matter is able to explain the decreasing charmonium production, also charmonium can be dissolved due to inter-

actions with nucleons. As pointed out in [Kha96] the observed suppression can be explained by the breakup of charmonium caused by scattering off nucleons. Thus the observed suppression pattern is caused by confined nuclear matter. Therefore it should be observable in collisions of smaller systems like proton-nucleus or deuterium-nucleus collisions. Indeed a detailed analysis of experimental data estimates the absorption cross section as $\sigma_{abs} = 7.3 \pm 0.6$ mb [Kha96]. Currently one believes, that the matter created in S-U collisions at 200 GeV per nucleon is still confined - the energy density is not sufficient to melt the nucleons.

Since the complete dimuon continuum in the J/ψ mass range cannot be predicted from theory, the NA50 experiment compared the charmonium production to the Drell-Yan ($q\bar{q} \rightarrow l^+l^-$) process, where the cross section can be predicted using the measured parton distribution functions. The disadvantage of choosing this reference is that the cross section for the Drell-Yan process is lower than the one for J/ψ production and thus the statistical error of the presented data is dominated by the Drell-Yan process. Figure 2.7 shows the measurement of the NA50 experiment [Ale04].

The ratio of produced dimuons from J/ψ 's to dimuons from the Drell-Yan process is plotted as a function of the length L of traversed nuclear matter. L is obtained from a Glauber model calculation [Kha96] [Abr02] and directly related to the centrality of the collision. The solid line represents the suppression as obtained from proton-proton and proton-nucleus collisions. Thus the line shows the amount of suppression due to nuclear absorption, that cannot be related to dissociation due to deconfinement. A clear deviation from this line can be observed for $L > 7.5$ fm. At this centrality the energy density is sufficiently high to create deconfined matter, leading possibly to dissociation of charmonium beyond the dissociation by nucleon scattering.

To determine the energy density necessary to melt charmonium, measurements on smaller systems have been performed. Although the maximum achievable energy density is smaller than in collisions of larger nuclei, smaller systems enable a higher resolution centrality scan. The results are shown in figure 2.8, left, [Sco07]. The J/ψ /Drell-Yan production is plotted as a function of the number of participants in the collision. The data is normalized to cold matter effects. A suppression exceeding the nuclear suppression is seen starting from 80 participants on. In figure (2.8, right) the data is compared to the results of the NA50 experiments from lead-lead collisions of the same energy of 158 GeV/nucleon. For peripheral collisions the ratio of measured/expected J/ψ yield is as expected, close to one, any observed dissociation is attributed to cold nuclear effects. For more central collisions a clear deviation from the expected behavior is observed, with good agreement between the In-In and the Pb-Pb data.

So far only results for J/ψ were presented. Measurements of ψ' are shown in figure 2.9. All the measurements suffer from the significantly lower statistics accumulated for the ψ' . The lower yield of the ψ' compared to the J/ψ is not only due to the lower production cross section, but dominantly due to the lower branching into dileptons ($\sigma_{\psi' \rightarrow l^+l^-} = 0.73$ % compared to $\sigma_{J/\psi \rightarrow l^+l^-} = 5.9$ %).

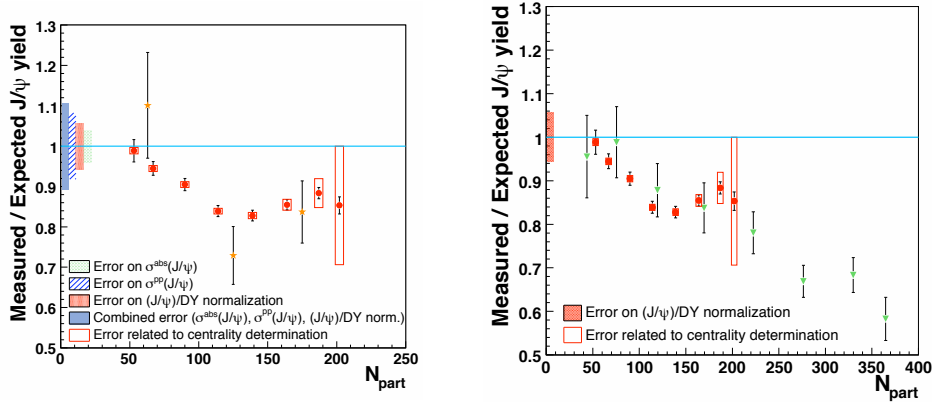


Figure 2.8: The left panel shows the centrality dependence of the J/ψ suppression for In-In collisions at 158 GeV/nucleon measured by NA60. The circles correspond to the measured J/ψ yield divided by cold nuclear matter effects calculations. The stars correspond to the ratio between measured and expected $\sigma_{J/\psi}/\sigma_{DrellYan}$. The right figure shows a comparison between the NA60 In-In and the NA50 Pb-Pb data [Sco07].

From figure 2.9 one can conclude that a similar suppression is seen for the ψ' compared to the J/ψ only the onset of the anomalous suppression is already at $L = 4$ fm and thus happens at a lower energy density. It seems as if the melting of higher excited charmonium states sets in already close to T_C – the ground state may survive up to higher values of T_C and thus up to higher energy densities (compare section 2.3).

2.4.2 RHIC measurements

The quarkonia measurements at RHIC are performed by the PHENIX collaboration [Ada06b]. The experimental setup is shown in figure 2.10. The experiment consists of a central part with the central magnet, a Cherenkov detector, drift chambers and electromagnetic calorimeters. The central part with a rapidity coverage of $|\eta| < 0.35$ is dedicated to the measurement of quarkonia decaying into dielectrons and the two arms with a rapidity coverage of $1.2 < |\eta| < 2.2$ measure quarkonia decays into dimuons. The azimuthal coverage of the central part is $2 \times 90^\circ$, the muon arms have full azimuthal coverage.

To cleanly track and identify the muons each of the two arms consist of a magnet, tracking chambers, a steel absorber and straw tubes for muon identification. PHENIX is able to detect quarkonia in central and forward rapidities in two different decay channels which allows for cross-checks between different results.

PHENIX has accumulated data on different collision energies ($\sqrt{s_{NN}} = 62$ GeV and 200 GeV) as well as different collision systems (p-p, d-Au, Cu-Cu and Au-Au) [Ada06b, Adl03b]. To show the effect of the nuclear medium the J/ψ production

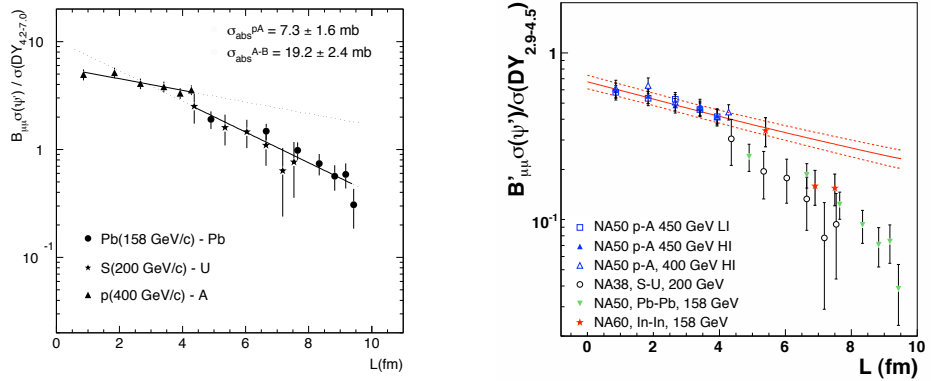


Figure 2.9: The ratio between ψ' production $\sigma(\psi')$ times the branching into muons $B_{\mu\mu}$ and the Drell-Yan reference process $\sigma(DY)$ as measured by the NA50 and NA60 collaborations at various energies and in different collisional systems. The lines indicate the calculated absorption due to cold nuclear matter effects. With increasing amount of traversed nuclear matter the amount of measured ψ' shows an anomalous suppression with respect to measured Drell-Yan reactions. [Ale06a, Sco07]

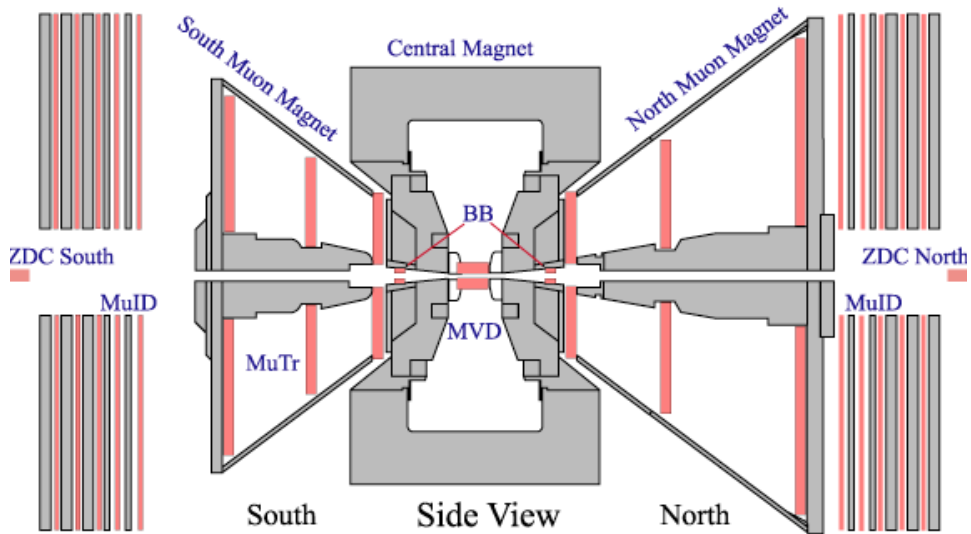


Figure 2.10: Setup of the PHENIX experiment. The experiment is designed to measure quarkonia via the dilepton decay mode. The central part ($|\eta| < 0.35$) measures $J/\psi \rightarrow e^+e^-$ and the two arms ($1.2 < |\eta| < 2.2$) measure $J/\psi \rightarrow \mu^+\mu^-$.

measured in proton-proton reactions is used as the reference process.

Figure 2.11 shows the observed suppression pattern observed by PHENIX in Au-Au and Cu-Cu collisions. $R_{AA}^{J/\psi}$ as defined in equation 2.8 is shown as a func-

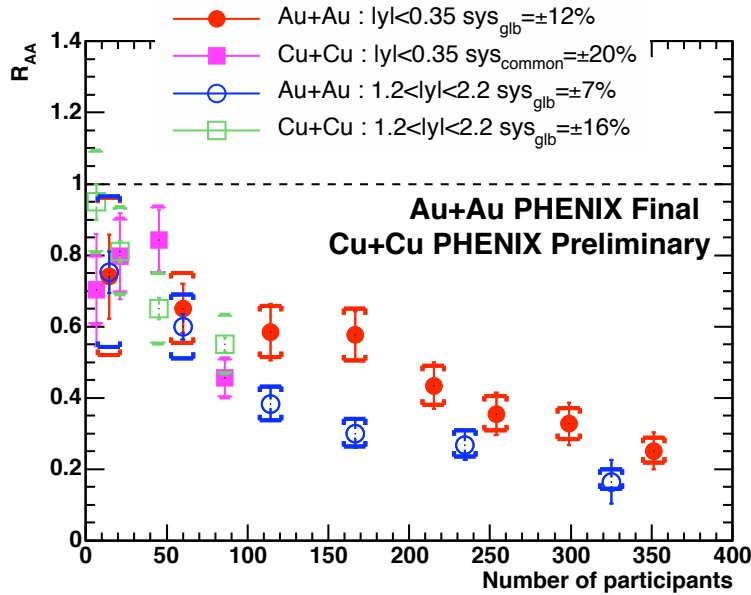


Figure 2.11: R_{AA} as a functions of the number of participants as measured by PHENIX in Au-Au (circles) and Cu-Cu collisions (squares) [Gun07].

tion of the number of participants. The J/ψ production is suppressed for large numbers of participants. Since cold nuclear matter effects are not subtracted here the observed suppression cannot be attributed to the dissociation of quarkonia in the deconfined medium alone. In figure 2.12 the ratio of R_{AA} versus cold nuclear matter effects (CNM) [Adl05a] is shown. For comparison also the J/ψ production data by NA50 and NA60 is included. For lower energy densities the data from SPS and RHIC agree quite well, while for higher energy densities the suppression observed at RHIC clearly exceeds the maximal suppression observed at SPS of $R_{AA}/CNM = 60\%$, this can be attributed to the higher energy density produced in RHIC collisions (compare appendix A: $\epsilon_0(\text{SPS}) \approx 3 \text{ GeV}/\text{fm}^3$, $\epsilon_0(\text{RHIC}) \approx 5 \text{ GeV}/\text{fm}^3$).

PHENIX is able to measure J/ψ production at forward and mid rapidity. Figure 2.13 shows the J/ψ R_{AA} in four different centrality bins as a function of the rapidity (y). While R_{AA} is almost constant for peripheral collisions (centrality bins 40-60% and 60-92%), the central collisions show a clear difference between forward and mid rapidity. The suppression of J/ψ production is significantly lower in forward/backward direction compared to the observed suppression at mid rapidity. This phenomenon could so far not be explained by current quarkonia production and suppression models.

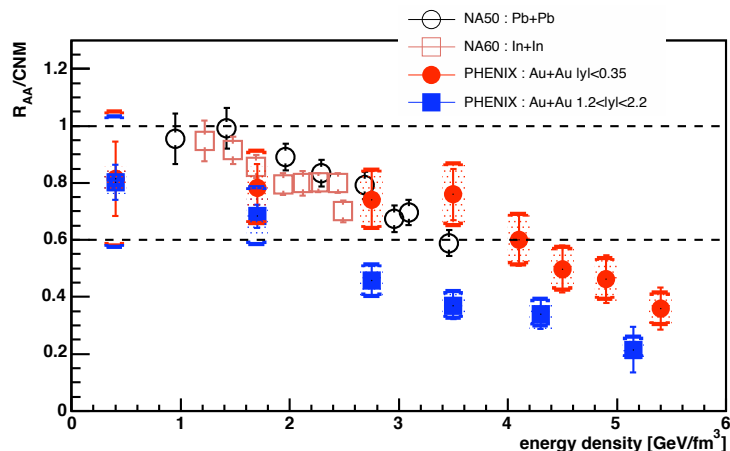


Figure 2.12: R_{AA}/CNM as a function of the Bjorken estimate (see Appendix A) of the energy density. The RHIC data ($\sqrt{S_{NN}} = 200$ GeV) is compared to SPS ($\sqrt{S_{NN}} = 17.3$ GeV) measurements performed by NA50 and NA60 [Gun07]. PHENIX estimates the cold nuclear matter effects from measurements on d+Au, while the NA50 and NA60 rely on theoretical calculations.

2.4.3 Theoretical interpretation

The presented data measured at SPS and RHIC can be interpreted within different models. In general one can divide the models in two classes: pure dissociation models and models including recombination.

The pure dissociation models [Kar05] are still very close to the original idea of quarkonia suppression already described in section 2.3. The presented model of quarkonium dissociation is computed using lattice QCD calculations at zero temperature. This leads to a charmonium dissociation temperature close to the proposed critical temperature of 170 MeV [Sus79, Kut80, Eng80, Brow90, Kar95]. More refined calculations using finite temperatures show that the ground state J/ψ may survive up to temperatures of about $2 T_C$ [Sat06b]. The spectral functions of different quarkonia states are shown in figure 2.14. The excited states, χ_C and ψ' , melt completely already very close to the critical temperature. Since a large fraction of about 40% of the measured J/ψ originate from the decay of these higher excited charmonium states, the total yield of J/ψ will decrease as well. This effect called *sequential dissociation* [Kar05] is used to explain the suppression pattern observed at the SPS shown in figure 2.8. At the highest energy densities, reflected by the largest number of participants, a suppression of the J/ψ down to 60% compared to the expected yield is observed. Thus one could interpret this pattern as a complete suppression of the higher excited charmonia states and their subsequent decay products, but since the temperature is not sufficiently high the ground state is not affected.

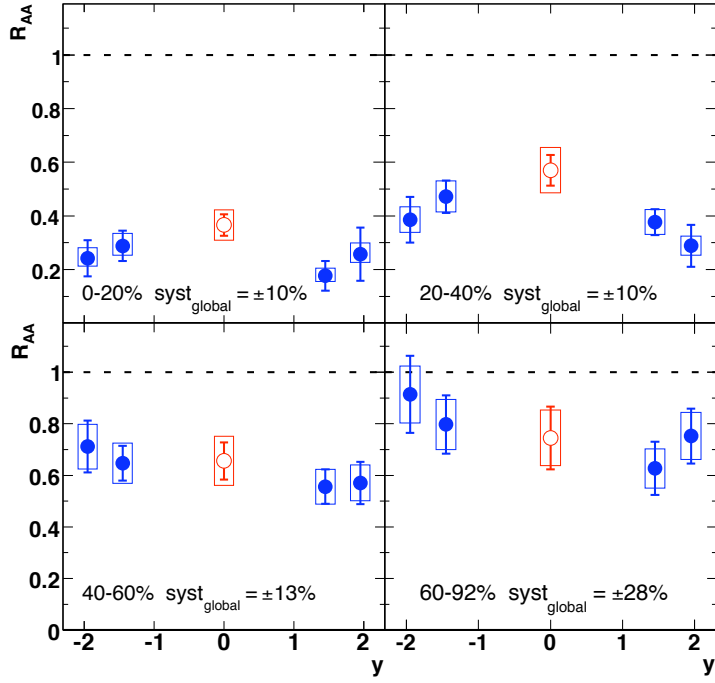


Figure 2.13: J/ψ R_{AA} as a function of the rapidity (y) for different centrality bins [Ada06b].

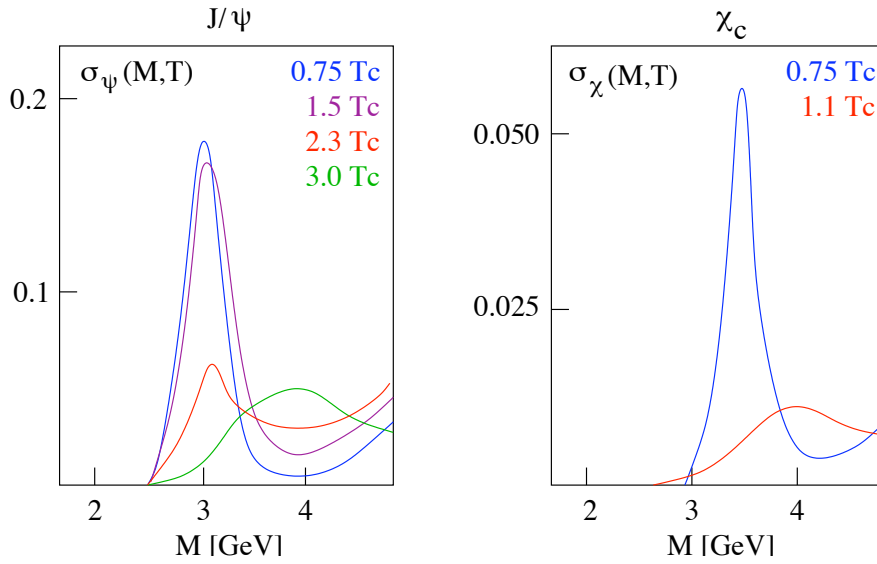


Figure 2.14: J/ψ and χ_C spectral functions at different temperatures [Sat05]

According to this model one expects that at RHIC, due to the higher energy density, also the ground state melts and charmonia is almost completely suppressed. Only a contribution of 15-20% of the total production cross section is expected, originating from peripheral zones of the collision. Figure 2.15 shows a comparison between the measured J/ψ production in Au-Au collisions at midrapidity and the pure dissociation model. Pure dissociation models [Rap05, Yan06] overpredict the suppression. Even before the suppression was measured different authors argued, that the relatively large number of charm quarks produced at RHIC (≈ 10) shall lead to a charmonium production at the hadronization stage. Although the term is misleading these models became known as *recombination models*. Not only those charm quarks which previously formed charmonium undergo this hadronization, but all produced charm quarks.

Several models include the charm hadronization in their calculations. The specific details of these models are not described here. A comparison of the recombination models [Rap05, Yan06, The05, And06, Cas00] is shown in figure 2.16. All reproduce the measured pattern. One should note that the recombination models include the assumption that charmonium is dissolved⁴ within the deconfined medium, thus they do not contradict the original idea of charmonium suppression [Mat86].

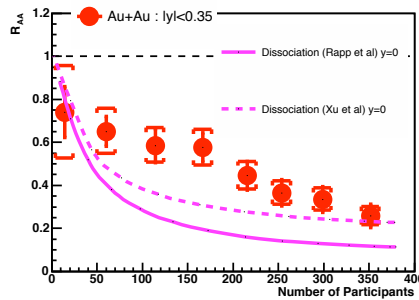


Figure 2.15: Comparison of the data on J/ψ production measured by PHENIX with predictions by pure dissociation models [Gun07].

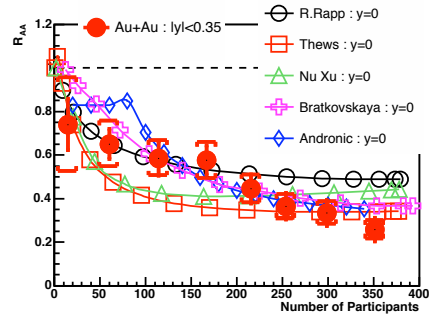


Figure 2.16: Comparison of the data on J/ψ production measured by PHENIX with different models assuming full dissociation and recombination [Gun07].

Although the analysis of the cold nuclear matter effects is still ongoing, the RHIC measurements imply that the original idea of dissociation has to be extended by the mechanism of charm hadronization. The J/ψ production out of uncorrelated charm quarks (≈ 10 at RHIC) at the freeze out of the deconfined medium, has to be taken into account to reproduce the observed yields. Since the amount of charm quarks produced at the SPS is rather low (≈ 0.1) no significant contribution to the production cross section of charmonium is seen. However at the LHC about 100 $c\bar{c}$ -pairs per central collision will be produced and about 1 J/ψ . At the LHC a higher

⁴The level of dissociation varies within the models.

energy density is expected compared to RHIC. Thus all initially produced J/ψ s are expected to be suppressed. But due to the large number of charm quarks the production within the hadronization phase is expected to produce an even higher J/ψ yield compared to the production from initial collisions. [And03].

At the LHC for the first time in heavy-ion collisions the Υ family will be produced in measurable quantities, opening the possibility to use a second quarkonium probe to explore the deconfined phase. One advantage of the Υ family compared to the J/ψ family is that the first excited state is compared to the ground state more often produced ($\sigma_{\Upsilon \rightarrow e^+e^-} / \sigma_{\Upsilon' \rightarrow e^+e^-} \approx 3.5$ compared to $\sigma_{J/\psi \rightarrow e^+e^-} / \sigma_{\psi' \rightarrow e^+e^-} \approx 52$). Lattice calculations [Sat06b] indicate that the ground state of the Υ may survive up to temperatures of $4 T_C$ while the excited states vanish already close to T_C . Thus one would expect the suppression pattern observed for the Υ at LHC to be similar to the pattern for the J/ψ seen at RHIC. The difference is that also the suppression of the higher mass state can be shown and related to the changing production of the ground state.

$b\bar{b}$ pairs are expected to be produced at a rate of roughly 4 pairs per central collision. This is comparable to the amount of $c\bar{c}$ pairs produced at RHIC. Thus hadronization of $b\bar{b}$ to bottomonium will not contribute significantly to the total production, while the dissociation by the deconfined medium should be present for the excited states and for the most central collisions maybe even for the Υ .

The J/ψ should be strongly enhanced, predicted by the recombination models. At the LHC it will be possible to test the dissociation/recombination model using the two quarkonia probes within the same experimental environment.

Chapter 3

Heavy Ion Collisions at the Large Hadron Collider

3.1 The Large Hadron Collider: LHC

The Large Hadron Collider (LHC) is constructed at CERN and will start its operation in 2008. It resides in the old tunnel of the Large Electron Positron (LEP) collider which stopped operation in 2000. Its diameter is 9 km, resulting in 27 km circumference. It consists of acceleration cavities and bending magnets. The bending magnets are operated at a field of 8.3 T and are super conductive. The cooling is done using liquid helium at 2 K. The LHC will accelerate protons and heavy-ions with so far unprecedented energies¹. Due to this large collision energies new insights into the structure of matter is expected. The planned running scenarios [Car04] and main beam parameters are summarized in table 3.1.

One should note that especially the luminosity in proton-proton collisions is not limited by the collider itself but from the ALICE detector. Since proton-proton beams have a bunch crossing time of 25 ns this will lead to a pile-up of roughly

¹Increase in energy of a factor of 30 compared to the RHIC and 300 for the SPS

Table 3.1: Planned running scenarios taken from [Ale06b]. Further measurements depend on experimental findings and might include running at lower energies and/or with other collision systems.

System	$\sqrt{s_{NN}}$	Luminosity $\text{cm}^{-2}\text{s}^{-1}$	total running time
p-p	14 TeV	$5 \cdot 10^{30}$	10 years
Pb-Pb	5.5 TeV	$1 \cdot 10^{27}$	1-2 years
p(d)(α)-Pb	8.8 TeV	$1.1 \cdot 10^{29}$	1 year
Ar-Ar	6.3 TeV	$2.8 \cdot 10^{27}$	1-2 years

30 events in the TPC. This means that 97 % of the recorded data belong to partial events and cannot be used for analysis. To restrict the amount of unusable data the luminosity will be reduced such that these values are not exceeded. After the first periods of running it is planned to use the High-Level-Trigger (HLT) to remove the pile-up of events. The HLT will reconstruct events online and is thus able to remove tracks which do not belong to the primary vertex but to vertices from subsequent collisions.

In lead-lead collisions the luminosity is not limited by the detector but the limiting factors arise from accelerator specific problems. At the LHC any uncontrolled loss of the beam will, due to the high beam energy and intensity, result in serious damages of the accelerator. To control the position of the beam, beam position monitors are periodically installed. These beam position monitors require a certain minimal amount of charge within one bunch. Since with three data taking experiments and thus also three interaction points the charge within a bunch is reduced with every collision, it has to be guaranteed that the bunch charge is always above limits. The luminosity is reduced such that the beam remains stable over a full data taking period of 8 h.

3.2 A Large Ion Collider Experiment: ALICE

Four large experiments are planned at the LHC. Two of them, ATLAS² and CMS³, dedicated to the search of new elementary particles with very low production yields in proton-proton collisions. These two largest experiments have a similar physics program and acceptance. The third experiment is the LHC-B [Lhb07] experiment searching for CP-violations in the B-system. Dedicated to the measurement of a large variety of observables in heavy-ion collisions ALICE was planned.

ALICE was designed to track and identify particles from ion collisions from rather low transverse momenta of 100 MeV/c on. The experiment is shown in figure 3.1. The central part is called the *Central Barrel* and the forward part called the *Muon Arm*.

The major constraint for the design of the detectors is the expected multiplicity of charged particles. The detectors should be able to track and identify almost all particles even at the highest expected multiplicities. For this reason the granularity of a detector has to be such that at the highest track densities two tracks can be clearly separated. Since the energies at LHC will exceed the highest achieved energy in a heavy ion collision by a factor of thirty, the charged particle multiplicity cannot be easily predicted by extrapolations without introducing a huge uncertainty. Figure 3.2 shows different extrapolations for the charged particle multiplicity per participating nucleon pair. Unfortunately previous measurements cannot constrain the scaling behaviour to either a power-law scaling, leading to rather large multiplicity of 13 per participant, or a logarithmic scaling, leading to more modest

²A Toroidal LHC AparatuS [Atl07]

³Compact Muon Solenoid [Cms07]

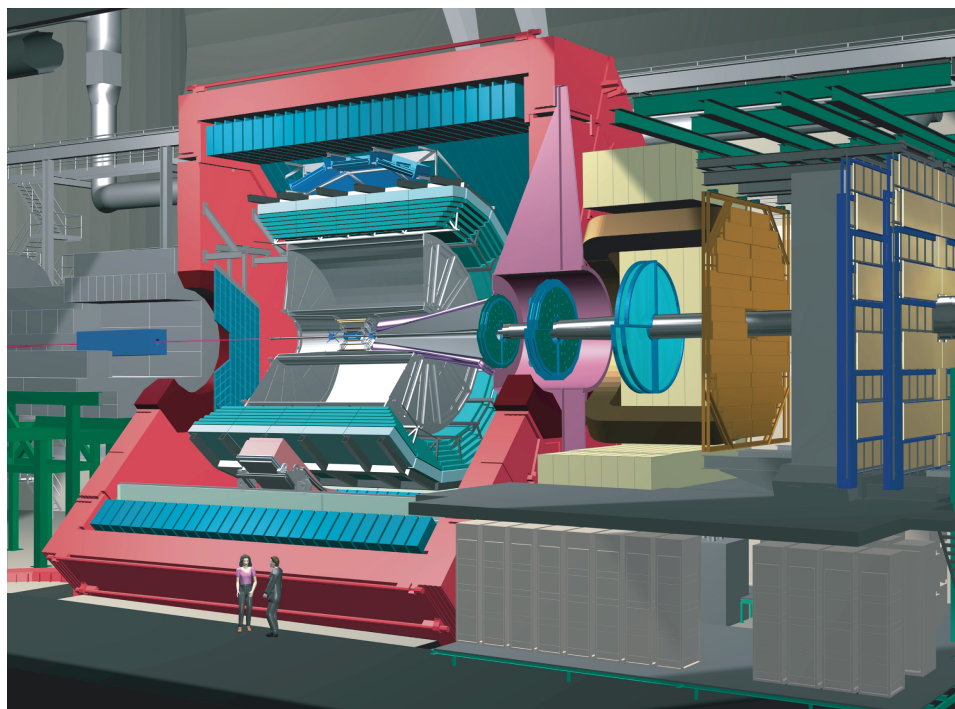


Figure 3.1: Schematic Drawing of ALICE. The experiment is split into two parts: the so-called Central Barrel contained in the L3 magnet (red) and the Muon Arm.

predictions of 5 particles per participant. Taking into account that for a lead-lead collision one expects on average 170 participating nucleons [Car04], in absolute numbers one would expect the multiplicity at ALICE to be between $5 \times 170 = 850$ and $13 \times 170 = 2210$ charged particles per unit rapidity. Since the spread in the predictions is rather large and the given numbers represent only an average multiplicity the detectors were designed to cope with a multiplicity of up to $dN/dy_{ch} = 6000$ with $dN/dy_{ch} = 8000$ as an upper limit. Only for multiplicities exceeding 8000 particles the reconstruction efficiency drops significantly due to overlapping tracks, that cannot be disentangled.

The Muon Arm covering a pseudo-rapidity range from $-2.4 > \eta > -4.0$ is as the name indicates dedicated to the measurement of muons. The detector layout is similar to the layout of the muon arms of the PHENIX experiment (see figure 2.10). Hadrons and electrons are removed by the absorber. The muon tracks are bent for momentum measurement by the dipole with a integrated field of 3 Tm and then detected by the huge arrays of trigger and tracking chambers.

The central part of ALICE is an assembly of various detectors. One can subdivide the detectors into detectors of general interest used for a large variation of physics analyses, detectors providing basic informations like multiplicity and detectors dedicated to specific observables. The detectors providing information of general interest like momentum, vertex coordinates and particle identification are

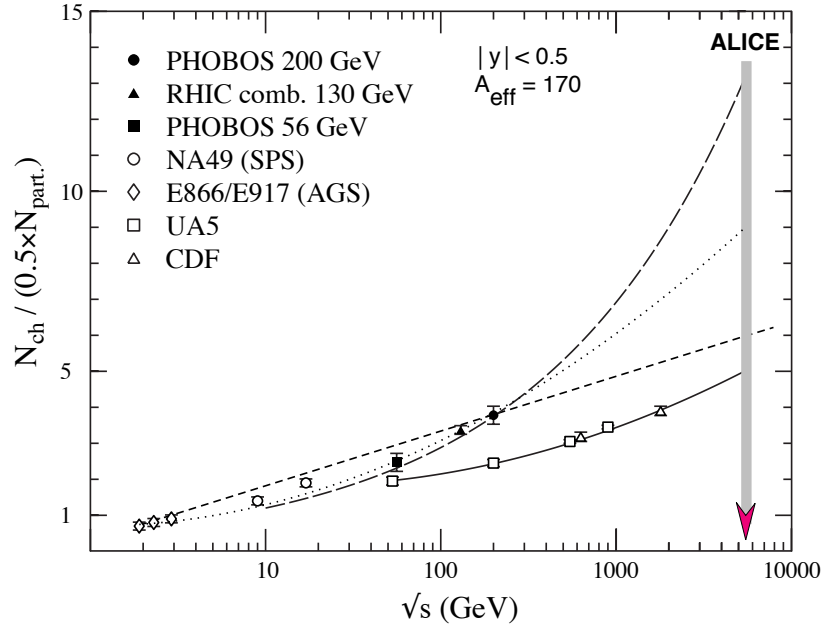


Figure 3.2: Centre-of-mass energy (\sqrt{s}) dependency of the charged particle multiplicity per unit rapidity for A-A and p-p collisions [Car04]. Three different types of functions were fitted to the data resulting in a huge spread of predictions for the LHC. The dashed line is a logarithmic fit to the nuclear data. The dotted line is a \ln^2 fit and matches the RHIC data best. The long dashed line leading to the highest prediction is a fit including a saturation scale [Ame01, Arm00, Fer98, Arm94, Ame94] leading to a power-law scaling.

the Inner Tracking System (ITS), the Time Projection Chamber (TPC), the Transition Radiation Detector (TRD) and the Time of Flight detector (TOF). They all cover a pseudo-rapidity range from $-0.9 < \eta < 0.9$ and full azimuth and are thus often called the ALICE Central Barrel (ACB). The ACB is used for the presented studies and will therefore be described in more detail in the following section. The detectors dedicated to a specific physics task are the Photon Spectrometer (PHOS) measuring high momentum photons, the High Momentum Particle Identification (HMPID) to separate various kinds of hadrons and the Electromagnetic Calorimeter (EMCAL) for the detection of high momentum electromagnetic probes. These three detectors cover only a small part of the full acceptance. A detailed description of the individual subcomponents of ALICE can be found in [Ali99].

With the already quoted (table 3.1) luminosity of $10^{27} \text{ cm}^{-2} \text{ s}^{-1}$ and an expected minimum bias cross section of $\sigma_{MB} = 8 \text{ b}$ [Car04] one expects 8000 minimum bias interactions per second. Since the most interesting physical processes are expected in the 10 % most central events, ALICE should be able to take data

at a rate of slightly less than 1 kHz. This rather low rate allows the usage of slow but very precise tracking detectors like the Time Projection Chamber and the Silicon Drift Detector. The advantage of using a TPC as the main tracking device is, that the number of measured points on a track is large. therefore the combinatorial background of the tracking algorithm arising from combinations of points or clusters belonging to different tracks is very low. This enables the measurement of a large number of tracks within one event. In heavy-ion collisions not only a few high momentum particles are of interest. The bulk properties of the produced medium, reflecting its characteristics, manifest in the relative abundancies and the momentum distributions of all produced particles. therefore it is necessary to track and identify also particles with rather low momenta.

3.3 The central barrel

As already mentioned the central barrel is a synonym for the four inner detectors namely ITS, TPC, TRD and TOF contained in the 0.5 T L3-magnet. The magnet was inherited from the old LEP experiment L3. While ITS, TPC and TRD are due to their specific properties essential for the detection of quarkonia and will be discussed in detail in the following sections, the Time of Flight detector was designed to identify heavier particles like pions, kaons and protons by their time of flight with respect to the measured momentum. For a detailed description of the TOF system see [Ali00].

3.3.1 Inner Tracking System – ITS

The main purpose of the Inner Tracking System is the determination of vertices with very high resolution. Besides that it will be used for tracking and identification of particles with very low momenta and it will improve the momentum resolution of tracks with higher momentum. While doing this the ITS has to be able to cope with the large number of charged particles expected to be produced in a lead-lead collision. Thus it has to have a high granularity and radiation hardness. Further on, not to change the yield and the momentum of the particles, it has to be as thin as possible.

The ITS is shown in figure 3.3 it consists of six cylindrical layers of detectors. To reduce losses due to gaps in the detector, the segments overlap at the borders. Three different types of silicon detectors are used. The innermost layers are made of pixel detectors providing the highest precision, namely $12\ \mu\text{m}$ in $r\phi$ and $70\ \mu\text{m}$ in z -direction⁴. However this high spatial resolution includes a large number of readout channels adding up to a total of 16 million channels for both layers. The third and fourth layer are made of a silicon drift detector working similar as a time projection chamber with the electrons drifting within the silicon. This design was

⁴ z is the direction of the beam with positive z pointing away from the muon-arm. ϕ denotes the azimuthal angle (positive direction counterclockwise) and r the radius of the cylinder.

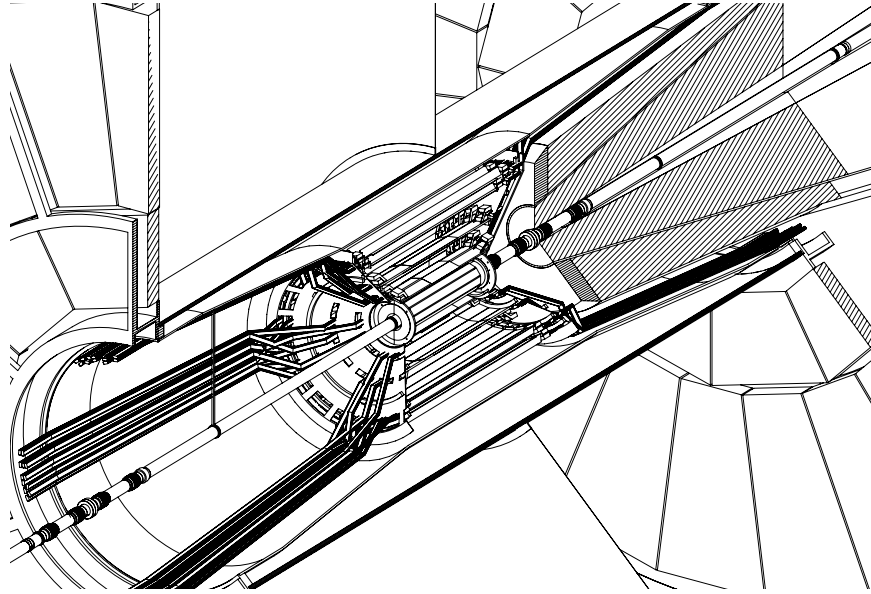


Figure 3.3: Schematic Drawing of the Inner tracking system located around the vertex region. One can also see the inner wall of the TPC, the beam pipe and parts of the absorber.

chosen to improve the resolution especially in the z -direction which is $28 \mu\text{m}$ and $38 \mu\text{m}$ in $r\phi$ -direction. The two outermost layers are made of silicon strip detectors with a spatial resolution of $20 \mu\text{m}$ ($r\phi$) and $830 \mu\text{m}$ (z).

All detectors were constructed as thin as possible and the total thickness does not exceed 6% of one radiation length. The complicated support structures were constructed out of carbon fiber combining excellent stability at minimal weight and radiation length.

The important parameter for the ITS is the so-called impact parameter resolution. Impact parameter in this case denotes the distance of a reconstructed track to a primary or secondary vertex. Since the ITS was designed to measure the decay of heavy charm and beauty hadrons with life times ranging from $c\tau = 100\text{-}500 \mu\text{m}$ these numbers determine the desired performance. Figure 3.4 shows the combined impact parameter resolution of primary pions reconstructed in the ITS and the TPC. The resolution in the $r\phi$ plane falls below $100 \mu\text{m}$ for momenta above $700 \text{ MeV}/c$ and between 2 and 3 GeV/c in the z -plane. Thus the reconstruction of charm and beauty decays should be possible in ALICE (see also chapter 5 and [Ale06c]).

3.3.2 Time Projection Chamber – TPC

The ALICE Time Projection Chamber [Del00, Gla07] is with a length of 5 m, an inner radius of 0.845 m, an outer radius of 2.466 m resulting in an active volume of 95 m^3 the largest TPC ever built. A sketch of the detector is shown in figure 3.5.

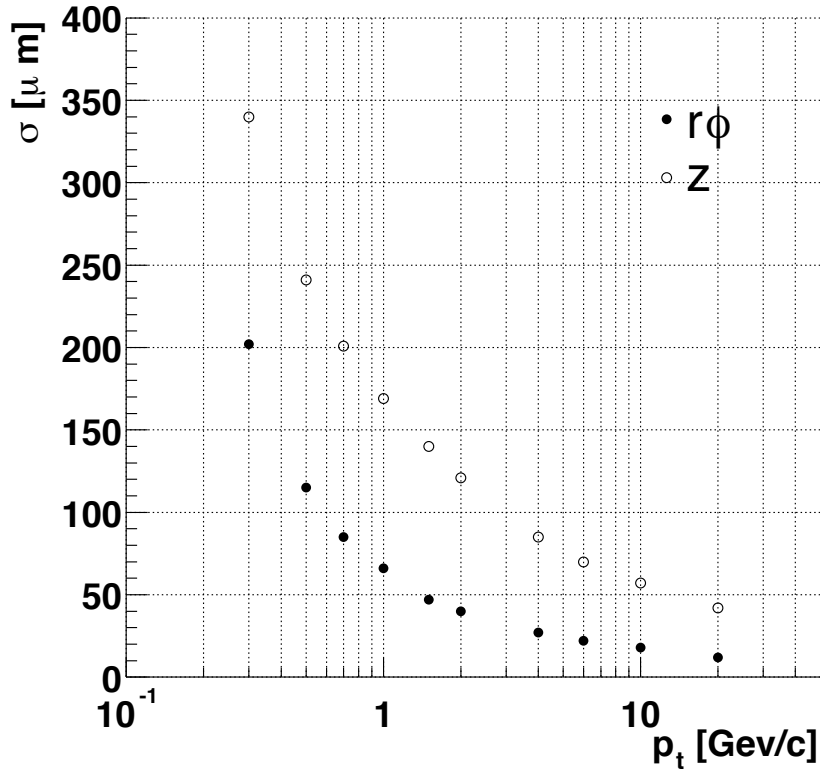


Figure 3.4: The impact parameter resolution for primary charged pions reconstructed in the TPC and ITS (with 6 of 6 possible clusters in the ITS) for central lead-lead collisions with a multiplicity of $dN/dy_{ch} = 6000$ per unit rapidity.

The detector volume is filled with a mixture of 90% Neon, 10% CO₂ and a small fraction of N₂. The advantage of this gas mixture is that it shows almost no ageing effects in contrast to other mixtures like CF₄. Further advantages are a short drift time, small diffusion and a low radiation length. These nice features have to be paid with a strong dependence of the drift velocity on the temperature. For this reason the temperature has to be kept constant within an interval of 0.1 K. To prevent heat conduction from the outer detectors a thermal shield was added in between TPC and TRD.

The central electrode operates at a voltage of 100 kV translating into a field gradient of 400 V/cm and a maximum drift time of 92 μs . The signals are read out at the two end caps by 72 multi-wire proportional chambers. Each of these chambers has three layers of wires. To prevent space charge effects within the detector volume the outermost wire layer of the read-out chambers is used as a gating grid such that electrons are only collected in the chambers if a Level-One trigger accept was send (see section 3.3.4)

ALICE will be the only experiment at the LHC using a large TPC as the cen-

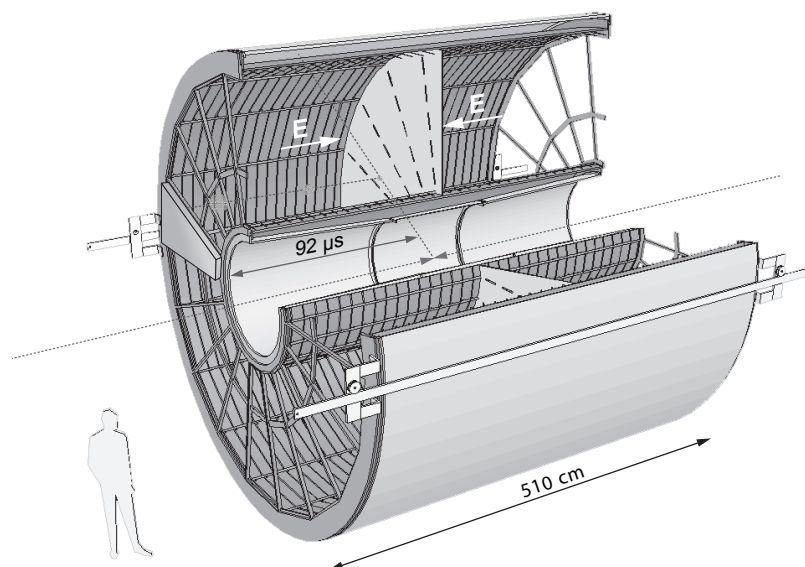


Figure 3.5: Schematic drawing of the ALICE TPC. One can nicely see the central electrode operated at a voltage of 100 kV. On the front and end cap the segmentation of the TPC into 18 azimuthal sectors and 2 radial sectors is visible resulting in a total of 72 read-out chambers.

tral tracking detector. This can be understood when looking at the desired physics observables. As the dedicated heavy-ion experiment ALICE will not only measure high- p_t particles but the physics program requires to measure also low momentum particles. During a heavy-ion collision at an energy of 5.5 TeV per nucleon up to 6 000 particles might be produced per unit of rapidity. Thus one expects about 20 000 charged tracks within the central part of the detector. For high energy physics topics like top-quark measurements and the search for the Higgs-boson most of these particles contribute to the background, while the measurement of relative particle abundancies and their momentum distributions are crucial for the understanding of a heavy-ion reaction. To track all these particles a TPC is the best choice since it provides an almost continuous picture of a particle track (see figure 3.6). Other tracking detectors do have a certain amount of tracking planes and thus cannot provide a continuous track but only the coordinates where a particle track crosses one of the tracking planes. Now every of these points has to be associated to one track. With increasing track density this association gets ambiguous. Thus at some point tracks will be reconstructed which do not belong to a physical particle. Most of these tracks can be suppressed by the tracking algorithm using checks on consistency or maximum allowed deviation from a specific parameter. Nevertheless a few of these *ghost* tracks remain, the more particles are within the detector. With a TPC a track can almost continuously be followed and thus the association of a measured cluster with the physical track is almost unambiguous and

the *ghost*-rate is negligible.

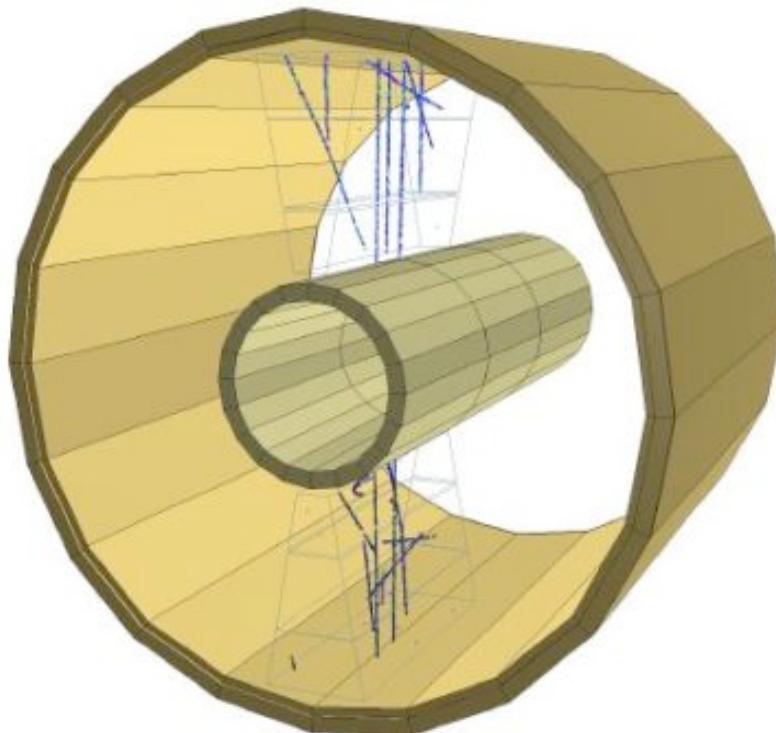


Figure 3.6: Schematic view of the first cosmic shower recorded in the ALICE TPC. One can easily recognize the tracks with the naked eye. This demonstrates the excellent tracking capabilities of a TPC.

The TPC will not only serve as the main tracking device but will also contribute strongly to the particle identification. Particles can be identified within the TPC by their specific loss of energy due to interactions with the TPC gas. The performance of the particle identification will be discussed in section 4.4.

The pads of the read-out chambers are read-out by the especially designed front-end electronics [Mus03, Bos03]. The electronic signal depends on the pad shape and the signal distribution, having a long tail due to the slowly drifting ions. The electronic includes various options for signal shaping like tail cancellation and other digital filters [Bra05] to account for these effects. Although the number of pads is with 560 000 small compared to the number of pads in ITS or TRD, a good resolution in z -direction requires a sampling frequency of 500 – 1 000 Hz which results in a maximum of 5×10^8 bins and an event size of about 60 MB. Since the total bandwidth is limited, the trigger rate is limited to 200 Hz for central lead-lead events and 1 kHz for proton proton collisions. Thus the signal to background ratio for rare probes like measurements of high energy jets and quarkonia has to be increased by the usage of a trigger system with various trigger levels which for the highest trigger level (Level 3 see section 3.3.4 and [Bra03, Lin03]) already includes

coarse tracking and fast analysis algorithms.

The whole read-out chain using final components has been tested extensively in beam tests [Ant06] and it has been shown that the current design meets the physical requirements.

3.3.3 Transition Radiation Detector – TRD

As one of the last subdetectors of ALICE the TRD [Ali01] was added. It has two main purposes namely the identification of electrons over a large momentum range via their emission of transition radiation and to serve as a trigger device for events containing high $p_T > 3$ GeV/c electrons. Further on it will, since it provides additional points to charged particle tracks, increase the tracking resolution.

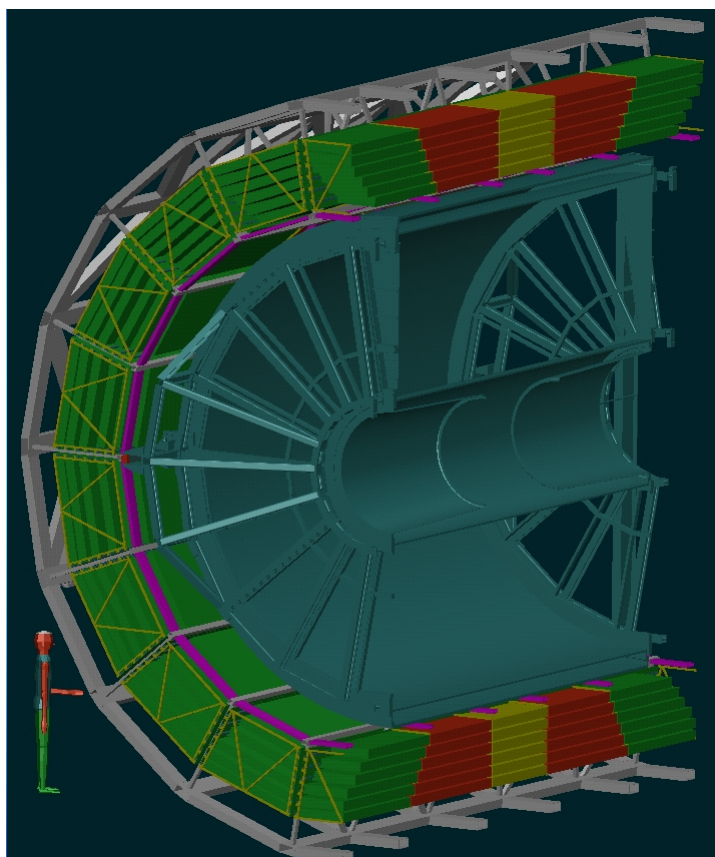


Figure 3.7: Schematic drawing of (one half) of the ALICE TRD. The complete detector consists of 540 read-out chambers (green, red and yellow) arranged 18 super modules covering the full azimuth. Each of these super modules consists of 6 radial layers and 5 stacks of chambers in z-direction. The total sensitive area of the detector is 750 m^2 divided into 1.16 million read-out channels.

The detector is shown in figure (3.7). It consists of 540 read-out chambers

arranged in 18 super modules covering the same angle as a corresponding TPC sector. Each of these super modules consists of 30 chambers arranged in 6 radial layers and 5 stacks in z -direction. The total active volume is about 27 m^3 , filled with a mixture of Xenon (85%) and CO_2 (15%). Since Xenon is very rare noble gas (0.08 ml Xenon in 1 m^3 air), the amount of Xenon used in the TRD represents roughly one annual production worldwide. This puts strong requirements in terms of gas tightness on the detector. The total sensitive area of the detector is roughly 750 m^2 divided into 1.16 million read-out pads. Each channel is individually read-out, 18 read-out channels are bundled and connected to a highly integrated multi chip module (MCM). The MCM contains two main parts: the pre-amplifier and shaper chip called PASA and the Tracklet processor (TRAP) [Ang06] containing a 10 bit analog to digital converter with a sampling rate of 10 MHz configurable digital filters providing further shaping, pedestal subtraction, tail cancellation and zero suppression. In addition short tracks within one chamber, called tracklets, are processed used for the trigger on high p_t particles.

Transition Radiation

The principle the TRD uses to discriminate between electrons and heavier particles is the emission of transition radiation. Transition radiation was predicted in 1945 [Gin45] and first observed in 1959 [Gol59]. It denotes the effect that a charged particle, moving with a certain velocity, undergoing transitions between materials of different dielectrical properties emits electromagnetic radiation. Since the electrical field surrounding every charged particle depends not only on the charge but also on the speed of the particle and of the dielectric properties of the surrounding medium, changing one of these parameters leads to a change in the field. For example changing the velocity of a charged particle leads to the emission of Bremsstrahlung. Changing the medium surrounding the particle also leads to a changing field and thus to the emission of transition radiation. A detailed theoretical treatment can be found in [Gin80, Gin79], here only for the TRD important relations between the traversing particle and the emitted radiation shall be reported. Important for the design of a transition radiation detector are the probability to produce a transition radiation photon and its energy.

The probability to produce a photon during one transition of a charged particle first depends on the relativistic γ -factor⁵. Thus the emission of transition radiation is directly related to the mass of a particle. This enables just by the observation of transition radiation the distinction between different particles without the need of a precise momentum measurement like it is needed for particle identification via the specific energy loss of particles in the medium. Table 3.2 shows values for γ for different particles with different momenta. The threshold for transition radiation emission depend on the thickness and on the plasma frequency difference of the radiator materials. For polypropylene/air radiators particles with a γ ex-

⁵ $\gamma = \frac{E}{m}$

ceeding 1000 produce transition radiation [Dol93]. Over a large momentum range (1-100 GeV/c) only electrons are expected to emit transition radiation. Thus transition radiation detectors are very well suited to separate especially electrons from heavier particles. The probability to emit a transition radiation photon during one transition is on the order of $\alpha = 1/137$. For this reason transition radiation detectors are designed such that the particle undergo not only one but many transitions. First detectors were built with foil stacks with a lot of parallel foils. This design has some clear disadvantages: It is mechanically very difficult to guarantee the parallelity of the foils. This could only be done using a complex gas system, controlling the pressure between the foil layers [Man88]. Newer detectors like also the ALICE TRD rely on irregular radiator material like foams or fibre mats. While the emission of transition radiation in regular foil stacks can be calculated analytically [Fab75], calculations for irregular radiators are still missing. Nowadays usually a combination of plastic foams and fibre mats are used since especially foams can be produced in any desired geometrical shape and they are self sustaining and need no additional mechanical support structure. The drawback is that for simulations of the detector response parametrizations have to be used. In the case of the ALICE TRD the behavior of the radiator is modeled by a foil stack. The adjustable parameters are the number of foils N_f , the thickness of one foil d_1 and the distance between the foils d_2 . Figure 3.8 shows distributions of transition radiation energy as measured in a test experiment in 2004 [Bal06]. The three parameters were adjusted such ($N_f = 120$, $d_1 = 15 \mu\text{m}$ and $d_2 = 400 \mu\text{m}$) that the simulation matches the measured spectra (see also [Lip04, And04]). Although these parameters do not reflect any characteristics of the used fiber and foam radiator, the simulation reproduces the correct transition radiation yield and can thus be used to estimate the performance of the electron - pion discrimination.

The energy of the photons depends on the different dielectrical properties of the two media. Since the photon is produced inside the radiator material, the material, in order not to absorb the photon, has to be transparent to the produced photon. For the transition between polypropylen and air and an electron with a γ -factor larger than thousand one finds that the energy of the produced photon is in the X-ray range and the photon is therefor able to leave the radiator. A detailed description of the emitted energy spectrum can be found in [Fav01]. In order to absorb the photon with a high probability a gas with a large absorption cross section for X-ray has to be used. For this reason Xenon was chosen.

Design of the read-out chambers

Now that the basic design requirements arising from the production and detection of transition radiation were described one should take a closer look at the design of a read-out chamber. Figure 3.9 shows a schematic drawing of one side of a read-out chamber. The basic design is the one of a Multi-Wire-Proportional-Chamber (MWPC) with pad readout. The charged particles traverse the 3 cm long drift region and create electron ion pairs along their track. The electrons due to

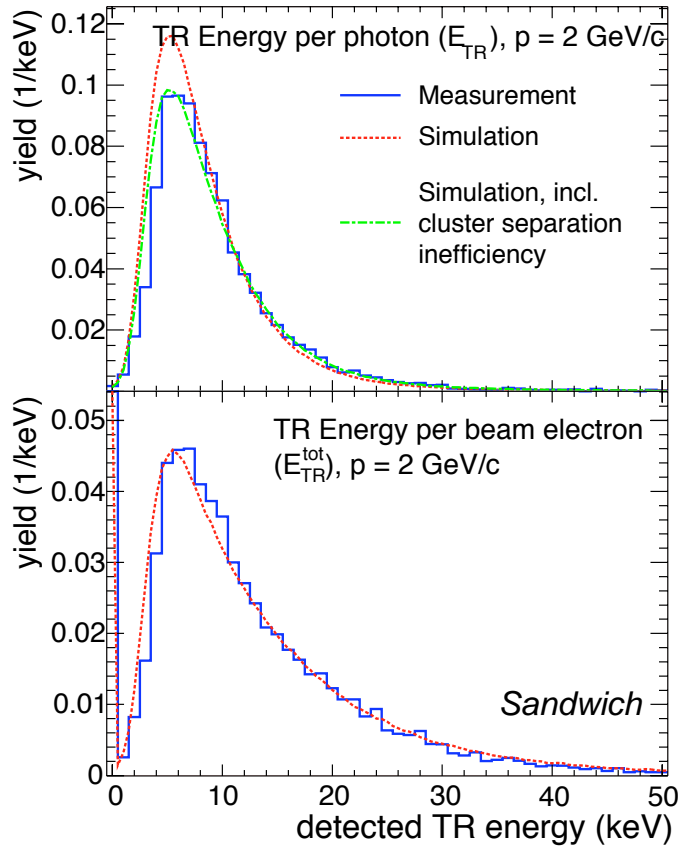


Figure 3.8: Measured and simulated spectra of transition radiation, recorded at a test experiment in 2004 [Bal06]. The upper panel shows the energy distribution of single transition radiation photons. The lower panel shows the distribution of the total transition radiation energy per beam electron. The parameters have been adjusted such, that the simulation matches the measurements. The obtained parameters can be used to obtain realistic simulations on the electron-pion discrimination performance.

their charge drift in the field (2.1 kV) of the drift anode (aluminized backside of the radiator) towards the cathode wire plane. The cathode wires are beryllium wires with a copper coating and a diameter of $75 \mu\text{m}$. The grounded cathode wire plane separates the drift from the amplification region. The amplification region is 0.7 cm long, ending at the pad plane. In between the pad plane and the cathode wire grid, is the anode wire grid. The anode wires are tungsten wires with a gold coating and a diameter of $20 \mu\text{m}$. The nominal anode voltage is 1.6 kV, providing an average gain factor of 10000. The signals are collected on the pad plane. All of the pads are connected to a read-out channel. The read-out electronics is mounted on the back panel of each chamber.

Table 3.2: The relativistic γ factor for different particles with various momenta. Only particles with $\gamma > 1000$ produce transition radiation in significant amount.

particle mass [MeV/c ²]	e	μ	π	K	p
	0.511	105.658	139.57	493.677	938.272
p [GeV/c]	γ				
0.1	195.	1.4	1.2	1.0	1.0
1.	1956.	9.5	7.2	2.26	1.5
10.	19569.	94.5	71.2	20.3	10.7
100.	195000.	946.	716.5	202.6	106.6
1000.	$2 \cdot 10^6$	9500.	7200	2000.	1065.

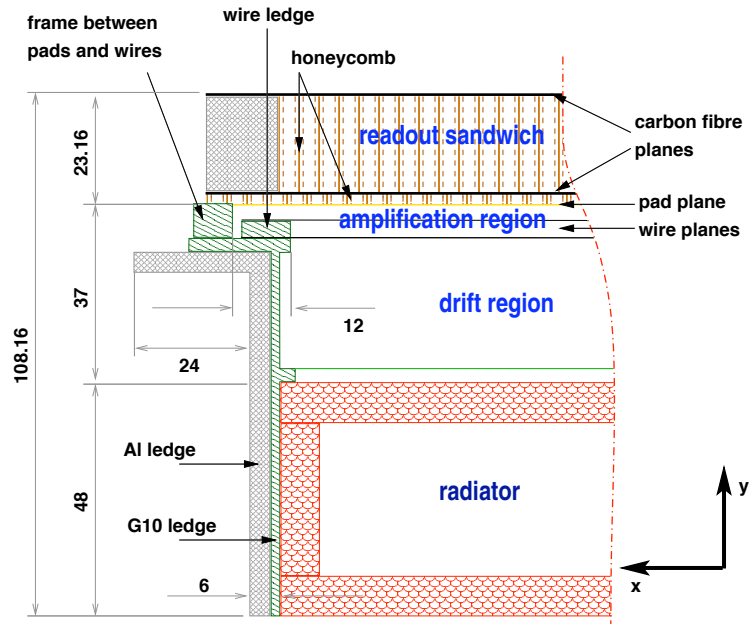


Figure 3.9: Schematic drawing of one side of an ALICE TRD read-out chamber. The size of the chambers varies from 1.5 m² up to 2 m². To minimize the losses due to Bremsstrahlung light materials or compound materials were chosen especially for the back panel which is made out of Nomex honeycomb structure with carbon fibre surfaces.

The most significant change compared to other MWPCs is the radiator made of polypropylene foam and fiber mats. The foam is needed for mechanical stability while the transition radiation yield is higher for the fiber mats. As any MWPC the TRD read-out chamber does detect charged particles by their specific energy

loss due to interactions with the filling gas. Thus the TRD serves as an additional tracking device for any charged particle. In addition to the energy loss electrons produce transition radiation within the radiator. The radiation is immediately absorbed by the Xenon at the entrance of the chamber. The process is shown in figure 3.10. The transition radiation contributes in two ways to the particle identification: First it contributes to the overall measured energy measured for one particle. Since electrons emit transition radiation in addition to their *normal* specific energy loss, the integrated deposited energy is significantly larger for electrons than for pions. The second information is provided by the time resolution of the read-out electronics. Since the transition radiation is absorbed at the entrance of the drift region, the signal induced by this incident drifts longer compared to the signals induced by the specific energy loss, since these signals continuously ionize atoms along their path. The process is depicted in figure 3.11. The large peak at low drift times corresponds to ionization happened directly within the amplification zone. After this peak an almost constant plateau is observed for pions which represents the continuous loss of energy within the drift volume. For electrons the signal increases again due to the production of the transition radiation. The resulting performance for particle identification will be discussed in chapter 4.4.

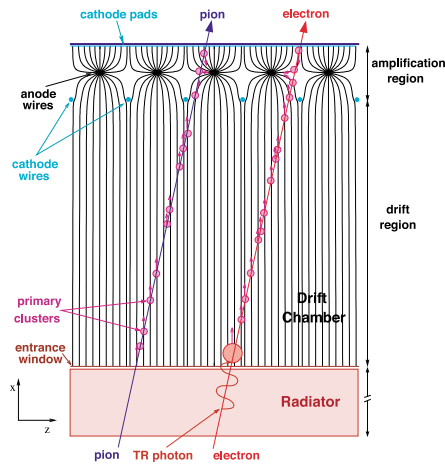


Figure 3.10: The signal production in the TRD read-out chambers for electrons and pions.

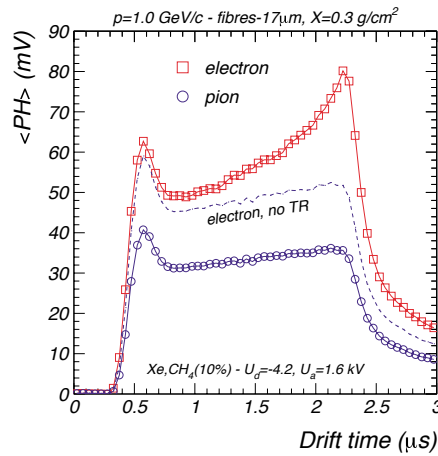


Figure 3.11: The time response for 1 GeV/c electrons and pions measured for a fibre radiator with 17 μm fibres.

3.3.4 Trigger and data acquisition

Trigger Levels

The ALICE trigger system [Ali05] was designed to meet a large variety of requirements, from constraints by the desired physics to technical feasibility. Two

detectors were especially designed to deliver fast trigger information of general interest namely V0 triggering on centrality and T0 delivering fast information on multiplicity. Besides that more specialized detector system can cause triggers on their specific process of interest, like the EMCAL will trigger on jets, PHOS on high p_t photons, the muon spectrometer triggers on muons and the TRD offers the possibility to trigger on electrons. The trigger system is staged into four levels. The lowest level trigger L0 is delivered within $1.2 \mu\text{s}$ and registers if there was a collision and evaluates simple information like multiplicity, centrality or if there was a signal in one of the especially dedicated detectors as previously mentioned. The next higher trigger level L1 gives an accept or reject within $6.5 \mu\text{s}$. Enough time to do more complex analysis like electron identification with the TRD, coarse momentum determination (low/high p_T) or topological cuts. The third trigger level L2 prevents recording events with pile-up. As the interaction rate is predicted to be 8 kHz in lead-lead collisions there is a non-negligible probability that within the drift time of the TPC of $92 \mu\text{s}$ a second collision is recorded that might spoil the previous event. To ensure that only pure events are recorded the L2 rejects events where a subsequent collision caused signals in the detector within the drift time interval. The fourth level L3 or High Level Trigger enables already the complete reconstruction of an event within a few ms. Of course this cannot be done with the same precision as done in the offline reconstruction but still it is possible to especially reject events which do not contain signals of interest but caused one of the lower level triggers. Doing so the High Level Trigger will reduce the recorded data volume significantly.

Data acquisition scenarios

The main constraint put by the data acquisition system to the recorded data is the bandwidth, meaning the maximum amount of data that can be stored and processed per second. Due to technical reasons the maximum bandwidth is limited to 1.25 GB/s. This bandwidth has to be shared between the possible trigger configurations. In principle a minimum bias event rate of 8 kHz as expected for lead-lead beams at the LHC (see section 3.1) would be more than enough to fully utilize the data acquisition system. Since this would not allow the measurement of rare probes which strongly depend for example on the dielectron trigger, the bandwidth has to be shared among different trigger scenarios. The planned trigger scenarios taken from [Car04b] are shown in table 3.3.

Scenario 1 refers to an unbiased data acquisition like it will happen for the first data taking periods. Given this scenario, in one ALICE running year⁶, $2 \cdot 10^7$ central, $2 \cdot 10^7$ minimum bias and $6.5 \cdot 10^8$ muon arm events will be recorded. However since this amount of events is not sufficient to do quarkonium physics at reasonable statistics (compare to table 2.2) scenario 2 was proposed to meet the minimal requirements for quarkonia physics with expected 10^8 recorded dielectron events and

⁶one ALICE running year corresponds to 1 month (= 10^6 s) of lead-lead beam and 10 month (= 10^7 s) of proton-proton beam.

Table 3.3: Data taking scenarios for lead-lead beams.

	Scenario 1 Rates		Scenario 2 Rates		Scenario 3 Rates		Scenario 4 Rates	
	Max.	Rec.	Level 2	DAQ	Level 2	DAQ	Level 2	DAQ
Central	10^3	20	10	10	20	20	20	20
Minimum Bias	10^4	20	10	10	20	20	20	20
Dielectron			100	100	200	20	200	20
Dimuon	1000	650	1600	1600	1600	1600	1600	1600
Total throughput (MB/s)	1250		1400		1400		700	

$1.6 \cdot 10^9$ muon arm events. For this scenario the bandwidth exceeds the maximum bandwidth, but since the event sizes were calculated with the maximum expected charged particle multiplicity of 8000 charged particles per unit rapidity one expects smaller event sizes for real events. In addition it has been shown that for the TPC the data can be compressed by a factor of two without losing any physics information [Nic03]. Other compression algorithms are under investigation, of course these compressions will only be applied if it was proven that they do not influence the physics results. This especially applies for the High Level Trigger, used in the scenarios three and four. In scenario three it is assumed that dielectron events triggered with an L2 rate of 200 Hz can be reconstructed by the High Level Trigger online thus a total rate of $2 \cdot 10^8$ events are inspected for dielectrons without a significant increase in bandwidth consumption. In scenario four the High Level Trigger is used to further reduce the data volume. This can be achieved in different ways. One example is the exclusive readout of regions of interest or another one the usage of preprocessed tracking data provided by the High Level Trigger.

Chapter 4

Quarkonia measurements with the ALICE central barrel

4.1 Simulation framework

The importance and physical relevance of the measurement of quarkonia has been reported in chapter 2. Now the performed studies on the measurements of quarkonia in the ALICE central barrel in lead-lead collisions are presented. The evaluation of the detector performance with respect to quarkonia is of major importance even before the first real data taking. The first reason is the justification of the chosen detector design. The second reason is to set a baseline on the physical results with respect to the recorded statistics. So one could summarize the work presented in this chapter by asking the following questions:

1. Can ALICE measure quarkonia in the dielectron channel?
2. Which quarkonia states can be observed?
3. What is the expected significance of the individually observed quarkonia states?
4. Is the significance of the measurement sufficient to observe suppression or enhancement?

Similar studies have been carried out for the muon arm of ALICE [Mar05, Mar06, Ale06d, Cro06], as well as for other LHC experiments with a heavy-ion program [Bet02, Bed07, Wos07, Gra07]. The way to perform these simulations is very similar. Since the aim of the simulations is to give an realistic estimate of the performance one would like to simulate the expected amount of recorded events with the quarkonia rates reported in table 2.2. These quarkonia signals shall then be embedded into a *realistic* background event. The produced event is then propagated through the detector to include acceptance, resolution and efficiency effects. After

that the remaining particle tracks are analyzed. For the reconstruction of quarkonia this analysis is basically the calculation of the invariant mass for dielectron pairs.

For one ALICE running year on the order of $2 \cdot 10^8$ central lead-lead events will be recorded (see section 3.3.4) and the full simulation and reconstruction of one lead-lead event with a multiplicity of 3000 charged particles per unit rapidity takes about a few hours on a modern computer. Due to limited capacities this task cannot be easily performed with the available computer resources. For this reason one has to speed up significantly the simulation and reconstruction of the events. The most time consuming part of the simulations is the full simulation of the detector response and the subsequent reconstruction of the particle tracks. Instead of using this complicated numerical calculations the idea is simply to use a detailed parameterization of the detector performance for electrons and pions.

All the simulations are run under the standard ALICE software framework *aliroot* [Ali07]. Aliroot offers a large variety of standard particle generators like PYTHIA [Sjo06] or HIJING [Gyu94] as well as especially designed generators used to produce specific signals like quarkonia with rapidity and momentum distributions expected for the LHC collision energies. Further on the whole experimental setup is parameterized in aliroot. The detector response can be simulated using different detector simulation programs like GEANT3 [Bru87], GEANT4 [Ago02] and FLUKA [Fer05, Fas03]. After the calculation of the deposited energy in the detector, digitization routines provided by the different detector groups can be used to produce realistic *signals*.

As a third part aliroot contains the whole ALICE reconstruction and calibration routines. These routines are strictly separated from the simulation to ensure that the reconstruction can be run on measured events. The fourth part of aliroot are analysis libraries. This fourth part will be described in more detail in section 5.2.

4.2 Expected quarkonia yields

In heavy-ion collisions it is always the question whether an observed signal arises purely from overlaying a certain number of elementary nucleon-nucleon collisions or if the signal can be attributed to a collective behavior of the produced hot and dense nuclear matter. Since the presented simulations represent baseline predictions for the observation of quarkonia we concentrate on the signal one would expect if a certain number of nucleons collide. The intention is not to simulate any predicted anomalous quarkonia suppression but to give a reliable prediction of the baseline in quarkonia measurements. The implications on the current competing models on quarkonia suppression on these measurements will be discussed in section 4.7.

The performance of the quarkonia measurements shall be simulated as realistically as possible. Hence the input to the simulations, namely the expected yields per event have to be calculated using the latest predictions for LHC energies. The yield of production for each individual quarkonium state consists of four compo-

Table 4.1: Masses, decay width and branching ratios to electron-positron pairs for the simulated quarkonia states [Yao06].

System	mass [MeV/c ²]	width [keV/c ²]	Br(e^+e^-) [%]
J/ψ	3096.916 ± 0.011	93.4 ± 2.1	5.94 ± 0.06
ψ'	3686.093 ± 0.034	337 ± 13	0.735 ± 0.018
Υ	9460.30 ± 0.26	54.02 ± 1.25	2.38 ± 0.11
Υ'	10023.26 ± 0.31	31.98 ± 2.63	1.91 ± 0.16
Υ''	10355.2 ± 0.5	20.32 ± 1.85	seen ($\approx 1.$)

nents:

1. the production cross section of the corresponding heavy quark pair in nucleon-nucleon collisions
2. the branching ratio to dielectrons
3. nuclear shadowing to attribute for cold nuclear matter effects
4. a scaling factor obtained from Glauber model calculations to scale the results to lead-lead collisions by the number of binary nucleus-nucleus collisions

Each component is described in the following.

Quarkonia production

The first component was already described in section 2.2. The values used for the simulations are taken from table 2.2 for quarkonia production for J/ψ , ψ' , Υ , Υ' and Υ'' for 5.5 TeV proton-proton collisions. As the collisions at the LHC will exceed the collision energies of the currently highest available energies for proton-proton collisions performed at the Tevatron by a factor of 3 (1.96 TeV compared to 5.5 TeV) the production cross sections include a rather large uncertainty factor of at least a factor of 2. Nevertheless these cross sections are used for all ALICE physics simulations [Ale06b] and especially for the simulation of quarkonia within the Muon Arm.

Dielectron branching ratios

The branching ratios for quarkonia decaying into electron positron pairs have been taken from [Yao06] and are shown in table 4.1. For the Υ'' state no measured branching ratio to dielectrons exists, a value of 1% was used.

Table 4.2: Used values for cold nuclear matter effects [Ale06d].

state	$c\bar{c}$	$b\bar{b}$	J/ψ	ψ'	Υ	Υ'	Υ''
C_{CNM}	0.65	0.84	0.60	0.60	0.76	0.76	0.76

Cold nuclear matter effects

The measurements presented in section 2.4 showed the need for precise knowledge of the modification of quarkonia production in cold nuclear matter [Bed04]. Although a commonly accepted theoretical model to calculate the various effects is still missing, it has been shown that nuclear shadowing and anti-shadowing as well as nuclear absorption are present in heavy-ion collisions. PHENIX d-Au measurements [Adl05a] showed that cold nuclear matter effects are smaller at RHIC energies compared to SPS energies leading to the prediction that the effects might be even smaller at the LHC. This observation is seen as a relativistic effect: The higher the energy of the collision, the more the two nuclei are Lorentz contracted, such that at LHC, the collision can be seen as the collision of two gluonic discs. Reaction products traverse less nuclear matter than in lower energetic collisions.

Nevertheless cold nuclear effects were included in the presented simulations to give a prediction of the quarkonia baseline starting from today's knowledge. The chosen value for nuclear shadowing for the different contributions is taken from [Ale06d] and is consistent with simulations for the Muon Arm. The values were chosen such that the resulting shadowing is in agreement with the EKS98 [Esk98] parameterization on cold nuclear matter effects. Table 4.2 shows the factors used for central events.

Glauber model scaling

Without assuming any collective phenomena like the described quarkonia suppression one would expect a lead-lead collision to be a superposition of a certain amount of elementary nucleus-nucleus collision. The amount of elementary collisions is given by the geometry of the colliding nuclei. A very sophisticated and widely used approach to calculate the number of elementary collisions is the Glauber model [Gla70b]. A detailed review and examples for applications can be found in [Bia76, dEn03, Mil07, Shu03, Bro01]. Within this model which can be applied to nucleus-nucleus as well as nucleon-nucleus collisions, the nucleus is modeled using a Woods-Saxon distribution [Woo46] for the nuclear density of the form:

$$\rho(r) = \frac{\rho_0}{1 + e^{\frac{r-R}{a}}} \quad (4.1)$$

The resulting density profile of a lead nucleus is shown in figure 4.1. This density profile is then used to calculate the *nuclear thickness function* which gives the

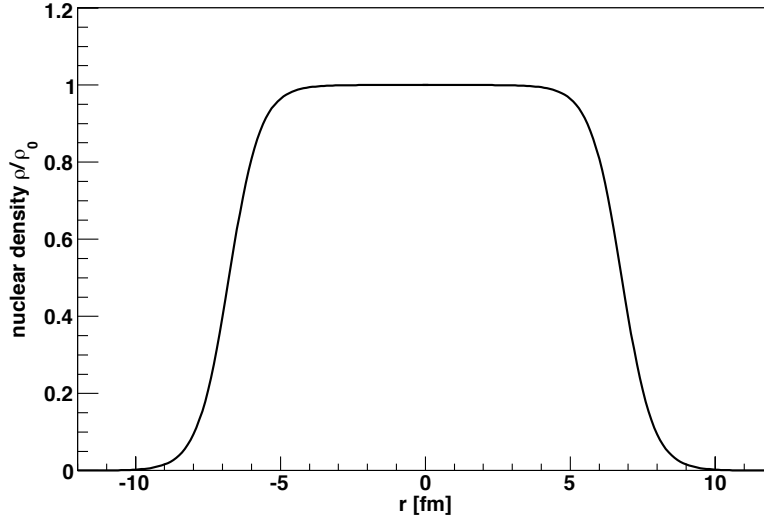


Figure 4.1: Density profile of a lead nucleus described by the Woods-Saxon parameterization. The density is almost constant in the center and falls off steeply at the edges.

number of nucleons $T_A(b)$ in the nucleus A along the path z separated from the center by an impact parameter b :

$$T_A(b) = \int dz \rho_A(b, z) \quad (4.2)$$

normalized such that

$$\int d^2b T_A(b) = A. \quad (4.3)$$

This function is valid for nucleon-nucleus collisions. To extend this picture to nucleus-nucleus collisions one defines the *nuclear overlap function* as the convolution of the two nuclear thickness functions:

$$T_{AB}(b) = \int d^2\vec{s} T_A(s) T_B(|\vec{b} - \vec{s}|). \quad (4.4)$$

Where \vec{s} is a position vector in the transverse plane and \vec{b} is the impact parameter between the two nuclei. Analog to the nuclear thickness function the nuclear overlap function is normalized such that:

$$\int d^2b T_{AB}(b) = AB. \quad (4.5)$$

With the overlap function one is able to calculate the cross section of a specific process in ion collisions σ_{AB} from the elementary cross section of this process in

nucleus-nucleus collisions σ_{NN} :

$$\sigma_{AB} = \int d^2b \left[1 - e^{-\sigma_{NN}T_{AB}(b)} \right] \quad (4.6)$$

In addition T_{AB} can be used to calculate the average number of elementary inelastic collisions $\langle N_{coll} \rangle$ for a given impact parameter b . The average number of collisions is simply given by the probability that two nucleons interact σ_{NN} and the amount of overlap, meaning the number of nucleons that come close to each other:

$$\langle N_{coll} \rangle(b) = \sigma_{NN} \cdot T_{AB}(b). \quad (4.7)$$

However the impact parameter b is not a directly measurable quantity in heavy-ion collisions. The impact parameter can within the presented Glauber model calculations be related to the centrality of an event. The assumption is that the more central ($b \rightarrow 0$) a collision is, the more particles are produced, thus the measured charged particle multiplicity can be used to determine the centrality of the collision. Since the temperature and pressure are maximal for the most central collisions these studies focus on the 10% most central events. The corresponding impact parameter range is determined using the following definition [Vog99]:

$$f_{geo}(b_1 < b < b_2) = \left[2\pi \int_{b_1}^{b_2} b db \left(1 - e^{-\sigma_{NN}T_{AB}(b)} \right) \right] / \sigma_{AB}^{geo}. \quad (4.8)$$

f_{geo} denotes the fraction of the total geometric cross section σ_{AB}^{geo} with the impact parameter b .

One should keep in mind that this definition implies wounded nucleon scaling meaning that the number of nucleons that are struck at least once by the incoming nucleus (and thus the nucleon is *wounded*) and scattered inelastically with the cross section σ_{NN} are counted. σ_{NN} denotes the inelastic scattering cross section for elementary nucleus-nucleus which is predicted to be 55.6 mb for LHC energies [dEn03].

The results obtained by using the described formalism are summarized in table 4.3. For the presented studies the number of collisions for the 10% most central events is used to scale the elementary nucleon collisions to lead-lead collisions.

Calculation of quarkonia yields

As a summary the final quarkonia yields are given in table 4.2. The yields per event for each type were calculated using

$$Y_{Q\bar{Q}} = \frac{\sigma_{Q\bar{Q}} pp(5.5 TeV)}{\sigma_{inel}(5.5 TeV)} \times N_{coll} \times C_{CNM} \times Br_{type}(e^+e^-) \quad (4.9)$$

$\sigma_{Q\bar{Q}} pp(5.5 TeV)$ is the production cross section, $\sigma_{NN} = 55.6$ mb the inelastic nucleon-nucleon cross section. It is used to normalize the quarkonia production cross section to one elementary event to get the expected yield per event. C_{CNM} is the factor accounting for cold nuclear matter effects and N_{coll} the number of collisions from the Glauber-Model calculations. The resulting yields are now used as input to the particle generators for quarkonia generation (see table 4.2).

Table 4.3: Glauber model calculations for different centrality classes calculated using equations 4.8 and 4.7

f_{geo} [%]	b [fm]	N_{coll}
0-10	0-5.1	1297
10-30	5.1-8.8	608
30-50	8.8-11.3	184
50-70	11.3-13.3	39
70-100	13.3-16.0	4
Min bias	0-100.0	312

Table 4.4: Calculated yields per lead-lead event for the different quarkonia states decaying into dielectrons as a function of centrality.

Cent. [%]	J/ψ	ψ'	Υ	Υ'	Υ''
0-10	2.0e-2	3.8e-4	1.6e-4	4.5e-5	1.4e-5
10-30	9.6e-3	1.8e-4	7.8e-5	2.1e-5	6.5e-6
30-50	3.1e-3	6.0e-5	2.4e-5	6.7e-6	2.0e-6
50-70	7.4e-4	1.4e-5	5.5e-6	1.5e-6	4.6e-7
70-100	9.7e-5	1.9e-6	6.7e-7	1.8e-7	5.6e-8
Min bias	5.4e-3	1.0e-4	4.2e-5	1.1e-5	3.5e-6

4.3 Event cocktail

To simulate the performance of the ALICE central barrel measurement of quarkonia one needs all components contributing either to the signal or to the background. Apart from the calculated yield of quarkonia states the generation of quarkonia shall be performed in an almost realistic way. Since measured transverse momentum and rapidity distributions are only available for proton-proton collisions of 1.8 TeV [Abe88] the distributions for 5.5 TeV have to be scaled to account for the higher energy. The scaling has been performed using either predictions from the Color Evaporation Model or wherever possible the measured spectra at the highest available energies were used for scaling. For the transverse momentum distributions, measurements by the CDF experiment were fitted with the function $f(p_t) = cp_t/(1 + (p_t/A)^2)^n$. The obtained functions were then extrapolated to LHC energies using the behavior of $\langle p_t \rangle$ with increasing \sqrt{s} predicted by the Color Evaporation Model [Acc04]. The distributions used for quarkonia are shown in figure 4.2. The generators for higher quarkonia states ψ' , Υ' and Υ'' use the same transverse momentum and rapidity parameterizations as for the ground states. For the rapidity distributions one assumes for the relevant rapidity interval of $|y| < 0.9$ a flat distribution for the generated quarkonia states which is supported by PHENIX measurements on the J/ψ [Ada06b].

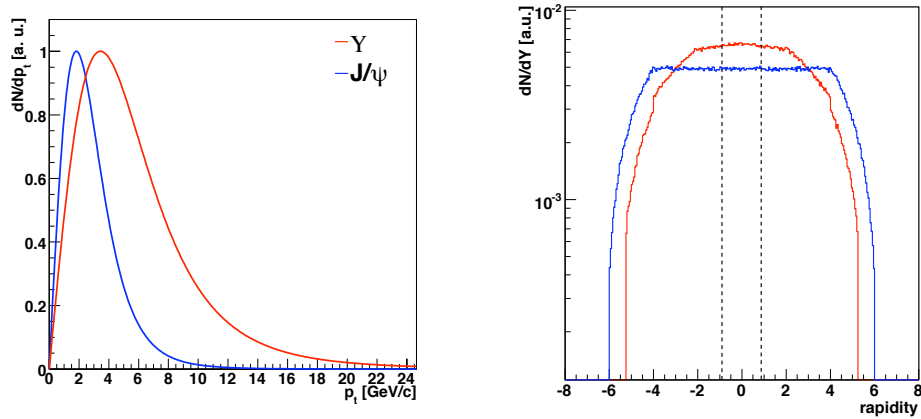


Figure 4.2: Transverse momentum (left) and rapidity (right) distributions of the generated J/ψ - and Υ -family. The dashed lines indicate the acceptance of the Central Barrel.

Apart from the signal also the background has to be simulated. The expected sources for background are:

1. single electrons from charm and beauty decays
2. hadrons from charm and beauty decays misidentified as electrons
3. other hadrons misidentified as electrons

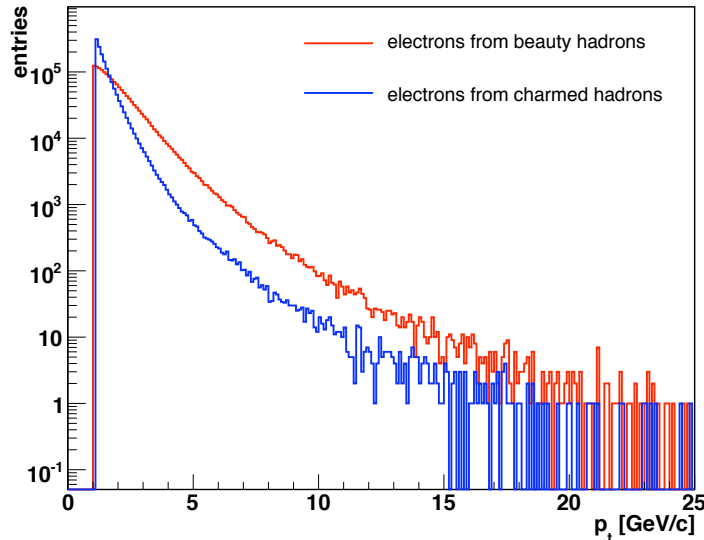


Figure 4.3: p_T spectra of electrons originating from semi-electronic decays of charm and beauty hadrons as simulated for the presented studies. A single electron p_T cut of 1 GeV/c was applied.

4. electrons from γ conversions

Higher quarkonia states decay into the lower mass states and thus contribute to the total yield. These states are not regarded as background contributions to the total yields as they are already included in the quarkonia cross sections given in table 2.2.

The background contributions have to be included in the *cocktail* event. Electrons and hadrons from charm and beauty decays are simulated using a parameterization for the generation of charm and beauty hadrons and baryons. As the kinematical distributions for quarkonia, the used distributions for charm and beauty mesons were extrapolated from the highest available energies. Since hadrons containing charm or beauty quarks decay hadronically as well as semi-electronically they contribute via two channels to the background: directly via decay electrons or indirect via misidentified pions. As the p_T spectrum of the charm and beauty decay products has significant entries in the high- p_T region (see figure 4.3), charm and beauty are expected to contribute significantly to the background in the high-mass region, there especially to the background in the region of the Υ -family. However within the final analysis there might be an option to suppress the background arising from charm and beauty decays using the high vertex resolution and the resulting detection of the displaced decay vertex (see also section 5.6). Since the presented studies use conservative estimates on background contributions, the suppression due to the secondary vertex reconstruction is not taken into account.

To simulate an almost realistic hadronic background of a lead-lead event a pa-

parameterized HIJING [Gyu94] generator was used. This generator produces pions and kaons with the relative rates and transverse momentum distributions as measured by the CDF collaboration [Abe88] and the particle production depending on pseudo-rapidity obtained by using full HIJING simulations. 87% of the produced particles are pions while π^0 , π^+ and π^- are produced in equal amounts. The remaining 13% of particles are equally distributed as K_{long}^0 , K_{short}^0 , K^+ and K^- . The total amount of produced particles within the detector acceptance was adjusted such that it matches the expected multiplicity of $dN/dy_{ch} = 3000$, already discussed in section 3.2. The contributions to the background originating from photon conversions are not taken into account. The reason is that since the conversions happen within the detector material, the impact parameter between these tracks and the primary vertex is large. This enables a very efficient reconstruction of these conversions and thus the expected contribution to the dielectron invariant mass spectrum is negligible.

4.4 Evaluation of the detector performance

As it was already described in section 4.1 the time consuming part of simulating the detector response and the reconstruction of the particle tracks is replaced by using look-up tables to parameterize the detector response to the traversing particles. Using this approach it is possible to simulate the amount of data that is expected to be recorded in one ALICE running year by reducing the computing time needed to simulate one central lead-lead event from a few hours down to a second. The parameterization of the detector response and the creation of the look-up tables is discussed in detail in [Gro05]. Here only a short summary of the studies is given. The look-up tables have to provide the following informations concerning the detection of a generated particle:

1. Efficiency – is the particle detected?
2. Resolution – difference between generated and reconstructed quantities
3. Particle identification – detected particle type.

The particle properties are examined with respect to the kinematic variables p_T , η and ϕ .

The look-up tables were obtained by full simulation and reconstruction of 5000 events. The event generator used for these event consisted of the parameterized HIJING generator tuned to multiplicities of $dN/dy_{ch} = 4000$ and 6000 and additional electrons and positrons with a flat p_T -distribution. The parameterized HIJING generator was used to simulate a realistic occupancy of the detector needed to explore the multiplicity dependence of the track reconstruction. One of the goals concerning the performance of the quarkonia measurements is to study the specific characteristics of the measurements induced by the energy loss of the electrons, for this reason 1000 electron/positron pairs were embedded, with a flat p_T distribution

between 1 GeV/c and 10 GeV/c. The total number of 1000 electrons increases the occupancy of the detector only by 2.9% but enables detailed studies on the reconstruction efficiency of electrons especially at higher momenta.

To evaluate the detector response concerning efficiency, resolution and particle identification the observed tracks had to fulfill certain quality requirements as well as they had to pass physical cuts. Nevertheless to keep the look-up table as unbiased as possible the cuts were defined in a loose way. The applied cuts are shortly described in the following for a more detailed description see [Gro05]:

- **Reconstruction specific cuts:**

- Lost track cut: If the reconstructed momentum of a track differs more than 50% from the generated one, the track is considered lost and it is not used for the further analysis.
- No matching with ITS: Since the tracking in ALICE starts with the TPC and the found tracks are attempted to be propagated to the ITS [Iva06], sometimes this propagation fails meaning that there is no precise information on the production vertex of the particle. Since in the following analysis quarkonia originating from the primary vertex shall be studied vertex information is desperately needed, tracks without this information are not used for the analysis.
- Doubly found tracks: The reconstruction algorithm sometimes due to technical reasons finds two tracks for one generated particle. Both tracks are very similar and in order not to spoil the efficiency distributions, one of the tracks is removed. This problem is known for the used all-root version and might be solved in subsequent versions.

- **Physical cuts:**

- The most powerful cut in reducing the total amount of tracks is the p_T -cut on single electrons. It was chosen to be 1 GeV/c within the creation of the look-up table as well as for the later presented performance studies. It especially removes electrons originating from conversions of low momentum photons, π^0 and bremsstrahlung. The implications on the J/ψ yield of this cut will be studied in section 5.5.
- Cut on production vertex: Most of the reconstructed particles are not primarily produced but originate from subsequent particle decays or conversions on the detector material. Since it is expected to remove these secondary particles by the reconstruction of their production vertex with high efficiency, here only particles are taken into account which were produced within a cylinder around the primary vertex with a radius (x,y coordinates) of 0.1 cm and a length (z) of 6 cm.

The obtained results for the parameterization of the detector efficiency and resolution are summarized in the following.

Efficiency

The efficiency is defined as the number of tracked particles divided by the number of generated particles. In this case the number of generated particles is defined as the particles generated within the pseudo-rapidity interval of $|\eta| < 0.9$. The parameterization of the efficiency is available as two 2D-histograms. One histogram parameterizing the p_T - θ - the other one the p_T - ϕ plane. This way of parameterization has been chosen since in principal the three parameters p_T , θ and ϕ are not independent. Since a 3-dimensional binning of the parameter-space would have led to very high statistics needed for the simulation, it was assumed that θ and ϕ are independent coordinates with respect to the efficiency. Thus the response function of the form $E(p_T, \theta, \phi)$ can be written as $E(p_T, \theta, \phi) = E_1(p_T, \theta) \cdot E_2(p_T, \phi)$. Wherever possible symmetries of the detector are used to increase the statistics in one efficiency bin. In that respect the segmentation of the central barrel into eighteen sectors in ϕ and the symmetry around the central electrode of the TPC has been used. The obtained results are shown in figure 4.4. The projections of the efficiency onto the ϕ and θ axis clearly reflect the geometry of the detector with the eighteen-fold segmentation in ϕ , resulting in a 20% drop of the efficiency and a 2% drop of the efficiency due to the central electrode of the TPC. The decrease of the efficiency with increasing p_T is explained by the curvature of the tracks. If a low p_T -particle with a large curvature of the track enters a dead area of the detector (like in between the ϕ -sectors) it has a larger probability to enter the detector again than a high- p_T particle with an almost straight track. Consequently this drop of efficiency is not observed in simulations without magnetic field.

Resolution

The resolution as quoted here is defined as the difference between the generated quantity and the reconstructed value. It is given for p_T , θ and ϕ . It was of special interest since the influence of the specific energy loss of electrons on the invariant mass distributions was one of the motivations for the presented studies. Previous studies [Mah04] used a detector parameterization obtained from studies on pions and thus cannot study the effect of the electron energy loss. The obtained parameterizations were obtained in a similar way as the efficiencies, by comparing the generated with a reconstructed quantity. The same cuts as for the efficiency were used.

As it was done for the efficiency parameterization, the parameterization for the resolution was done in the p_T - θ and p_T - ϕ -plane. This results in a very large amount of bins and thus a large consumption of disc space and data access time. For this reason the distributions are parameterized by fit functions. The distributions of the θ - and ϕ -resolution are Gaussian when keeping the other parameters constant. This is expected since they should only depend on the detector resolution. The p_T -resolution shows a asymmetric tail due to the electron energy loss. For the θ and ϕ distributions a fit with a Gaussian was performed while the p_T -distribution was

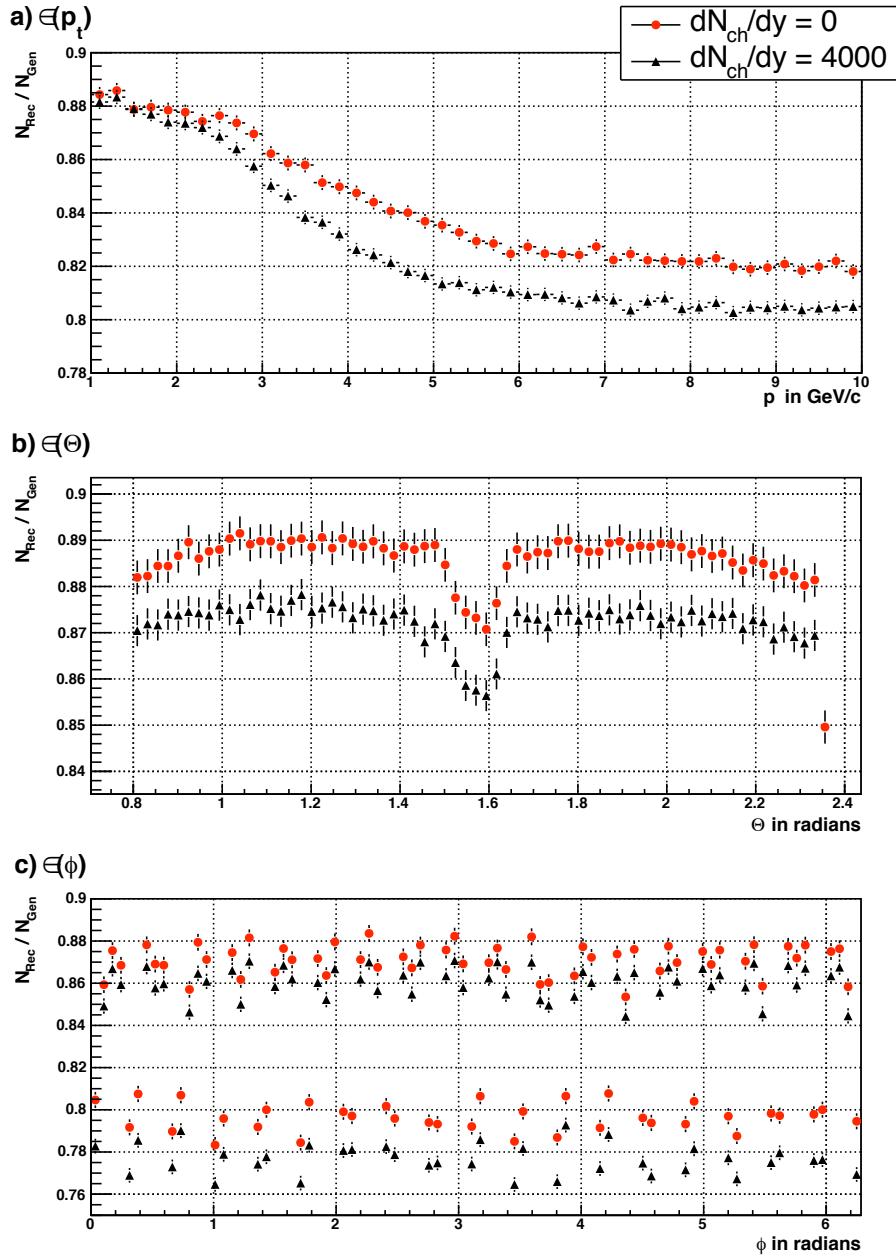


Figure 4.4: The dependency of the reconstruction efficiency of p_T (a), θ (b) and ϕ (c) as used for the presented studies. Efficiencies for $dN/dy_{ch} = 0$ (proton-proton collisions) and 4000 (lead-lead collisions) are shown. See text for details.

fit with a convoluted Landau-Gaussian distribution and to match the tail correctly an exponential function was used. The fit parameters are then used to reproduce the distributions again when used in the look-up table.

To give an impression on how the resolution of a certain variable depends on the other variables projections are shown in figure 4.5. Since the fit parameters of the fit to the p_T -distribution is not very descriptive here the Gaussian σ of the peak is shown. The deterioration of the p_T -resolution with increasing p_T (figure 4.5 a) simply arises from the fact that with increasing momentum particles are less bent within the magnetic field. Since with less bending radius the uncertainty of the measured radius increases (as an extreme case one can assume a straight track meaning infinite bending radius where only a lower limit of the momentum can be given) also the uncertainty of the momentum measurement increases. However this decrease of the momentum resolution is accompanied by an increased resolution for θ and ϕ (figure 4.5 c,d). It is attributed to less multiple scattering that high-momentum particles undergo in contrast to low momentum particles. The spikes in the $\sigma_{p_T}(\theta)$ distribution (figure 4.5 b) reflect the gaps in between the TRD-stacks which lead to the observed lower p_T resolution. The distribution $\sigma_\theta(\theta)$ (figure 4.5 d) can be explained by the diffusion of the charge in the TPC. The charge produced close to midrapidity with $\theta \approx 90^\circ$ has to travel the longest way through the TPC and thus suffers most from the diffusion of charge in the TPC. A similar effect accounts for the distribution of $\sigma_\phi(\theta)$ (figure 4.5 f). Since the tracks with large values of θ need to travel the longest way through the TPC they loose the largest amount of energy due to multiple scattering and specific energy loss and thus the ϕ measurement is stronger distorted than for short tracks.

Particle identification

For the particle identification only the TPC and TRD contribute significantly to the electron-pion separation. When separating electrons and pions one usually defines two quantities: The first one is the electron efficiency ϵ_e defined as the percentage of correctly identified electrons. The second quantity correlated with the electron efficiency is the pion efficiency ϵ_π analogously defined as the percentage of correctly identified pions. The two quantities are correlated via the probability distribution for electrons and pions. Usually after obtaining the distributions one sets a cut on the electron efficiency which then also determines the pion efficiency. In these studies the electron efficiency is set to be 90% for each detector which leads to a combined electron efficiency for TPC and TRD of 81% and a momentum dependent pion efficiency shown in figure 4.7. While the TPC shows the best efficiency in the low momentum region, the TRD basically dominates the discrimination from momenta of 3 GeV/c on. The discrimination in the TPC is done using the specific energy loss in the TPC gas. The dependency of the specific energy loss on the particle momentum is shown in figure 4.6. The specific energy loss of the electrons is almost constant in the momentum range between 1-10 GeV/c. The en-

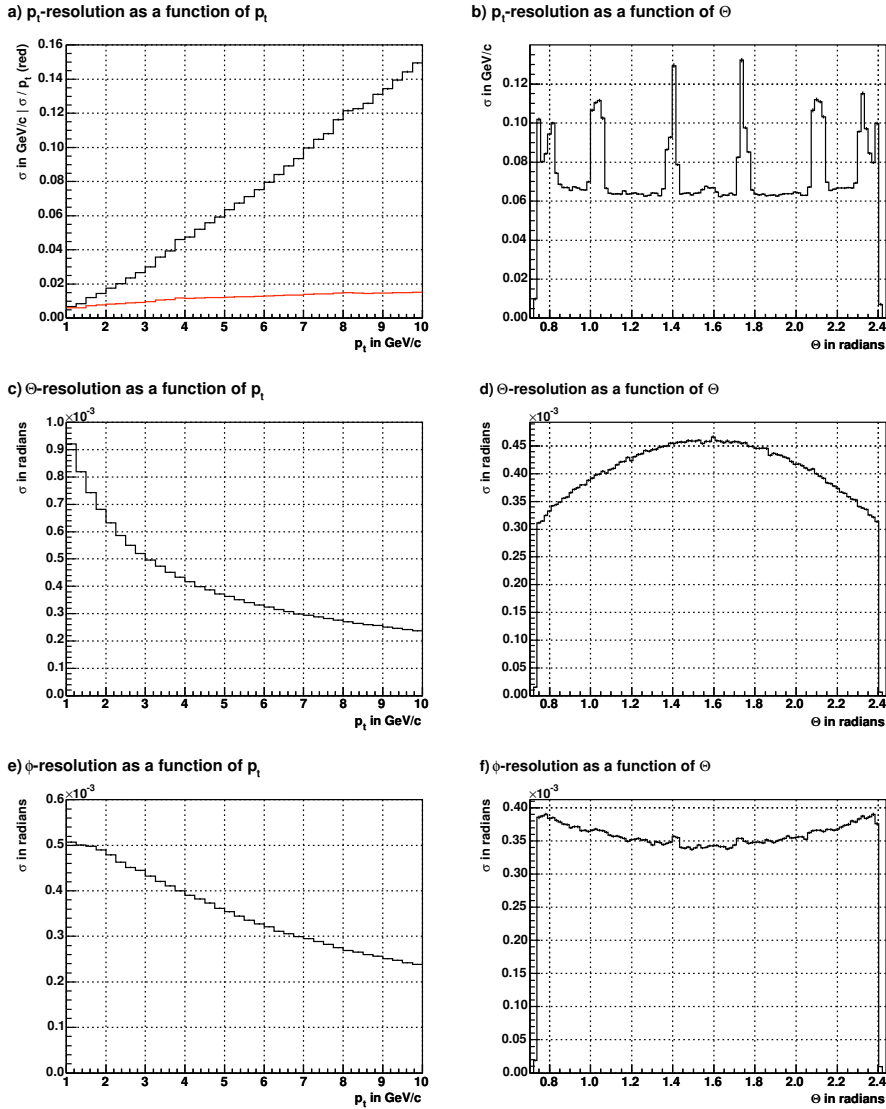


Figure 4.5: Projections of the 2D-histograms showing the p_T and θ dependence of σ_{p_T} (a,b), σ_θ (c,d) and σ_ϕ (e,f). See text for details.

energy loss of the pions is described by the well known Bethe-Bloch formula¹, low momentum pions lose a large amount of energy. With increasing momentum the energy loss approaches a minimum at around 0.6 GeV/c. At this point particles are called minimum ionizing particles. Up to this point pions and electrons can well be separated by their different energy deposition in the gas. With further increasing momentum the energy loss of the pions rises logarithmically until it approaches the electron band at 6 GeV/c. Applying a cut on the electron and pion bands in fig-

¹For a detailed description see [Leo94, Jac99]

ure 4.6 such that the electron efficiency is 90% delivers the momentum dependent pion efficiency further used for these studies. However due to the relativistic rise of the pion energy loss the two bands are only well separated for momenta below 5 GeV/c, for higher momenta the TRD information is used for the separation.

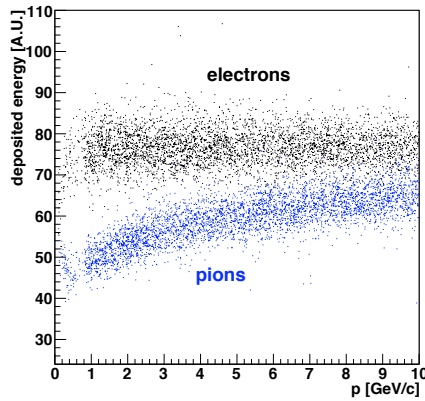


Figure 4.6: Deposited energy of electrons and pions in the TPC gas due to the specific energy loss. A cut on the deposited energy is used for electron-pion separation.

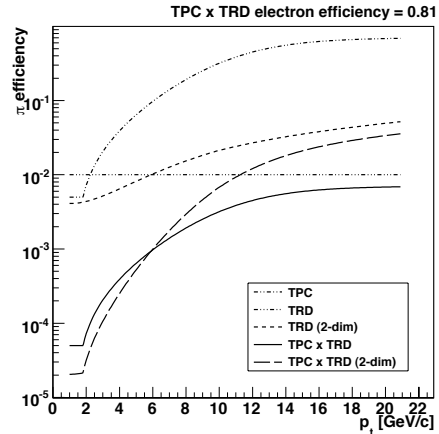


Figure 4.7: Old and new parameterizations for the pion efficiency at a combined electron efficiency of 81%. The influence of the parameterization will be discussed in section 4.6

The way the TRD detects electrons was described in section 3.3.3. Although the particle identification was extensively studied in the same way than the tracking efficiency and the resolution of the electron measurement, the results of these studies will not be used here. The reason is that at the time the performance studies were done the response of the detector with respect to particle identification was not correctly implemented in aliroot. Data collected at a beam test performed in 2004 was believed to deliver more precise data on the momentum dependence of the electron identification with the TRD, however the analysis of this data was not finalized at the time these studies were performed. Finally, also for reasons of compatibility we used the same parameterization as it was used for the studies on open charm and beauty [Ale06c]. So for all the presented studies the parameterization given in figure 4.7 (TPC×TRD) will be used. In the meantime the analysis of the 2004 beam test data made huge progress. A two-dimensional likelihood procedure was used to analyze the recorded data and a momentum dependence of the electron identification could be extracted [Ber07] (TPC×TRD 2-dim), the possible changes due to these new results will be discussed in section 4.6.

4.5 Quarkonia acceptance

A very important characteristic of the detector is the geometrical acceptance. Together with the production rate, the data acquisition rate and the reconstruction efficiency it can be used to give an estimate of the recorded signals over a certain time. While the other parameters have been described previously the geometrical acceptance shall now be evaluated. It is defined as follows:

$$\epsilon_{geo} = \frac{N_{QQ \rightarrow e^+e^-}^{rec}}{N_{QQ \rightarrow e^+e^-}^{sim}} \quad (4.10)$$

Thus it is the ratio of reconstructable versus simulated quarkonia. *Reconstructable* in this context denotes simply whether the two decay electrons are within the detector acceptance. The geometrical detector acceptance for pseudorapidity η and azimuthal angle ϕ is:

$$-0.9 < \eta < 0.9 \quad \text{and} \quad 0^\circ < \phi < 360^\circ \quad (4.11)$$

Defining the detector acceptance this way, dead areas within the detectors like in between TRD super-modules are not included. The drop in detection efficiency due to these areas is parametrized within the look-up tables described in section 4.4. Although it would be more elegant not to split the acceptance this way, the drop in efficiency due to dead zones in the detector is, because of the curvature of the tracks, momentum dependent while the pure geometrical acceptance is independent of the particle momentum.

To evaluate the geometrical acceptance 1 million pure J/ψ and Υ events have been simulated. The decay was forced to the e^+e^- channel, an entry was seen as reconstructed if both electrons were within the above described geometric acceptance cuts. The amount of reconstructed particles depends strongly on the used rapidity distributions. The simulated distributions for the J/ψ and Υ were already shown in figure 4.2. For the J/ψ one obtains an integrated acceptance of 7.69 % and 9.68 % for the Υ . Figure 4.8 shows the detection probability of J/ψ 's and Υ 's with respect to the rapidity. Naturally the probability of detection is maximal for quarkonia produced around midrapidity. For $y = 0$ the detection probability reaches almost 70 %.

Apart from the input distribution a possible p_T cut on single electrons has strong implications on the acceptance. The implications of the single electron p_T cut on the acceptance is shown in figure 4.9. The J/ψ is strongly affected by low p_T cuts. A cut of 1 GeV/c already reduces the acceptance by 25 %.

4.6 Quarkonia performance

4.6.1 Dielectron analysis

Now that all the various inputs, namely the physics inputs like the different ratios of particles as well as the detector inputs to the simulations have been described,

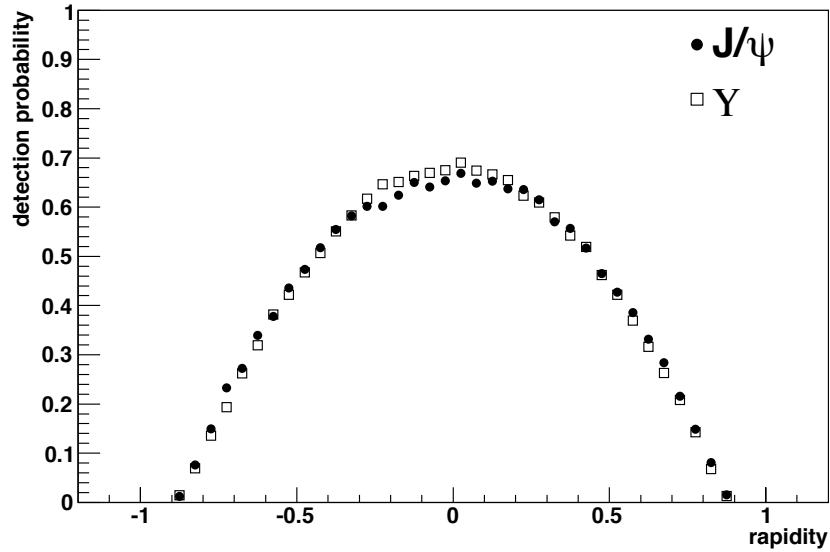


Figure 4.8: Detection probability of J/ψ and Υ as a function of the rapidity of the produced particle. The detection probability includes only the pure geometric acceptance of the detector.

the results of the simulations are presented. In general all results correspond to the expected statistics accumulated within one ALICE running year (see section 3.3.4), so if not else indicated the results correspond to $2 \cdot 10^8$ central lead-lead events. The results were obtained by the analysis of the events generated according to the particle cocktail described in section 4.3, these particles were then evaluated with respect to the efficiency, energy loss and particle identification given in section 4.4. After that each electron was combined with each positron found in one event, calculating their invariant mass. The only cut applied to the single leptons is a cut on transverse momentum of 1 GeV/c. Further studies on possible cuts are presented in sections 5.4 and 5.5.

4.6.2 Invariant mass spectrum

The obtained spectrum is shown in figure 4.10. The peaks for J/ψ , Υ and Υ' are clearly visible. Included in the spectrum are also the various background contributions. The main sources of background are for the lower up to the intermediate mass region electrons from charm decays, while for the high mass region electrons from beauty decays and misidentified pions account for the background. For even the highest mass region the electrons from beauty die out and only pionic background remains.

One should also notice the rather long tails of the resonance peaks towards lower masses. The long tail arises from the energy loss of the electrons with inter-

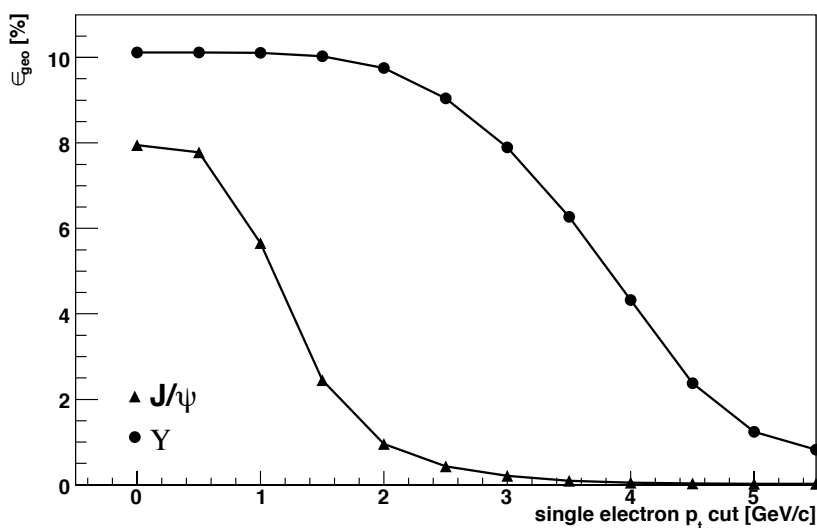


Figure 4.9: Total geometrical acceptance for the J/ψ and the Υ with respect to the applied single electron p_t -cut.

action with the detector material. Consequently this long tail is not observed in the muon decay channel (figure 4.11), there the rather small energy loss of the muons results in an asymmetric peak shape with only a short tail.

4.6.3 Background estimation

To determine the amount of signals present in the invariant mass spectrum one has in principle two options: fitting signal+background together with a combined function or using special techniques to determine the background and then subtract it from the total spectrum to obtain a clean signal spectrum. The first approach is described in the following chapter while this chapter concentrates on the techniques to determine the background. Two commonly used techniques of background estimation shall be described: the event-mixing technique and the like-sign pair technique. Each of these has its specific advantages and drawbacks. In principle both techniques combine measured electrons and positrons in a way that no correlated signals are expected.

The event-mixing technique combines measured electrons with positrons from other events and vice versa. Since the two partners originate from totally independent events the resulting invariant mass spectrum is totally uncorrelated and does not show any correlated signals. A further advantage is that one can combine an almost unlimited amount of events and thus produce an uncorrelated spectrum with higher statistics than the correlated spectrum. However doing this one has to be careful since if the signal to background ratio is very large, the event-mixing technique might create fake background. This can be easily understood if one considers

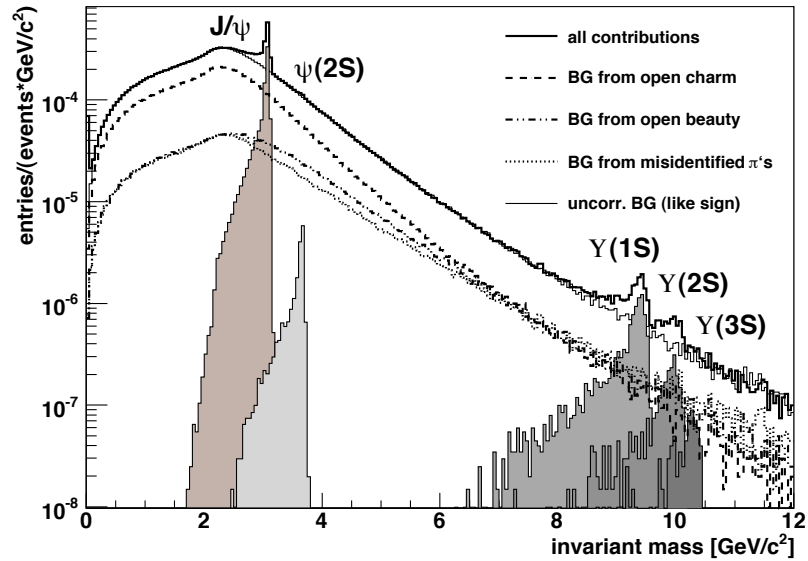


Figure 4.10: The dielectron invariant mass spectrum as obtained by the described simulations. The filled areas indicate the quarkonia input to the simulations. The various contributions from the simulated background are also shown as well as the uncorrelated like-sign background. The histogram is normalized to the total expected statistics of $2 \cdot 10^8$ central events.

background free events where the event-mixing technique will create uncorrelated background were there is none. Another drawback of this method is the normalization. Since from event to event the number of produced leptons fluctuates, even if the same centrality is selected, this will result in non-trivial deviations from the background of the correlated background. Usually the event-mixing background is normalized to the correlated spectrum away from the signal peaks and then subtracted. Of course this imposes a systematic error to the signal determination.

The second technique that shall be evaluated here is the so-called like-sign technique. This technique combines dielectrons with the same sign, i.e. electrons with electrons and positrons with positrons. Using this one assumes that two electrons do not originate from the same physical process and are thus uncorrelated. Since the electrons and positrons are the same that are used for the unlike-sign spectrum the resulting background spectrum is automatically normalized to the signal spectrum. However using the like-sign technique may also contain correlated signals. There are two reasons for correlated signals in the like-sign distribution:

- B^0 -oscillations:
Detailed measurements [Aub02] on the B^0 -meson showed that it oscillates to a rather large fraction into its anti-particle. Knowing this one can think of the following scenario: two b-quarks are created in the initial collision. Both hadronize, while the first one decays semi-electronically with an electron

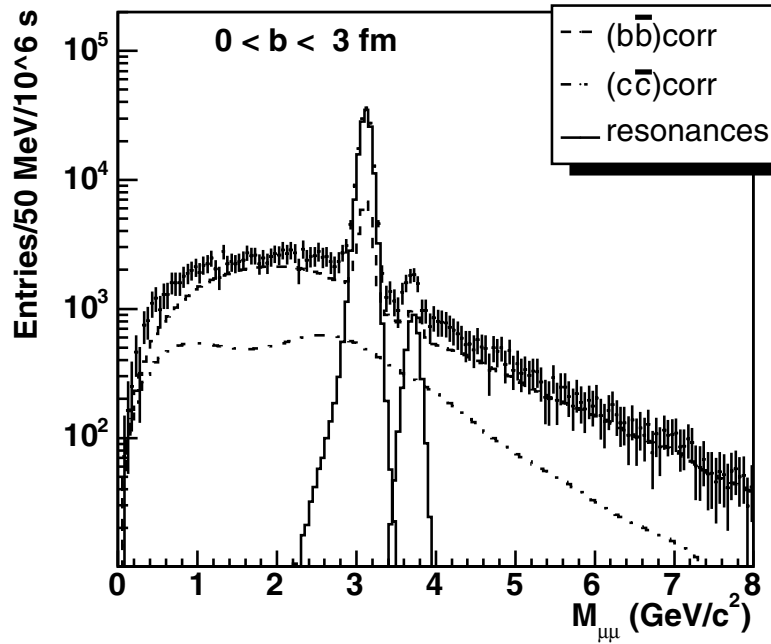


Figure 4.11: Dimuon invariant mass spectrum in the J/ψ mass region as expected for one ALICE running year [Ale06d] in the rapidity range $-2.5 < y < -4.0$. Since muons lose only a small amount of energy through interactions with the detector material, the tail towards lower masses is much less pronounced as for the presented dielectron measurements.

as one decay product, the other one oscillates into its antiparticles and may also decay such that an electron is among the decay products. Since the two electrons arise from the same initial production process they are correlated.

- Decay of B^+B^- :
Charged B-mesons decay with a rather large fraction of about 10% into leptons and D-mesons. The D-mesons with a branching ratio of 12%, in turn might also decay semi-electronically. Thus two or even more correlated electrons arise from one initial $b\bar{b}$ -pair.

Studies including the above described effects [Cro01] conclude that the like-sign background should not be used to estimate the background of the unlike-sign spectrum, since it underestimates the background on the order of 25%. In the meantime it has been shown that also the D-meson oscillates [Aub07], thus the described effects should be studied in the same way for the background arising from charmed mesons. For the presented studies these effects even though it has been shown that their contribution is non-negligible are not taken into account. The possible oscillations of hadrons containing charm and beauty were not simulated and thus do not effect the like-sign distributions. Doing so it was possible to compare the

background obtained by the event mixing with the background from the like-sign technique.

4.6.4 Performance of the quarkonia measurements

The aim of the studies described in this chapter is to give a realistic answer to the question whether quarkonia can be measured with the ALICE central barrel or not and if the answer is yes what the performance of the measurement will be. The performance is measured by three quantities, namely the signal to background ratio, the significance and the total amount of expected signals. The signal to background (S/B) ratio and the significance (SGN) are defined as follows:

$$S/B = \frac{\sum(N_{signal})}{\sum(N_{background})} \quad (4.12)$$

$$SGN = \frac{\sum(N_{signal})}{\sqrt{\sum(N_{signal}) + \sum(N_{background})}} \quad (4.13)$$

While the signal to background ratio is independent of the accumulated statistics, the significance depends on the total amount of recorded events, as well as the total amount of signals. Besides these quantities also the width of the obtained peaks is of importance since it can be used as a measure for the mass resolution of the detector in the various mass ranges of the different quarkonia states.

There are different ways to determine the number of signal and background entries. One simply uses background subtracted spectra, the other one fits the peak and integrates the obtained function. Fitting the obtained invariant mass spectrum shown in figure 4.10 is not straight forward. First of all since the shapes of the various quarkonia peaks differ from each other which can be attributed to the statistical fluctuations present in the corresponding mass range and the detector resolution which decreases significantly for higher masses. The peaks around the resonances show, besides their asymmetric shape, a long tail towards lower masses. To account for the asymmetric peak a convoluted Landau-Gaussian distribution² was used for fitting. However this function underestimates the low-mass tail. For this reason an exponential function was used for the tail. Around the crossover between the exponential and the Landau-Gauss part, an interpolation was used. In addition the background under the peaks is a composite of various contributions to the dielectron

² The Landau distribution describes the energy loss of charged particles in thin absorbers or gases. It is highly asymmetric with a long tail. The distribution can be calculated using

$$f(\lambda) = \frac{1}{\sqrt{2\pi}} e^{-\frac{1}{2}(\lambda+e^{-\lambda})} \quad (4.14)$$

with

$$\lambda = \frac{\Delta E - (\Delta E)_{mp}}{\langle \Delta E \rangle} \quad (4.15)$$

being the normalized deviation from the most probable energy loss. To account for detector resolution effects this distribution is numerically folded with a Gaussian.

spectrum and thus an analytic function derived from first principles that describes the dielectron continuum is not available. For fitting the background either a simple function like a polynomial has to be used or one can use the histograms obtained by the event mixing and like-sign technique. Since the like-sign technique reproduced the shape of the background best, it was used for further studies. For the fit function a polynomial fit to the like-sign histogram was used. Since the ψ' and the Υ'' are only rarely produced fitting did not work for these resonances.

Of course the results of both integration methods depend strongly on the chosen integration limits. Figure 4.12 shows the signal-to-background ratio with respect to significance for different lower integration limits. The same quantities have been evaluated for the other quarkonia states. For each state the integration limits have been chosen such that the values for significance and signal to background ratio become maximal. The limits are indicated as lines in the different quarkonia spectra shown in 4.13-4.15.

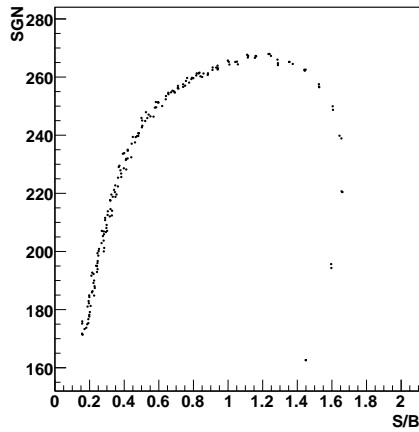


Figure 4.12: Significance versus signal to background ratio for different integration limits. Each point corresponds to a pair of lower and upper integration limits. The final integration limits have been chosen to maximize the significance.

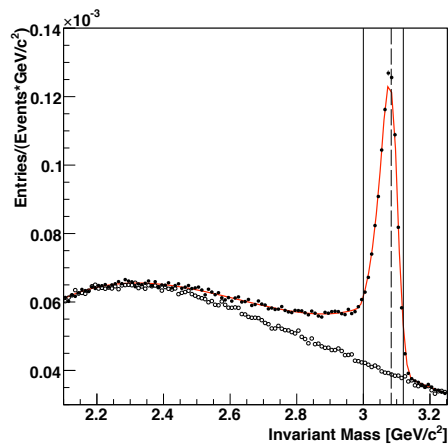


Figure 4.13: The invariant mass spectrum in the J/ψ mass region (full circles). In addition the fit to the spectrum as well as the like-sign background (open circles) are shown.

The obtained results for the described performance parameters are given in table 4.5.

Besides the performance of the measurement the mass resolution of the detector is of great interest. Since the width of the observed resonances is very small (see table 4.1) the width of the observed peak is a direct measure for the mass resolution of the detector. Further on to test the described models on quarkonia suppression it is necessary to be able to differentiate between the individual family members. It is especially of interest to be able to resolve the different Υ -states. Following the

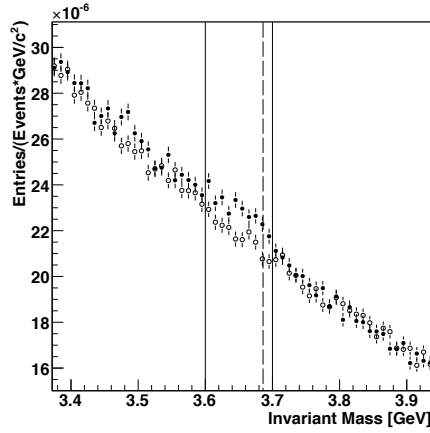


Figure 4.14: The mass region of the ψ' . Due to the low production rate of the ψ' no significant peak can be observed, only a small excess above the background is visible. This small excess was used to extract the significance and signal to background ratio by integrating the signal and background histogram.

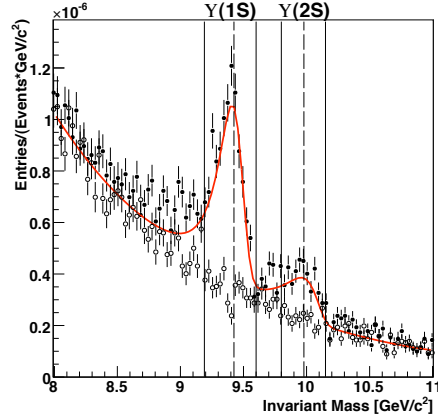


Figure 4.15: The mass spectrum as expected for the Υ family. Clear signals can be seen for the Υ and the Υ' . Due to rather large statistical fluctuations the Υ'' shows no significant signal.

argumentation in [Leo94] two overlapping peaks can be resolved if the distance between their mean values is larger than the full width at half maximum (FWHM). Thus one uses the FWHM as a measure for the resolution in the corresponding energy range. The advantage of using the FWHM is that it is independent of the shape of the peak and can also be applied to very asymmetric peaks as observed in these studies. The obtained values for the J/ψ and Υ are given in table 4.6. One should stress that the obtained resolution for the Υ region is sufficient to resolve the individual $b\bar{b}$ states.

4.6.5 Transverse momentum dependent J/ψ production

As a tool to distinguish between various quarkonia production models the measurement of the p_T distribution of produced quarkonia states can be used. Of course dividing the signals into sub-samples corresponding to the reconstructed p_T of the quarkonia state can only be done if the accumulated statistics is sufficiently large. Exemplarily the possibility to study the p_T dependent production of the J/ψ shall be discussed here.

The J/ψ p_T has been reconstructed using the p_T of the decay electrons delivered by the fast simulator. The sample was subdivided into five p_T bins. The resulting mass distributions are shown in figure 4.16. As a first impression one notices that with increasing J/ψ p_T the background decreases with respect to the signal

Table 4.5: Signal to background ratio, significance and total signal counts obtained by integration of the fit function (*fit*) or the invariant mass spectrum with like-sign background subtracted (*hist*). The results represent the expected statistics of 1 ALICE running year (see section 3.3.4).

		J/ψ	$\psi(2S)$	Υ	$\Upsilon(2S)$
mass window	m_{low}	3.0	3.6	9.19	9.8
	m_{up}	3.12	3.7	9.6	10.15
S/B	<i>fit</i>	1.225	—	1.22	0.48
	<i>hist</i>	1.235	0.05	1.42	0.68
SGN	<i>fit</i>	266.5	—	25.4	10.5
	<i>hist</i>	272.4	10.5	28.4	12.4
$signals$	<i>fit</i>	$1.28 \cdot 10^5$	—	1174	381
	<i>hist</i>	$1.34 \cdot 10^5$	23.	1378	338

Table 4.6: Full width half maximum of the convoluted Landau-Gauss fit as a measure for the mass resolution.

	FWHM [MeV/c ²]	$\Delta E/E$ [%]
J/ψ	65	2.1
Υ	200	2.1

peak, consequently the signal to background ratio shown in figure 4.17 increases with p_T . As the signal to background ratio the total amount of signals as well as the significance of the measurement decreases (see figure 4.18 left and right). As an example five p_T bins were used, resulting in a few thousand J/ψ s within the highest momentum bin.

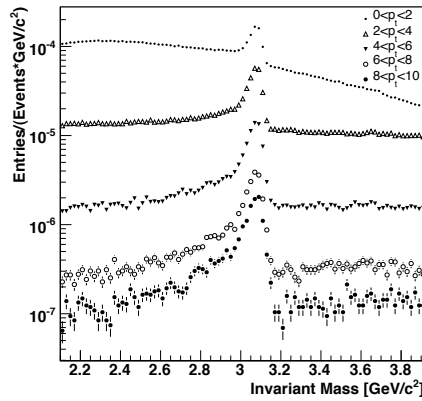


Figure 4.16: The dielectron invariant mass distributions for different values of the J/ψ p_T . The high statistics of the J/ψ would even allow for a finer binning.

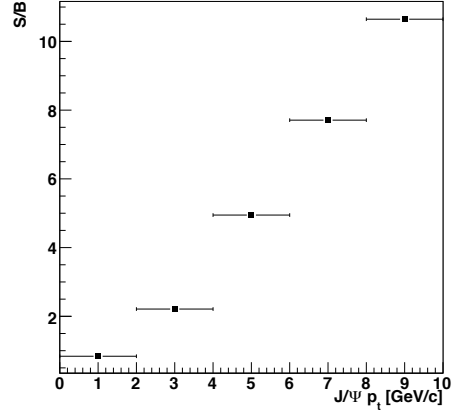


Figure 4.17: As already visible from figure 4.16 the signal to background ratio increases with p_T . Integrating over all p_T bins results in the previously quoted value of $S/B = 1.235$.

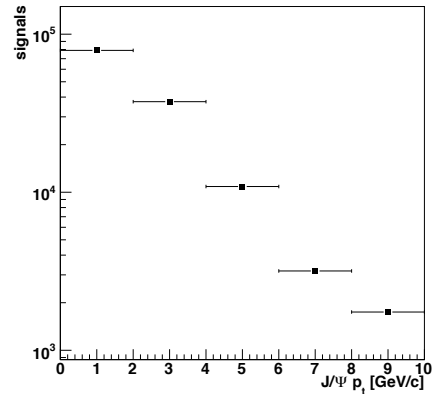
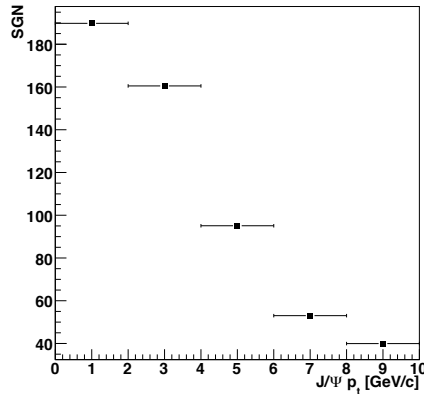


Figure 4.18: The significance decreases naturally with decreasing amount of signals per p_T bin, but also for the highest bin the statistics is sufficiently high for a significant measurement.

4.6.6 Multiplicity dependence

As it was already mentioned in section 3.2 the predictions for the multiplicity of a central lead-lead event are, due to the huge jump in center of mass energy, not very precise. First estimates used for the design of the detector expected 8000 charged particles per unit rapidity, however measurements of the multiplicity at RHIC suggest that the multiplicity expected for the LHC is in the region of 3000. As an upper limit we consider $dN/dY_{charged} = 6000$. The multiplicity affects the measurement in two ways:

1. A large amount of particles results in a high occupancy of the detector. Due to this high occupancy especially the tracking efficiency is expected to decrease.
2. More pions lead consequently to a larger number of misidentified pions contributing to the uncorrelated background and decreasing the performance of the measurement.

The first point was already discussed in [Gro05], as a summary one finds that the resolution does not undergo significant changes when increasing the multiplicity from $dN/dY_{ch} = 4000$ to 6000 and the efficiency slightly decreases by 1%. So within this multiplicity interval the effect of the occupancy can be neglected.

Basically the performance of the measurement is affected by the second point namely the larger amount of pions contaminating the electron sample. Figure 4.18 shows the ratio of the invariant mass spectra obtained using nominal and high multiplicity. As one can see apart from the resonances the uncorrelated background is enhanced by 30%. This leads to a decrease of the performance parameters. For the multiplicity of 6000 one finds a signal to background ratio of 0.94 for the J/ψ and 1.12 for the Υ (1.22 and 1.42 for $dN/dY = 3000$) and for the significance 252.8 and 26.5 (266.5 and 28.4). Although the performance of the measurement decreases with increasing multiplicity even a deviation of a factor of 2 from the nominal multiplicity is not expected to cause serious problems concerning the measurement of quarkonia.

4.6.7 Influence of the TRD electron identification

TRD contribution

To illustrate the contribution of the TRD to the electron identification capabilities, the above described simulations have been performed using only the particle identification provided by the TPC. Since the TRD electron identification capabilities are parameterized as a constant pion suppression factor of 100 (see 4.7) one expects a dramatic increase of accepted pions per event and thus a huge contribution from uncorrelated pion pairs in the invariant mass spectrum. Figure 4.20 shows the invariant mass spectrum using the TPC electron identification only and the spectrum using the TRD in addition. Without the information provided by the TRD, the

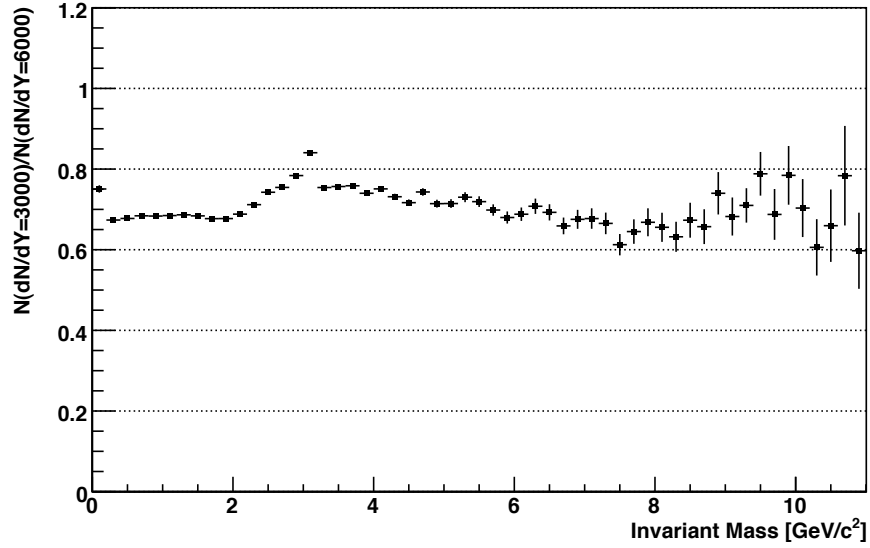


Figure 4.19: Ratio of the dielectron invariant mass spectra for the nominal ($dN/dY_{charged} = 3000$) and the highest expected multiplicity of $dN/dY_{charged} = 6000$. The larger number of pions for the high multiplicity environment leads to a generally higher uncorrelated background and thus to a decrease of the performance.

quarkonia peaks even for the J/ψ are almost not visible. The signal to background ratio drops to 0.006 for the J/ψ and 0.007 for the Υ and the significance is reduced to 30.5 (J/ψ) and 6.2 (Υ). Thus studies on quarkonia would only be possible using different techniques of background subtraction or other, more complicated cut strategies that might be able to reduce the uncorrelated pion background.

New TRD parameterizations

As it was already pointed out in section 3.3.3 the performance of the electron-hadron separation is still under study. For the presented studies a constant pion suppression factor of 100 was used. Analysis of data taken during a test beam performed at CERN in the 2004 imply that the pion suppression will decrease significantly with increasing momentum (see figure 4.21). Even though the analysis is not yet finalized two different parameterizations were extracted one using a one-dimensional (L-Q) and the other one using a multi-dimensional likelihood distribution (L-Q2) [Ber07]. For higher momenta both parameterizations use a straight-line approximation which can be seen as a conservative estimate. As the L-Q2 method has a better pion efficiency for lower momenta and is compared to the constant pion suppression worse for higher momenta the performance for the quarkonium measurement is better for the lower mass J/ψ region and a bit worse for the high mass Υ region (see also figure 4.22). A comparison between the constant, the L-Q1

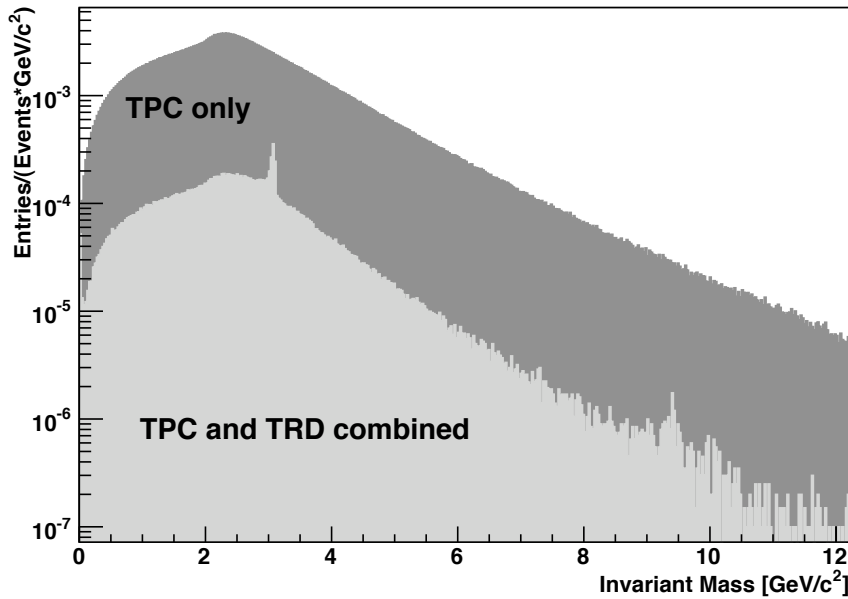


Figure 4.20: The dielectron invariant mass spectrum as obtained by simulating $2 \cdot 10^7$ events (10% of one ALICE running year). The data for the dark grey histogram uses the TPC for electron identification only, the data corresponding to the light grey histogram uses the TRD electron identification capabilities in addition.

and the L-Q2 method is given in table 4.7. Studies on using a neural network algorithm [Wil07] for the particle identification showed an even better performance on the pion efficiency.

4.6.8 Dependence on elementary charm and beauty production cross section

The largest uncertainty to the expected performance of the quarkonia measurement is introduced via the elementary $c\bar{c}$ and $b\bar{b}$ production cross section. As already pointed out in 2.2 the cross section varies between 4-15 mb for $c\bar{c}$ and 0.08-0.34 mb for $b\bar{b}$. The production cross section influences the measurement in two ways:

1. The quarkonia production cross section is proportional to the amount of produced $Q\bar{Q}$ pairs and thus proportional to the elementary production cross section. For this reason the amount of expected signals scales with this cross section.
2. A large part of the uncorrelated background consists of either electrons or misidentified pions originating from hadronic and semi-electronic charm and beauty decays. This background also scales with the production cross section.

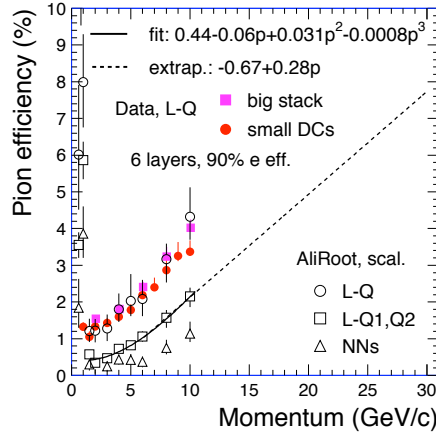


Figure 4.21: Parameterization of the pion efficiency as extracted from the 2004 test beam data [And07a].

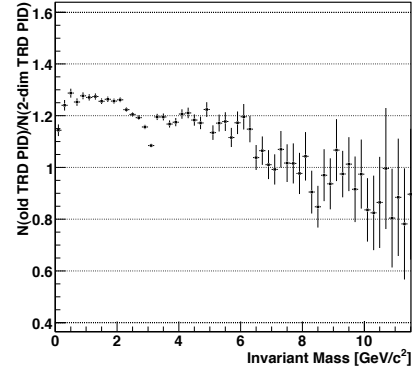


Figure 4.22: The ratio of the invariant mass spectrum using the constant pion suppression factor and the simulations using momentum dependent pion efficiency shown in figure 4.21.

The interplay between these two effects now determines the performance of the measurement. To evaluate the possible implications fast simulations have been performed for three different $Q\bar{Q}$ cross sections. Quarkonia cross sections were assumed to scale proportional to the $Q\bar{Q}$ cross sections. The results are given in table 4.8. The obtained values all show that even with very different cross sections from the nominal one, quarkonia measurements are still possible.

4.7 Suppression and enhancement

It was shown that ALICE is very well suited to measure Quarkonia in the dielectron channel with good significance and resolution. All simulations were performed under the assumption that the lead-lead production yield is determined by the elementary proton-proton cross section, scaled to the number of elementary collisions in central lead-lead events. Apart from the suppression of quarkonium production by cold nuclear matter effects, no suppression or enhancement scenarios were included here. Now the question shall be addressed what will be observed if one includes the dissociation and enhancement models already discussed in section 2.4.3.

First, the case of the J/ψ shall be discussed. The measurements performed at RHIC imply that the energy density at RHIC is sufficiently high to melt the ground state. Assuming that only dissociation effects take place one would expect that apart from a 15-20% contribution of J/ψ 's originating from the peripheral, confined parts of the reaction zone, all J/ψ 's are suppressed as well as the excited states. Thus the observation would be a by a factor of 5 reduced yield and a lower signal to background ratio as well as a reduced significance. However the pure

Table 4.7: Performance of the quarkonia measurement using the constant, a 1-dimensional (L-Q) and the 2-dimensional (L-Q2) pion suppression parameterization.

J/ψ			
TRD PID	const	L-Q	L-Q2
S/B	1.23	1.21	1.47
SGN	266.5	259.1	283.5
Υ			
TRD PID	const	L-Q	L-Q2
S/B	1.42	0.79	1.03
SGN	28.4	25.6	25.0

Table 4.8: Performance of the quarkonia measurement using the lower and upper, as well as the nominal $Q\bar{Q}$ cross section.

	charm			beauty		
$\sigma_{Q\bar{Q}}$ [mb]	4.0	6.64	15.0	0.08	0.21	0.34
	J/ψ			Υ		
S/B	2.06	1.22	0.64	1.61	1.42	0.57
SGN	224.1	266.5	395.9	18.1	28.4	27.6

dissociation models seem to be disfavoured in the explanation of the observed suppression pattern. The models including a production of J/ψ 's at the hadronisation stage seem to explain the RHIC data more precisely. Since the cross section of this production mechanism is directly proportional to the number of produced charm quark pairs, one would expect the yield of J/ψ 's at LHC to be enhanced compared to these studies. As an example the authors from [And06] predict a production cross section of $d\sigma_{J/\psi}^{pp} = 6.4 \pm 3.2 \mu\text{b}$ which is approximately twice as large as the value used for these studies. Thus one would also expect the yield to be twice as large. Which can be observed as a clear deviation from the presented studies.

The second case that shall be discussed, is the case of the Υ family. As already shown in table (2.3) the ground state is expected to survive even temperatures above $4 T_C$ while the excited states melt close to the critical temperature. The question, that nobody is able to answer currently is what the temperature in central lead-lead collisions will be at the LHC. So currently there are no predictions whether the Υ is dissolved or not. Nevertheless the excited states will surely melt, which due to feed-down of these excited states will lead to a reduced yield for the ground state. Since the $b\bar{b}$ pair production at LHC is expected to be on the order of $c\bar{c}$ production at RHIC recombination is not expected to play a substantial role for the Υ . So depending on whether the ground state is going to melt or not one expects two scenarios. If the ground state does not melt, one expects a pattern similar to the one observed for the J/ψ at SPS, with increasing energy density the excited states melt and due to that the ground state yield is reduced by the amount of feed-down. If the ground state does melt, one would expect a similar observation as for the J/ψ at RHIC: since the amount of Υ 's being produced during the hadronization should be negligible and the Υ 's produced in the collision zone center are suppressed, one expects only a small fraction originating from the peripheral part of the interaction zone, where the energy density is too low to produce a deconfined medium with sufficiently high temperature. Naively, since the dissociation temperature is higher for the Υ than for the J/ψ one would expect this contribution to be larger than the 15-20% [Sto07] quoted for the J/ψ . Thus the sequential dissociation model as well as the total dissociation model, including the peripheral production, might be able to describe the observed yield.

Chapter 5

Analysis of primary and secondary J/ψ 's with ALICE

5.1 Idea of the analysis

The previous chapter was dedicated to the evaluation of the expected performance of the future measurements of different quarkonium states. The chosen technique was to simulate a realistic amount of events without a detailed simulation of the detector. This chapter will now evaluate the possibilities to measure quarkonium in the case of the J/ψ using the available tools provided by the ALICE software framework aliroot [Ali07]. The aim is to develop an analysis algorithm that can be used as a starting point for real measurements. In this respect many cuts have been implemented and their implications on the performance has been evaluated. Further on the possibility to separate primary from secondary J/ψ 's originating from the decay of b-flavoured mesons (B -mesons) via their displaced decay vertex has been evaluated.

The basic idea of the analysis is rather simple and was basically already sketched in section 4.1. For each event all electron and positron tracks are combined with each other and the invariant mass is calculated. To obtain an estimate on the uncorrelated background one uses either combinations of particles with the same sign (like-sign distribution) or electrons are combined with positrons from other events (event-mixing). The major background contributions are expected from semi-leptonic decays of charm and beauty-mesons and from misidentified pions. Another large contribution to the total yield of J/ψ 's is expected from the decay of beauty mesons, up to 20 % of all measured J/ψ 's originate from b-decays including either directly the $J/\psi(1S)$ state or higher excited states which in turn decay into the charmonium ground state.

There are many possible cuts that can be applied to increase the performance of the measurement. The following cuts will be discussed in the following:

- cuts on the track quality

- cut on the transverse momentum p_T of the single electron tracks
- particle identification
- topological cuts

The cuts on the quality of the track are not directly related to the underlying physics of the process, but ensures that the information used for the analysis is reliable and the reconstruction of the event worked. As already used for the simulation of the performance in the previous chapter, the cut on the transverse momentum reduces the amount of background electrons dramatically. Although the particle identification is not a direct cut, it assigns the identity of a particle to a measured track and is thus of major importance for this analysis since a large fraction of the background is expected to originate from misidentified pions. The last group of cuts are the topological cuts, which will be especially used to separate primary from secondary J/ψ 's.

5.2 ALICE analysis framework

The design of the ALICE analysis framework [Ali05] is mainly driven by the requirements resulting from the huge amount of data that has to be processed and stored. As already discussed in 3.3.4 the average data taking rate for lead-lead collisions is 1.25 GB/s while one lead-lead running year is 10^6 s. From this one expects 1.25 PB¹ of lead-lead data. For proton-proton runs a bandwidth of 100 MB/s is foreseen and a total running time of 10^7 s, thus the amount of data with 1 PB is comparable to lead-lead runs. Since the experiment is expected to run over at least the next ten years the accumulated raw data has to be completely reconstructed before the next run in order not to generate pile-ups of not processed raw data. For proton-proton data the reconstruction will run online in parallel to the data taking. For lead-lead raw data analysis this is not possible due to the ten times higher data density, for this reconstruction the 4 month winter shutdown each year will be used.

Looking at these requirements it became clear that this task cannot be handled by one single large computer center. For this reason a grid computing concept based on the MONARC [Mon] was adapted to fulfill the above described requirements. The framework is sketched in figure 5.1. According to this sketch the grid is hierarchically subdivided into 3 levels of so-called *Tier centers*. A *Tier* level is defined by the type of the stored data. There are four different types of data:

Raw Data – As recorded by the data acquisition.

ESD – Event Summary Data: Reconstructed data; minimal cuts.

AOD – Analysis Oriented Data: Extrated from the ESDs, only data relevant for a specific type of analysis is stored.

¹ 1 PB = 10^{15} bytes or 1.000 TB

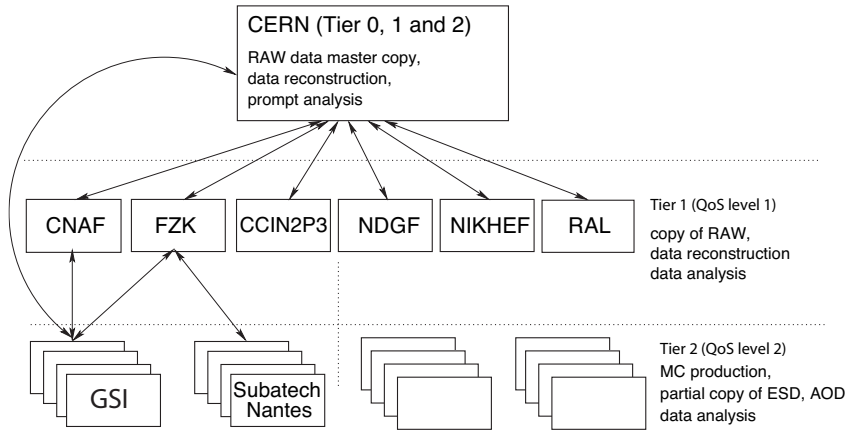


Figure 5.1: Sketch of the proposed structure of the computing grid for ALICE.

TAG – Event tags for event selection.

The grid was designed to handle the huge amounts of data as well as to give physicists access to it for further analysis. The raw data will be kept in the Tier 0 center, namely at CERN, where also parts or even all of it will be reconstructed for the first time. Parallel to this the raw data will be distributed among the Tier 1 centers, usually one large computer center per country. In the Tier 1 centers the raw data will be reconstructed for at least a second time. Due to the huge costs in terms of CPU power to reconstruct the raw data, this task will be done centralized, and since it will probably consume the available computing resources during one ALICE running period, more iterations on the reconstructions need careful planning and cannot be repeated arbitrarily often on the full data set. In addition the Tier 0 center is not foreseen to contribute significantly to the data analysis. The Tier 1 centers will apart from parts of the raw data keep a subset of all ESDs, however via the grid all ESDs will be available for analysis. The Tier 2 centers do not contribute to the reconstruction of the raw data, and will for this reason not store the raw data. Instead the Tier 2 centers will perform the necessary Monte-Carlo production needed for the data analysis. Each center will keep a subset of all ESDs and AODs for data analysis. The next Tier levels are the Tier 3 and 4. Tier 3 centers are planned as medium sized clusters at labs or universities keeping only a small subset of the total amount of the data as a copy. Finally the desktop machine of a physicist doing analysis is regarded as Tier 4.

The AODs represent a more specific version of the ESDs. While during the production of the ESDs any cuts or irreversible changes are avoided, the AODs are produced with respect to the requirements of a specific analysis and might for this reason, as an example, already include cuts on the quality of ESD tracks (see also 5.4) as well as particle identification. In addition results of very CPU intensive algorithms like secondary vertex finding might be performed during the production of the AODs, such that these expensive operations have to be performed only once.

The aim is to reduce the size of the data such that a reasonable amount of data can be stored at Tier 3. The analysis presented here is developed for ESDs. In the future a common framework for all data that has to be analyzed is planned. Using this framework the user can analyze ESDs, AODs and simulated data without changing the analysis algorithm. The specific access to the different data formats is done within different interfaces implemented within the framework, such that a user only has to specify the data sample, but will not have to change the algorithms.

The analysis of data is performed within the framework of an *AliAnalysisTask*. The concept of an analysis task is simple: since a lot of time is spent on reading the data from disks or tape one should perform not only one specific analysis task within one analysis run, but many tasks, to make maximal use of the event currently stored in the memory. To perform an analysis on the complete data set one has to first develop a task derived from a prototype class. Different tasks, which may even depend on each other can then be organized in an analysis train. The input and output of this train is managed by the *analysis manager*. Each task residing in this train is then subsequently executed as soon as the data is available. This system ensures that a lot of tasks can run on the full data set, without too many files being queried at the same time. In addition this system allows to easily activate and deactivate individual tasks according to their requirements with respect to CPU time or disc bandwidth consumption.

For the presented studies on J/ψ -analysis a task has been developed. The task has been run on different data sets to evaluate the implications of the applied cuts with respect to signal as well as possible background contributions. Thus this task should not only be seen as a tool to study the performance of the expected measurements on primary and secondary J/ψ 's but also as one of the first attempts to include a more complicated analysis within the new and still heavily developing aliroot package. One disadvantage of using this framework is that at the time this studies were performed there was no way foreseen to create mixed events. However for these studies the like-sign technique is supposed to give a sufficiently reasonable estimate on the expected background.

5.3 Data samples

To evaluate the implications of the various cuts and conditions, different data sets have been simulated. All simulations were done using the standard simulation and reconstruction of aliroot. The version of aliroot was *4-04-Release*. Since aliroot still undergoes rapid changes, some effects observed during these studies are only present for this particular version and are no more present in subsequent versions. In addition the efficiency of the tracking still changes due to further improvements in the framework. All presented results refer to version *4-04-Release*.

The following samples have been simulated:

1. Pure events containing only primary J/ψ and J/ψ 's originating from B-decays, decaying into dielectrons.

2. Full J/ψ events. One J/ψ , decaying into dielectrons was embedded into a background of charm and beauty hadrons, decaying into all possible channels and a purely hadronic background simulated using 4000 particles generated by the parameterized HIJING generator.
3. Full secondary J/ψ events. B -mesons forced to decay into a channel including a J/ψ , which in turn decay into dielectrons were simulated. These B -mesons were embedded in a realistic background consisting of charm and beauty hadrons, with all possible decays, as well as the 4000 parameterized HIJING hadrons.
4. Pure background events containing only possible sources for background, namely charm and beauty hadrons and parameterized HIJING hadrons.

For the first data set 100 000 events were simulated, however these events were only used to test the developed algorithms. For detailed studies on cut efficiencies the last three data samples were used. For each of them 10 000 events were simulated. To reduce the total amount of data only the Central Barrel detectors were used. Nevertheless each of the three data sets had a total size of 140 GB. The average size of one ESD file was 6.3 MB.

Since the ratio of signal to background events varies a lot in these data samples from the estimates given in table 4.2, the quoted signal to background ratios have been normalized such that under the same cut configuration as used in section 4.4 (only a single electron p_T -cut of 1 GeV/c was used) the signal to background configuration was equal to the ones quoted in table 4.5.

5.4 Track quality cuts

The raw data of the experiment can, due to the limited amount of computing resources, not be reprocessed arbitrarily often. The ESD format was designed such that it stores a maximum of information and it does not apply any cuts on the quality of the reconstructed tracks. To enable cuts on the track quality there are a lot of possible parameters stored parallel to the data to define the quality of a measured track. To understand the meaning of these parameters and to evaluate their implications the tracking procedure shall be briefly described (for details see [Ali05]).

The clusters² used by the reconstruction algorithm are calculated by specific routines individually for each detector. The first step is the determination of the primary vertex which is in this stage not done via reconstructed tracks but from simple correlations between measured points in the Silicon Pixel Detector [Ali05]. This primary vertex can in a later stage be used to try to constrain tracks to it, to separate primary from secondary tracks.

²Cluster denotes a combination of detector channels with a signal above a certain threshold. For most of the detectors not only one channel gives a signal if hit by a particle but the deposited energy is shared among a few channels.

After the vertex determination the tracking starts at the outermost pad row of the TPC. A sketch of the way the tracking takes through the detector is shown in figure 5.2. From the track seed found at the outer TPC wall the algorithm turns inwards towards the center of the detector. Clusters are assigned to a track using the Kalman filter [Ali05]. If the procedure reaches the inner wall of the TPC it tries to find matching clusters within ITS. Especially in an high multiplicity environment this may result in a large tree of possibilities which have to be analyzed with respect to the highest probability. From the inner layers of ITS the Kalman filter tries to find the track in the opposite direction. During this step clusters with a large χ^2 are removed from the track. From the outer wall of the TPC the track is then propagated into the TRD and from there to TOF, HMPID, PHOS and EMCAL. At the last reconstruction step all informations relevant for particle identification are assigned to the track and the track is refitted towards the center of the detector.

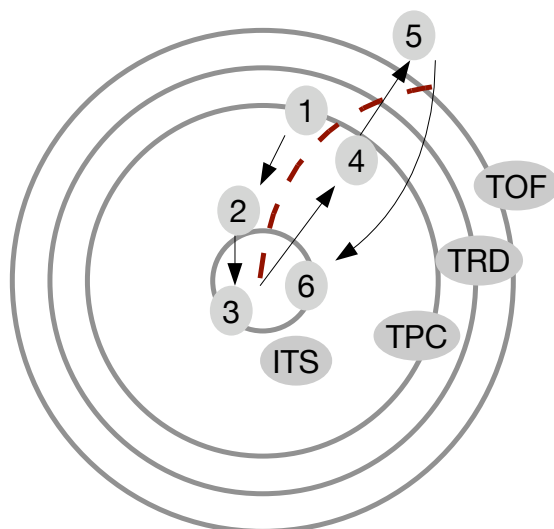


Figure 5.2: Schematic drawing of the way the tracking algorithm for the central barrel works. At each important point the tracking parameters are stored. (1) Track seeding, (2) track matching with ITS, (3) first fit to vertex, store inner parameters, (4) fit of the track outwards, store outer parameters, (5) propagation of the track through TRD and other outer detectors, (6) refit of the track inwards, attempt to constrain track to the primary vertex, constrained parameters.

Following these steps these are the parameters stored in the ESD used to determine the track quality:

Track parameterizations: The five parameters as well as the corresponding error matrix of each track are stored after reconstruction step three, namely

after the track was propagated to the detector center. These parameters are called **inner parameters**. After the track was propagated outwards towards the TRD or even further to TOF or other detectors, the **outer parameters** are stored. If the refit towards the detector center is successful the **refitted parameters** are stored. However all these different parameterizations are only stored if the corresponding reconstruction step was successful. So the simple existence of a parameterization tells something about the quality of the track. From a track originating from the primary vertex or a vertex close to the primary one, one would require all three parameterizations to be present.

Status bit: To give an easy access to the above described information of whether a specific parameterization is present or not as well as to other quality parameters a status word is stored for each track. This status word consists of 32 bits, each bit indicating whether a certain criteria was fulfilled for this track or not. It is stored whether a track was successfully propagated to the inner TPC wall (TPC_{in}), then passed over to ITS (ITS_{in}), fitted back out (ITS_{out}, TPC_{out}), propagated and tracked through the TRD (TRD_{out}) and finally if the refit through all detectors was successful (TRD_{refit}, TPC_{refit}, ITS_{refit}). In addition a bit indicating whether an information on the particle type is present (ITS_{pid}, TPC_{pid} and TRD_{pid}) is set. So for a track coming from the primary vertex, causing signals in all three central barrel detectors one would require ITS_{refit}, TPC_{refit} and TRD_{refit} to be present. The probability that a particle causes a certain status bit to be set was studied for all particles and particularly for electrons. Table 5.1 shows the percentage of all tracks and electron tracks with the refit bit set. To show the dependence on the transverse momentum, the ESD tracks were divided into five p_T -bins. As already discussed the track seeding happens at the outer wall of the TPC, thus naturally the percentage of tracks being refitted through the TPC is highest for all momenta, slightly decreasing for higher momenta. For low momenta the percentage of tracks refitted through the TRD is rather low since lots of the tracks do not reach the TRD due to the bending in the magnetic field.

Number of clusters: A very important parameter is the measured number of clusters (N_{Cls}). One might think of very nicely reconstructed tracks consisting out of only a few measured points. Informations on such tracks cannot be seen as reliable and thus one might want to exclude these tracks. Especially for vertex reconstruction one requires at least one hit in one of the Silicon Pixel Detectors and hits in most of the other Silicon Detectors, resulting in a minimum number of clusters of four. Typical distributions of the number of clusters for ITS, TPC and TRD are shown in figures 5.3-5.5.

χ^2/N_{Cls} **test:** As a measure for the quality of the fit to the track the χ^2 [Leo94] of each fit is stored. For a good fit the quantity χ^2/N_{Cls} should be close to one. Figure 5.6 shows the distributions of the χ^2 values. Table 5.3 shows the influence of three different cuts on the information stored in the ESD tracks

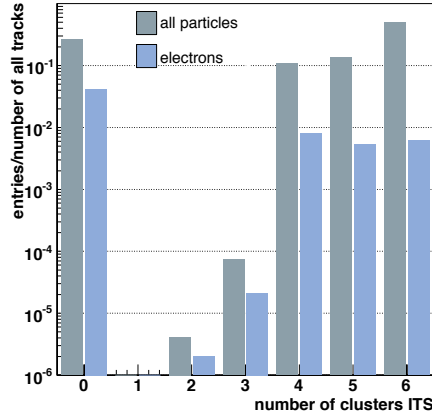


Figure 5.3: The distribution of number of ITS clusters attributed to an ESD track. The maximum number of six clusters reflects the structure of the six layers of the ITS.

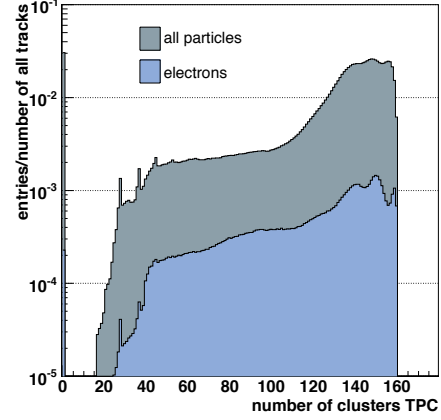


Figure 5.4: The distribution of TPC clusters attributed to an ESD track. The maximum number of clusters is 160 since the TPC has in total 160 pad-rows.

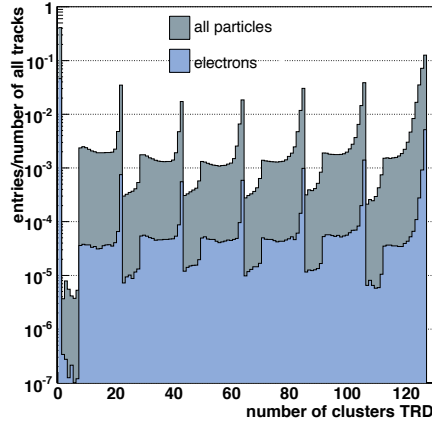


Figure 5.5: The distribution of the number of clusters for the TRD. The distributions reflects the six layers of the TRD, the maximum number of clusters for one chamber is 21.

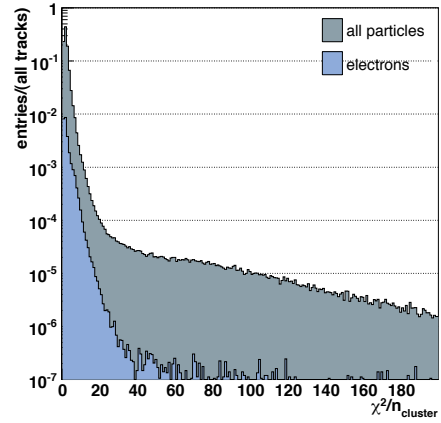


Figure 5.6: The distribution of χ^2/N_{Cls} for ITS as an example for the distribution of all detectors. The distribution for electrons is more narrow than the distribution for all tracks. Tracks with too large χ^2/N_{Cls} values are rejected since the fit and the corresponding momentum components cannot be seen as reliable.

for each of the three detectors. To show the dependence on the momentum, the data set has been divided into five momentum bins.

Table 5.1: ESD tracks with ITSrefit, TPCrefit and TRDrefit bit set.

p_T bin [GeV/c]	ITSrefit set [%]		TPCrefit set [%]		TRDrefit set [%]	
	all	electrons	all	electrons	all	electrons
0–1	71.4	73.5	95.8	97.7	44.8	50.9
1–3	80.9	73.5	97.4	92.7	75.7	74.2
3–5	66.9	69.9	96.2	88.4	73.0	73.4
5–7	55.7	68.5	93.8	88.8	62.2	75.1
>7	28.0	67.0	87.0	89.3	38.5	76.2

Table 5.2: Influence of the cut on the number of clusters (N_{Cls}) in ITS, TPC and TRD. The entries show the amount of rejected ESD tracks.

p_T bin [GeV/c]		0–1	1–3	3–5	5–7	>7
$N_{Cls}(ITS) > 3$	all tracks	27.4	18.7	32.8	44.0	71.7
	electrons	25.8	26.2	29.7	31.1	32.6
$N_{Cls}(ITS) > 4$	all tracks	38.2	28.9	42.3	53.5	75.8
	electrons	39.8	37.9	40.8	42.9	44.7
$N_{Cls}(ITS) > 5$	all tracks	51.6	43.4	51.7	57.9	77.1
	electrons	69.7	66.6	66.5	66.6	67.1
$N_{Cls}(TPC) > 40$	all tracks	4.4	6.5	13.6	17.2	71.4
	electrons	2.1	16.4	22.2	22.4	22.1
$N_{Cls}(TPC) > 100$	all tracks	17.8	20.9	32.5	39.7	59.6
	electrons	10.1	34.4	41.2	40.8	40.5
$N_{Cls}(TPC) > 140$	all tracks	59.2	37.8	38.8	47.3	75.0
	electrons	41.2	42.1	43.6	42.0	41.3
$N_{Cls}(TRD) > 40$	all tracks	52.8	27.1	28.3	38.1	71.4
	electrons	40.4	25.1	25.1	23.0	22.1
$N_{Cls}(TRD) > 85$	all tracks	66.6	38.2	34.7	43.8	75.5
	electrons	54.7	35.3	32.0	29.5	29.5
$N_{Cls}(TRD) > 105$	all tracks	75.6	45.0	40.4	48.5	77.9
	electrons	60.7	42.2	38.8	36.9	35.8

Table 5.3: Influence of the cut on the χ^2/N_{Cls} in ITS, TPC and TRD. The entries show the amount of rejected ESD tracks.

p_T bin [GeV/c]		0–1	1–3	3–5	5–7	>7
$0.1 < \chi^2/N_{Cls}(ITS) < 40$	all tracks	27.5	18.8	33.4	45.8	77.7
	electrons	25.9	26.2	29.8	31.2	32.7
$0.3 < \chi^2/N_{Cls}(ITS) < 20$	all tracks	28.2	19.3	33.9	46.5	79.3
	electrons	26.7	26.6	30.3	31.8	33.3
$0.6 < \chi^2/N_{Cls}(ITS) < 5$	all tracks	35.5	25.1	37.9	49.6	80.8
	electrons	37.8	30.7	32.4	33.5	34.4
$0.1 < \chi^2/N_{Cls}(TPC) < 40$	all tracks	3.4	2.4	3.5	5.4	10.2
	electrons	1.4	7.5	12.2	11.8	11.1
$0.3 < \chi^2/N_{Cls}(TPC) < 20$	all tracks	3.7	3.4	5.2	7.2	13.0
	electrons	1.6	9.0	13.6	13.4	12.5
$0.6 < \chi^2/N_{Cls}(TPC) < 5$	all tracks	5.2	3.9	6.6	11.0	22.7
	electrons	2.0	12.1	17.9	17.4	16.9
$0.1 < \chi^2/N_{Cls}(TRD) < 40$	all tracks	28.9	19.6	33.7	45.2	72.5
	electrons	27.1	28.4	31.7	33.3	34.8
$0.3 < \chi^2/N_{Cls}(TRD) < 20$	all tracks	29.9	21.2	35.8	46.7	73.2
	electrons	28.7	30.9	34.2	35.8	36.9
$0.6 < \chi^2/N_{Cls}(TRD) < 5$	all tracks	37.3	34.4	45.8	54.4	76.3
	electrons	37.7	43.6	43.9	45.2	45.7

Table 5.4: Fraction of *kink* ESD tracks within different p_T bins.

p_T bin [GeV/c]	kink ESD tracks [%]	kink ESD tracks [%] (electrons)
0 – 1	3.4	1.0
1 – 3	9.4	21.2
3 – 5	22.2	26.5
5 – 7	24.0	27.4
7 – 25	22.4	28.9

Apart from these parameters originating from the basic reconstruction another parameter is of importance, the kink index. The algorithm to find kinks was introduced to detect Kaon decays like $K^+ \rightarrow \mu^+ + \nu_\mu$ where only the muon is measured, but since the neutrino carries half of the momentum and is not measured, the whole process appears as a positively charged track with a kink at the point of the Kaon decay. Although this algorithm was designed for these Kaon decays it also finds a lot of kinks for other tracks, which basically leads to a duplication of the corresponding track. Whether a track was reconstructed as a *mother* (decaying particle) or *daughter* (produced particle) is indicated via the kink index. Since for this type of analysis only the primary tracks are of interest and double counting of tracks should be avoided all kink daughter particles are excluded from further analysis.

The above described parameters are of course not independent from each other. For example the number of clusters shows a strong correlation with the status bit for the corresponding detector, in an extreme case, there cannot be a track without a cluster. To give an impression on how different quality parameters influence the reconstruction efficiency, the electron tracks from the data set have been evaluated using three different sets for quality parameters: *tight*, *moderate* and *loose*. Named according to the strength of the applied criteria. Table 5.5 summarizes the implications of the various parameter sets on electron tracks. All three sets required the status bit *refit* to be present for ITS, TPC and TRD. So only the cuts for the number of clusters and the $\chi^2/n_{clusters}$ were varied. Table 5.5 shows the obtained results. The percentage of accepted ESD tracks is almost the same for the *moderate* and *loose* parameter set, it drops significantly for the *tight* parameter set.

One should note that the presented efficiencies are not directly connected to the tracking efficiency. The parameters reflect the quality and special characteristics of the tracks, the requirement to have all refit bits set and a relatively large number of clusters in ITS reduce the amount of ESD tracks to tracks originating from or only a small distance from the primary vertex. Secondary tracks, especially secondary electrons from conversions can only fulfill this requirement if they are produced in the first or second layer of ITS. All other secondary electrons are filtered out by these requirements.

For all further presented studies on the primary and secondary J/ψ detection, the *moderate* cut parameter set is used, additionally the refit bits for ITS, TPC and TRD are required. A detailed study on how the setting of the quality parameters influences the tracking efficiency should be performed as soon as real data used for comparison with the simulations is available.

5.5 Physics cuts

5.5.1 Transverse momentum cut

To give an impression on how a real analysis on J/ψ 's might work, various possibilities to cut on the ESD tracks shall now be discussed. These cuts will then be evaluated according to their implication on the performance of the measurement.

Table 5.5: Efficiency of combined cuts for three different parameter settings. For all settings the refit bits were required to be set. Apart from the quality parameters a cut on p_T of 1 GeV/c was applied to the ESD tracks.

parameter setting		<i>loose</i>	<i>moderate</i>	<i>tight</i>
$n_{cluster}$	ITS	3	4	5
	TPC	40	100	140
	TRD	40	85	105
$\chi^2/n_{cluster}$ ITS, TPC, TRD	min	0.1	0.3	0.6
	max	40	20	5
accepted [%]		56.1	55.8	24.2

The analysis is similar to the analysis applied to the *fast*-simulated data presented in section 4.1. Basically all identified electrons within all tracks of an event are combined with all positrons and the invariant mass of the pair is calculated. The background to the measurement arises from electrons not originating from J/ψ 's, but from other sources. Possible sources of background were already discussed in section 4.3. The dominant sources of background to the J/ψ measurement originate from misidentified pions and electrons from decays of open charm and beauty.

The above described way of analyzing the ESD data offers different ways of applying cuts to the individual tracks. The first possibility was studied in the previous paragraph, when the implications of the track quality parameters were discussed. The remaining cuts, since they reflect more the physics of the J/ψ and its decay products, called *physics* cuts, are the particle identification, the cut on transverse momentum and topological cuts. The particle identification and the cut on transverse momentum are applied to a single particle, while the topological cuts are applied to a combination of an electron with a positron. The cut on the transverse momentum is the most important cut to suppress background particles. The cut, as it was already shown in figure 4.9, also has a strong effect on the signal, especially in the case of the J/ψ . Figure 5.7 shows the signal to background ratio of the J/ψ spectrum as a function of the applied p_T cut. The amount of signal was obtained by the analysis of the data sample 2 (see section 5.3), the background was obtained by the analysis of data sample 4. The signal to background ratio was normalized such that for the same mass interval ($3.0 \text{ GeV}/c^2 < m_{inv} < 3.12 \text{ GeV}/c^2$) with the same cuts the calculated signal to background ratio is equal to 1.22, obtained via the fast simulation framework (see table 4.5).

With increasing p_T -cut the background is more and more suppressed. At the same time the acceptance for the J/ψ decreases until for $p_T(\text{min}) \simeq \frac{1}{2} m_{J/\psi}$ the acceptance approaches zero. As a compromise between the signal to background ratio and the total amount of measured signals, further presented studies will use a p_T cut of 1 GeV/c as it was also used for the presented performance studies, resulting in an acceptance for the J/ψ of 5.8%.

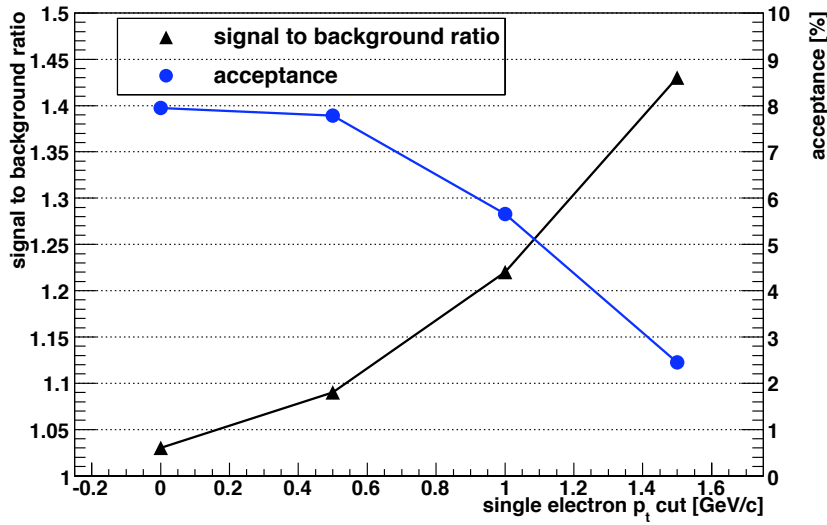


Figure 5.7: The signal to background ratio and the acceptance for the J/ψ as a function of the applied single electron p_T cut.

5.5.2 Particle identification

The scheme for the particle identification was described in [Car04] and shall only shortly be reported here.

Within the Central Barrel the particle identification is performed by the combination of different detectors. The ITS and the TPC distinguish particles via their specific energy loss within the detector material, the TRD uses a combination of the specific energy loss and the emission of transition radiation to distinguish electrons from heavier particles and the TOF detector uses the time of flight of the different particles. There are various possibilities to combine the informations on the particle species by the different detectors.

The scheme chosen for ALICE is based on Bayes's theorem [Bro99] on conditional probabilities. The conditional probability P that a measured signal E in one detector was caused by a particle A of type i can be used to determine the particle species. Following Bayes's theorem it can be calculated by:

$$P(A_i|E) = \frac{c_i \cdot P(E|A_i)}{\sum_{k=1}^n c_k \cdot P(E|A_k)}, \quad (5.1)$$

where c_i is the probability that a particle of type i is present in the detector. $P(E|A_i)$ is given by the detector response function of each individual detector. Both probabilities are in principle momentum dependent.

To determine the first probability c_i the relative particle abundances are needed as input. They are a priori unknown, but there are two proposed ways to obtain them. The first way uses the relative signal height observed in the TOF detector [Car04], the second way starts the particle identification with some educated guess

on c_i and then the relative ratios are tuned by an iterative procedure. The performance of the particle identification does not strongly depend on the chosen a priori probabilities c_i . Figure 5.8 shows a comparison of the electron efficiency ϵ obtained using the true weights obtained from Monte-Carlo information and weights with a 10% enhanced/decreased weight for electrons. Depending on the momentum of the particle the electron efficiency deviates maximal 3% from the ideal case where the Monte-Carlo information was used.

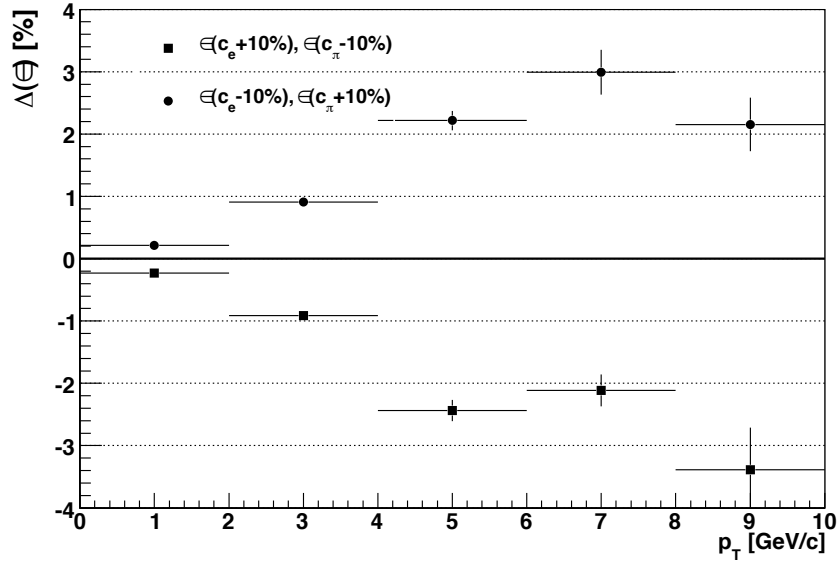


Figure 5.8: Comparison between the electron efficiency ϵ obtained using the Monte-Carlo particle ratios c_i and weights increased/decreased by 10%. The maximum effect on the electron efficiency is around 3%. Of course the relative particle ratios are in principal momentum dependent, which is not taken into account in this study.

The detector response functions $P(E|A_i)$ can be obtained by simulation, comparison to test beam data or directly using real data by creating clean samples of one particle specie using other detectors as a reference.

Under the assumption that the response of N different detectors is independent, one can combine the probabilities given in equation 5.1 to define a global probability:

$$W(A_i|E_1, E_2, \dots, E_N) = \frac{c_i \cdot \prod_{j=1}^N P(E_j|A_i)}{\sum_{k=e,\mu,\pi,\dots} c_k \cdot \prod_{j=1}^N P(E_j|A_k)}. \quad (5.2)$$

Defining the global PID probability this way has some advantages:

- If one of the detectors cannot distinguish between the different species it will give equal probabilities to all species, thus the contribution of this detector just cancels in equation 5.2.
- Since the relative abundances of particles are not known during the reconstruction, the event summary data store only the probabilities determined by the detector response functions. Thus the final decision of the identity of a particle causing the measured track can be postponed to the physics analysis, enabling further cuts on the quality of the particle identification.

To finally attribute a particle species to a measured track one calculates equation 5.2 using relative abundances obtained from one of the above described methods. The particle specie with the highest probability is then attributed to the track. Since the detector response functions did not reflect the realistic performance of the detector within the used aliroot version, conclusions on the performance of the particle identification framework shall not be drawn within these studies. The response functions have been corrected within subsequent releases and currently the performance of the particle identification is subject to extensive studies [Wil08, Ber07]. For all presented studies here the Monte-Carlo information of the particles is used together with the already introduced parameterization 4.6.7 to model the expected performance.

5.5.3 Topological cuts

Opening Angle

The opening angle α between the momentum vectors of the electron and the positron shall be evaluated to see whether it can be used to distinguish between correlated pairs originating from a J/ψ decay and uncorrelated pairs. The distribution of the opening angle is shown in figure 5.9. The distribution is asymmetric with a broad maximum around 60° . Given this broad distribution it is questionable if the opening angle can be used to enhance the signal to background ratio, without cutting too much into the signal distribution.

To show the effect of the cut a similar analysis was performed as in the case of the p_T cut. To obtain the signal to background ratio the data sets 2 and 3 were analyzed using different cuts on the opening angle. The method to calculate the signal to background ratio is equivalent to the method introduced in 5.5.1. Two different cuts on the opening angle were used, the limits are indicated as lines in figure 5.9. The corresponding results for the signal to background ratio are given in table 5.6. The first set of cuts reduces the background in a similar way than the signal (both reduced by 13 %), thus the ratio remains constant, only the rather rigid second cut set reducing the signal by 44 % is able to suppress the background further, such that the signal to background ratio increases slightly. Considering these results it is clear that a cut on the opening angle is not able to significantly increase the performance of the measurement.

Table 5.6: Implication of the cut on the opening angle α on the signal to background ratio (S/B) and the efficiency of J/ψ pairs ϵ calculated relative to the uncut sample.

$\alpha >$	$\alpha <$	S/B	ϵ [%]
0	180	1.22	100
20	140	1.23	87
35	90	1.28	56

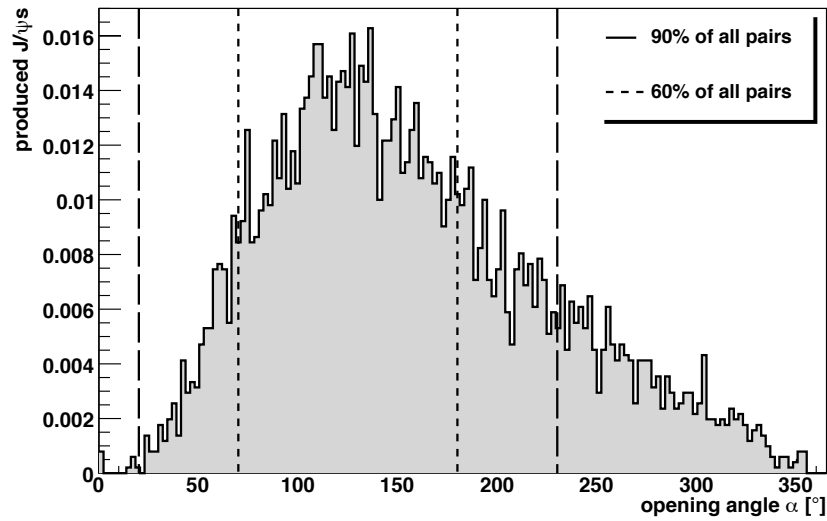


Figure 5.9: Distribution of the opening angle α between the measured momentum vectors of electron and positron at the point of the J/ψ decay. The lines indicate the cuts for 87 % and 56 % J/ψ reconstruction efficiency.

Distance of closest approach

The distance of closest approach dca denotes the closest distance between the electron pair. For electron pairs originating from the decay of a primary J/ψ or any other particle one expects a distribution for the dca which is dominated by the combined impact parameter resolution, given in figure 3.4. The distributions for pure electron pairs and all pairs are shown in figure 5.10. The distribution for the pure pairs has a Gaussian shape with $\sigma = 200 \mu m$. The distribution for all pairs, containing uncorrelated background pairs from misidentified pions and electrons from charm and beauty decays is much broader and reaches out to $dca > 2$ cm.

According to the distribution shown in figure 5.10 a cut on the dca should especially for $dca > 600 \mu m$ reduce the amount of uncorrelated background pairs while the pure signal pairs remain almost unchanged. To test this hypothesis the analysis algorithm has been applied to different data sets with different cuts on the

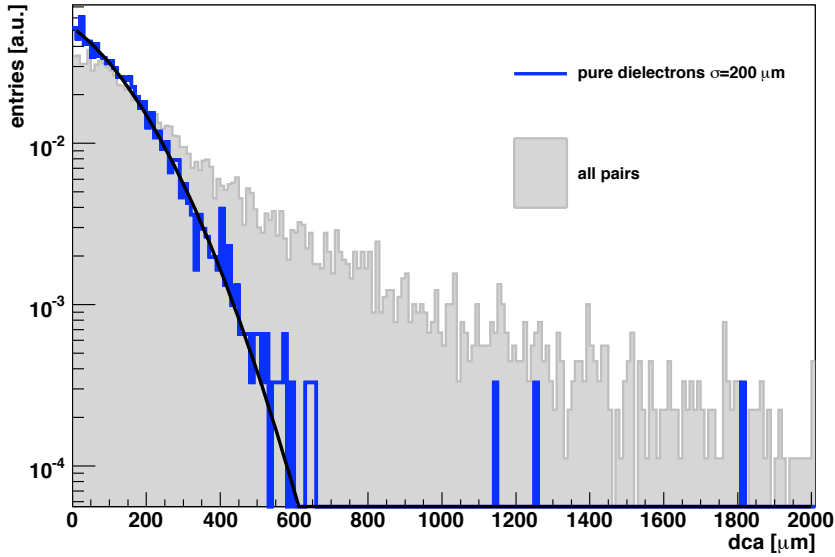


Figure 5.10: The distributions for the distance of closest approach dca for pure electron pairs from secondary J/ψ decays and for all pairs, including uncorrelated background from different sources. The distribution for the pure pairs has Gaussian shape, the $\sigma = 200 \mu m$ reflects the impact parameter resolution for ITS.

dca . The results are summarized in figure 5.11.

The results were normalized to the signal to background ratio given in table 4.5 and the efficiency was normalized to the absolute number of signals recorded with an analysis without dca cut. Only for rather low cuts of less than $200 \mu m$ leads to a significant increase in the signal to background ratio, which in turn goes with a decrease of the signal efficiency.

Although the cut on the dca is not appropriate to significantly increase the performance of the measurement, the implementation is of great importance for the reconstruction of secondary J/ψ decays. Within the algorithm, the dca is used to determine the J/ψ decay vertex. It is assumed, that the point where the two leptons come closest is the J/ψ decay vertex.

5.6 Reconstruction of secondary J/ψ 's

Due to the excellent capabilities to reconstruct decays of charm and beauty mesons, ALICE will also be able to distinguish between primary and secondary J/ψ production. As an extension of the presented analysis, the capabilities to identify secondary J/ψ 's shall be evaluated. Within this analysis the capabilities of the identification via two parameters, r and b (see figure 5.12), shall be evaluated.

The algorithm used to determine the secondary vertex is based on the *AliKF-particle* package [Kis07] which was recently introduced into the *alroot* frame-

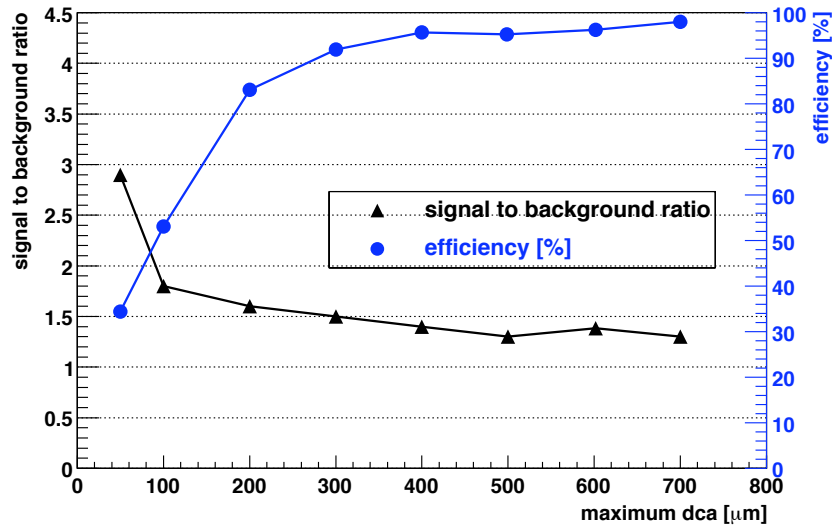


Figure 5.11: The efficiency of the signal and the signal to background ratio as a function of the maximum allowed dca .

work. The package is based on the Kalman filter [Fru00] algorithm, and it uses the same parameterization of the particles as used in the reconstruction. It allows very easy and intuitive combinations of particles and is therefore ideally suited to reconstruct the J/ψ out of two measured leptons and to determine its decay vertex. Since the package is rather new, these studies can also be seen as one of the first complex implementations.

Since these studies are focussed on the analysis of lead-lead collisions the information on the primary vertex is taken from the ESD directly. The primary vertex in lead-lead collisions is determined via linear fits from tracks within the ITS. Since the track density is very high in this environment, the primary vertex coordinates are rather well determined [Car04].

5.6.1 Secondary vertex determination

The secondary vertex is determined via the distance of closest approach (dca) between the electron and the positron. The exact point of the distance of closest approach is determined by the *AliKF*-package, by minimizing the distance between the two reconstructed tracks. To show that the secondary vertex can be determined via this method a comparison of the reconstructed distance r and the simulated distance has been performed. The comparison for pure B -meson events and events with a lead-lead background is shown in figure 5.13. The distribution is asymmetric with a long tail towards positive values, meaning the parameter r is overestimated.

The fact that r is overestimated can be attributed to the electron energy loss which shall be discussed in more detail in section 5.6.3.

In general the comparison shows that one can use the initial assumption that

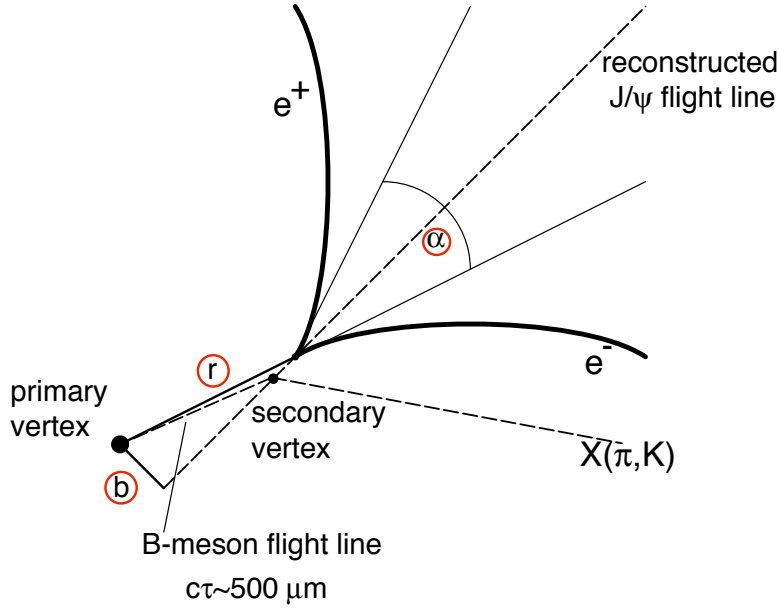


Figure 5.12: Topology of a B -meson decay (e.g. $B^+ \rightarrow J/\psi + K^+$). The distance between the primary and the secondary vertex (r) can be used to distinguish between primary and secondary J/ψ production. In addition the closest distance between the reconstructed J/ψ path and the primary vertex (b) is used to distinguish between correlated signals and uncorrelated background.

the point of the minimal dca can be used to determine the J/ψ decay vertex. For the pure data sample more than 90% of the entries deviate less than $100 \mu m$ from the Monte-Carlo truth, while for the embedded events, due to the degradation of the reconstruction in the high flux environment 70% of the entries are within an interval of $\pm 100 \mu m$.

5.6.2 Primary – secondary J/ψ separation using r and b

As it was briefly described before the basic idea is to determine the vertex of the secondary J/ψ and its distance to the primary vertex (r) by the minimal distance between the electron and the positron. For primary J/ψ 's a distribution of r around zero is expected, defined by the resolution of the detector. For J/ψ 's originating from B -meson decays the distribution is expected to be defined by the life time of $c\tau = 500 \mu m$. In addition, to define criteria to distinguish between them, the relative ratio of primary to secondary J/ψ 's is of importance. According to the calculations presented in section 4.2 $0.02 J/\psi \rightarrow e^+e^-$ per central event are expected. Following the same calculations for the B -meson decay with a production of 8 B -mesons per central event, a branching ratio of $\sigma_{B \rightarrow J/\psi + X} \approx 1\%$ and the

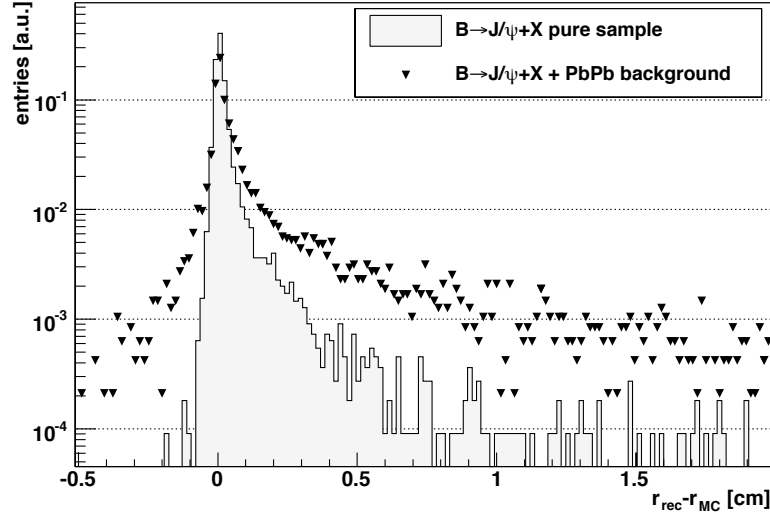


Figure 5.13: The difference between the reconstructed parameter r_{rec} and the true distance between the primary and the J/ψ decay vertex r_{MC} . The gray area shows the distribution for the data sample containing only pure B-decays while the triangles show the distribution for decaying B-mesons embedded in a lead-lead background event. The long tail can be attributed to the energy loss of the electrons (see text for details).

branching ratio of $\sigma_{J/\psi \rightarrow e^+e^-} \approx 6\%$ one expects $4 \cdot 10^{-3}$ J/ψ 's from B-meson decays per event, which is 20%³ of the expected primary J/ψ production. In all further studies this ratio will be used to normalize primary and secondary J/ψ 's relative to each other.

Figure 5.14 shows the distribution of the r parameter for primary and secondary J/ψ 's without background from uncorrelated pairs. Even for large values of r beyond the B-meson lifetime of $500 \mu m$ the contribution from secondary J/ψ 's is only as large as the contribution from primary production. Judging from this distribution r is not well suited to distinguish between primary and secondary J/ψ production.

In addition to the parameter r the parameter b has been evaluated, according to the possibility to enhance the performance of the separation. b denotes the minimal distance between the reconstructed J/ψ flight path and the primary vertex. For primary J/ψ 's one expects only small values of b again dominated by the detector resolution. For secondary J/ψ 's the average values are expected to be larger than zero since due to the decay of $B \rightarrow J/\psi + X$ the direction of the J/ψ and the B-meson are slightly different, thus the J/ψ flight path does not necessarily

³Of course this number depends in principle on the corresponding momentum of the J/ψ . Similar measurements performed by the CDF experiment [Aco04] showed that the relative ratio of primary/secondary J/ψ production ranges from 1% for low p_T to 45% for high p_T .

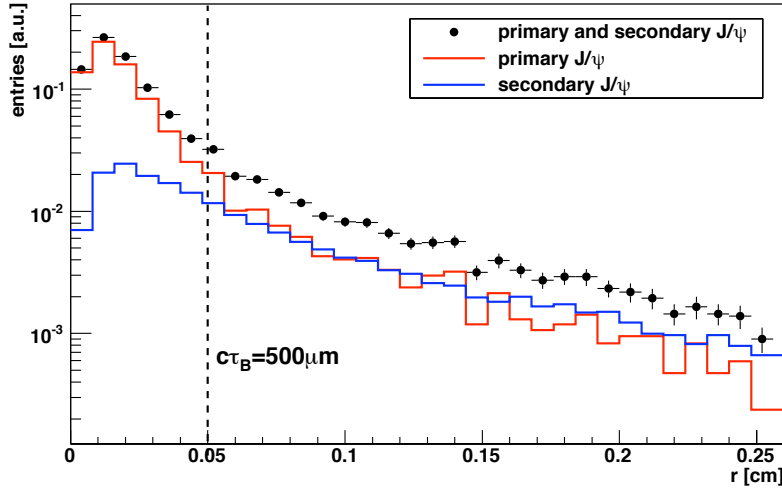


Figure 5.14: Distribution of the r parameter for primary and secondary J/ψ 's. Background from uncorrelated pairs is not included and the invariant mass of the electron pair was not limited to the J/ψ mass. Due to the relative ratio of 1:4 for secondary to primary production, even for large r of more than the lifetime of the B-meson, r is not able to give a reasonable criterion to distinguish between the two different production mechanisms.

point to the primary vertex. Figure 5.15 shows the distribution of b for primary and secondary J/ψ 's. Even worse than in the case of r , b is not suited to distinguish between primary and secondary production. The reason is that due to the decay kinematics the very heavy J/ψ takes most of the momentum of the B-meson and thus flies in almost the same direction, and points back to the primary vertex.

5.6.3 Impact of the electron energy loss

The specific energy loss of the electrons due to bremsstrahlung affects the determination of the precise track and thus also the determination of the location of the vertex. Figure 5.16 shows the correlation between the reconstructed parameter r and the invariant mass of the electron pair. The figures contain only pure events in order not to be disturbed by uncorrelated background pairs. Although the correlation is not very strong, one can safely conclude that large values of r typically coincide with a significantly lower invariant mass. The deviation from the nominal mass can be attributed to an energy loss of one or of both of the electrons due to bremsstrahlung.

If an electron radiates off a sizeable fraction of its energy due to bremsstrahlung the measured bending radius of the track is smaller than the *real*, undisturbed bending radius. If the bending radius and thus also the momentum measurement is disturbed by the energy loss the tracking algorithm reconstructs a track slightly de-

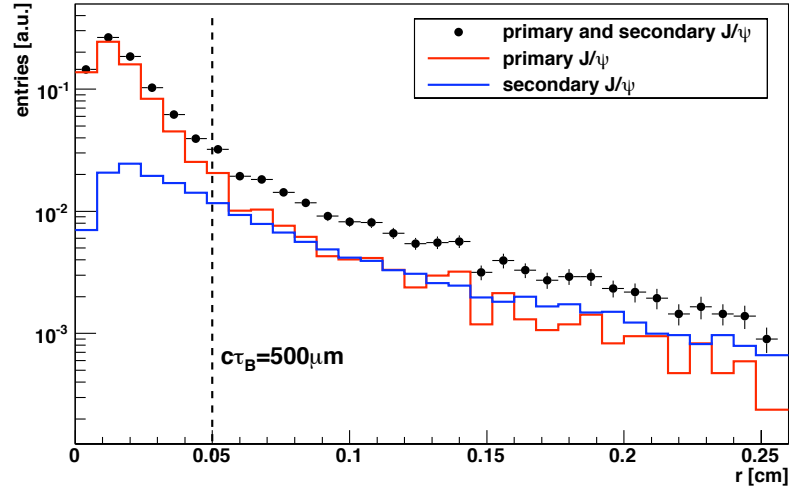


Figure 5.15: The distributions of primary and secondary produced dileptons as a function of the parameter b . It has almost no power to distinguish between primary and secondary production.

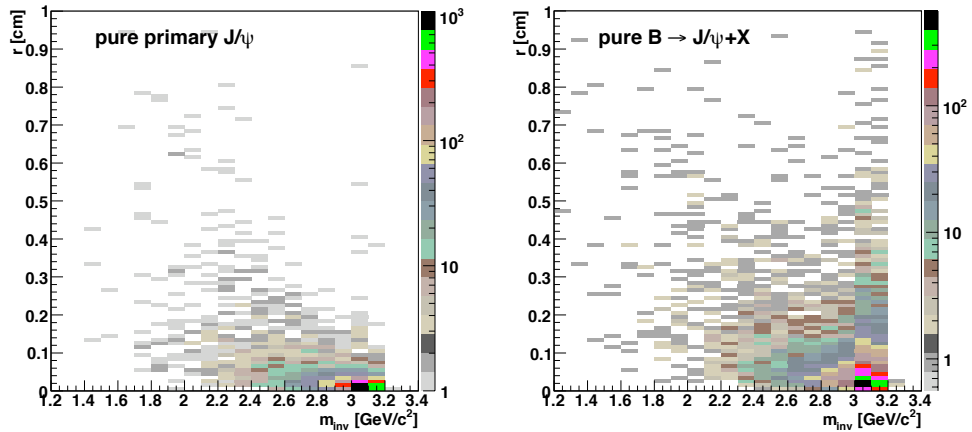


Figure 5.16: The correlation between the invariant mass m_{inv} and r . The figures show pure data sets of primary (left) and secondary (right) J/ψ production. Large values for r coincide with an underestimated invariant mass. Only for the pairs from secondary J/ψ s with the correct invariant mass, large values of r can be observed.

viating from the original path of the particle, thus also the vertex determination is affected. Since due to the orientation of the magnetic field the bending radius is only measured in the xy -plane⁴ an effect should be visible for the measurement of

⁴The ALICE coordinate system [Ali03] is defined as:
x axis perpendicular to the beam, positive direction points towards accelerator center;

the x and y coordinates of a single electron track, while for the z -coordinate one would not expect a correlation with the electron energy loss. Figure 5.17 shows the correlation between the deviation of the nominal and the measured p_T for a single track (Δp_T) and the minimal distance between the reconstructed track and the x -coordinate of the production vertex. Of course this figure is totally dominated by the high statistics around $\Delta p_T \simeq 0$. To quantify a possible effect on the spatial resolution, the histogram was subdivided into eight bins in Δp_T and a Gaussian was fit to the resulting distributions. The obtained fit values for the σ of the Gaussian are shown in figure 5.18, right. The more the reconstructed p_T deviates from the simulated value, the larger the reconstructed track deviates from the original position. As a comparison the same procedure was applied to the z -coordinate of the tracks. Figure 5.18, left shows the results, in contrast to the resolution in x , the z resolution is not affected by the p_T measurement.

It was demonstrated that the energy loss of the electrons not only affects the invariant mass calculation but also the determination of the J/ψ decay vertex. The easiest solution to this problem is to allow only electron pairs corresponding to the correct invariant mass. Figure 5.19 shows the distribution for the parameter r where now only electron pairs contribute with a mass between $3.0 \text{ GeV}/c^2$ and $3.2 \text{ GeV}/c^2$. Since now especially for the primary sample a lot of pairs with large r have been rejected, the secondary produced pairs dominate the total distribution from $r > 500 \mu\text{m}$ on. Nevertheless by the application of this cut one rejects on the order of 35% of the originally produced primary and secondary J/ψ 's.

To avoid this loss of signal of about 1/3 of all signals the tracks would have to be corrected for the energy loss. The standard reconstruction uses the Kalman filter for the reconstruction of the tracks. It allows for Gaussian-like process noise during the track finding, in this way it is possible to take in account deviations from the nominal position due to multiple scattering. In the standard *alroot* tracking scheme all particles are tracked as if they were pions⁵, thus the correction for multiple scattering is tuned for pions. This correction of course is not sufficient for electrons. For electrons, due to the emission of bremsstrahlung an asymmetric process noise distribution is needed, however a priori the Kalman filter is not able to handle asymmetric distributions as process noise. There exist solutions which are able to treat the electron specific energy loss [Kar07], however if and how these solutions can be applied for the ALICE tracking system has to be evaluated in the future.

5.6.4 Impact of the uncorrelated background in lead-lead collisions

In the previous section the possibility to separate primary from secondary J/ψ s was discussed, now the contribution from uncorrelated pairs shall be studied. To study the impact of the uncorrelated background three data samples were used:

y axis perpendicular to the beam, positive direction pointing upwards;

z axis parallel to the mean beam direction, positive direction pointing away from the muon arm.

⁵85% of all charged particles are expected to be pions.

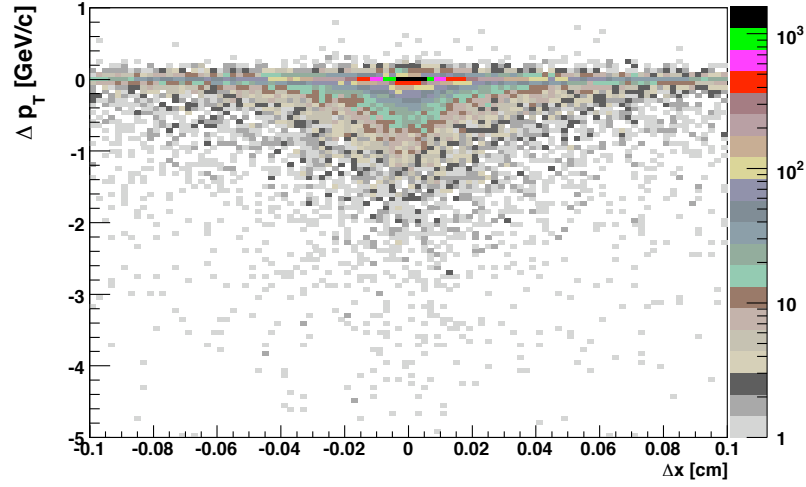


Figure 5.17: The correlation between the p_T resolution (Δp_T) and the spatial resolution Δx .

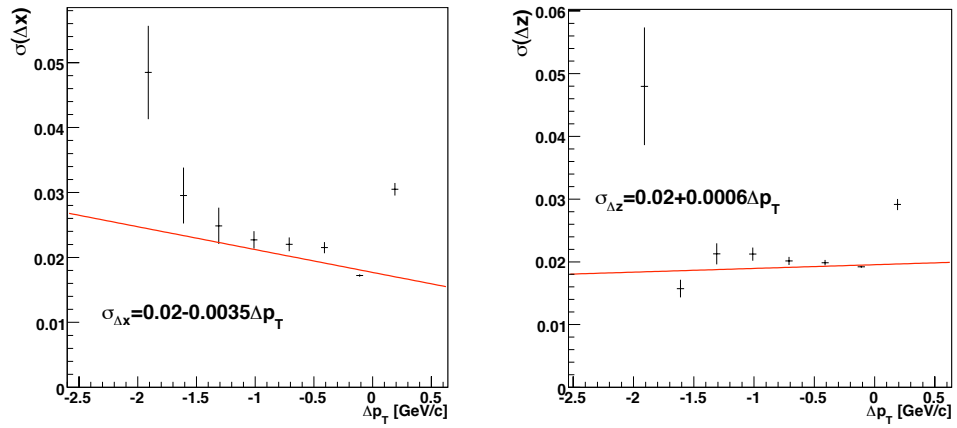


Figure 5.18: The σ of the resolution in x and z as a function of the deviation of the reconstructed from the nominal p_T (Δp_T). While for the x coordinate the spatial uncertainty increases with increasing deviation from the nominal p_T , the uncertainty in z is independent of the accuracy of the p_T measurement.

- $J/\psi \rightarrow e^+e^-$ embedded into a lead-lead background
- $B \rightarrow X + J/\psi \rightarrow e^+e^-$ embedded into a lead-lead background
- a lead-lead background including contributions from charm and beauty mesons.

The data samples consisted of an equal amount of events, in total more than 30.000 events were produced and fully reconstructed. All events were analyzed using the previously defined physics and track quality cuts. In addition to remove pairs con-

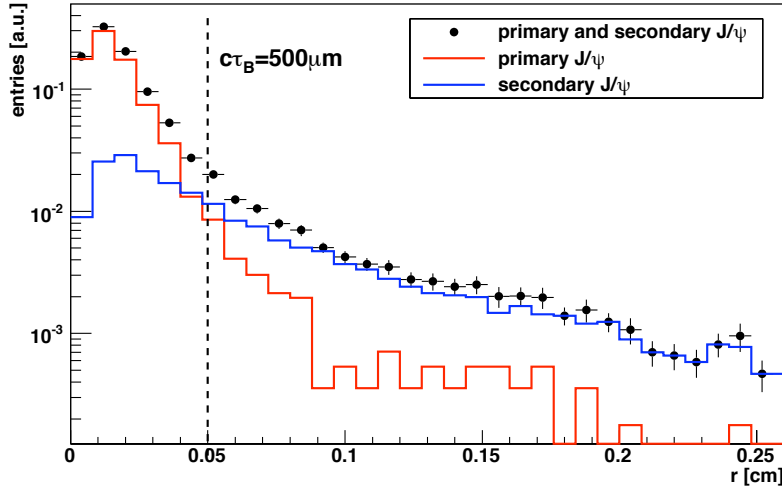


Figure 5.19: The distribution of r using a cut on the invariant mass of $3.0 \text{ GeV}/c^2 < m_{inv} < 3.2 \text{ GeV}/c^2$. From $r > 500 \mu\text{m}$ on the total distribution is dominated by secondary J/ψ production.

taining one or two electrons with a large energy loss, the invariant mass region has been set to $3.0\text{-}3.2 \text{ GeV}/c^2$.

First the *signal* data samples are mixed according to the previously used mixing ratio of 0.2 secondary J/ψ per primary. Then the resulting distribution is combined with the uncorrelated background. The ratio of the two contributions is chosen such that the signal to background ratio in the resulting invariant mass distribution is the same as obtained by the fast simulations presented in section 4.6.

The resulting distributions for r and b , containing contributions from primary and secondary J/ψ production, as well as background from uncorrelated pairs is shown in figure 5.20 and 5.21. For the parameter r there is a clear difference between primary and secondary production. Compared to the distributions for pure J/ψ production, shown in figure 5.14, the background from uncorrelated pairs adds a contribution to the overall distribution comparable to the contribution from secondary J/ψ 's. However since this background originates from uncorrelated pairs one might be able to model it using mixed events and subtract the contribution within an invariant mass analysis.

For the parameter b one can conclude that it has almost no power to distinguish between primary and secondary J/ψ production, in addition one expects a background distribution from uncorrelated pairs, comparable to the one from secondary J/ψ production.

To quantify the contribution from the different sources i the probability $P_i(r)$ was defined as the probability that an electron pair for a given parameter r originates from either primary production, secondary production or from an uncorre-

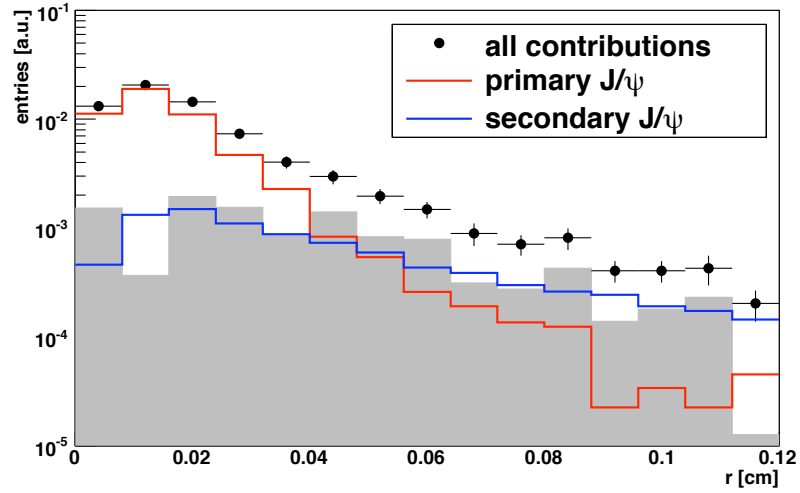


Figure 5.20: The distribution of r for central lead-lead events. The different data samples were mixed such that the expected signal to background ratio of 1.23 ($3.0 \text{ GeV}/c^2 < m_{inv} < 3.12 \text{ GeV}/c^2$, see section 4.6) was achieved. Over the whole range the background from uncorrelated pairs accounts for a significant contribution to the total distribution.

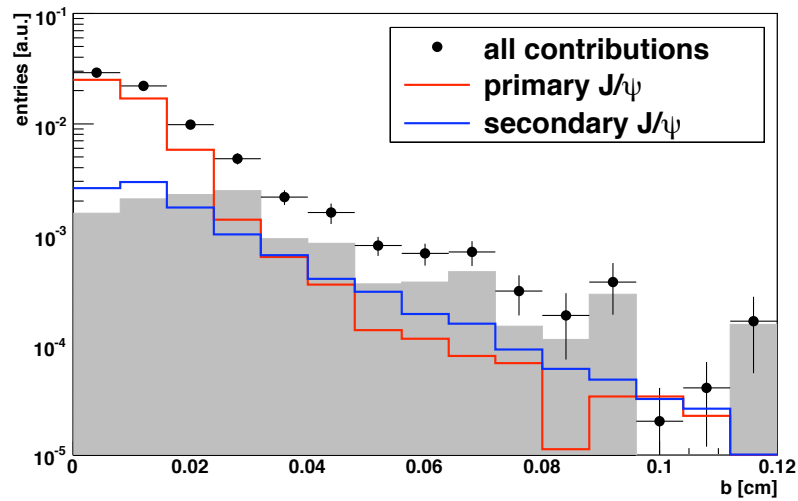


Figure 5.21: The distribution of b for central lead-lead events. The distribution was obtained using the same procedure as for figure 5.20. As already indicated by the studies with background free events, the parameter b has almost no power to distinguish between primary and secondary production and suffers from a background from uncorrelated pairs, that is comparable to the contribution from secondary J/ψ production.

lated pair:

$$P_i(r) = \frac{N_i(r)}{\sum_{j=0}^k N_j} \quad (5.3)$$

The resulting probability distribution for all three sources is shown in figure 5.22. For small distance r the pairs from primary production clearly dominate. From the B -meson lifetime of $c\tau = 500 \mu\text{m}$ on the primary contribution falls below the secondary and uncorrelated one. Only from $r > 0.06 \text{ cm}$ on, the secondary contribution has the highest probability.

However final conclusions shall not be drawn here since the remaining statistics of the uncorrelated sample was rather low and the large contribution in the spectrum can partially be attributed to the used normalization of the different contributions. Further studies with larger data samples should be performed in the future. Or, as a more elegant solution uncorrelated pairs from event mixing should be used to simulate a realistic background of the measurement. As it was pointed out earlier, the used framework was not ready to produce mixed events.

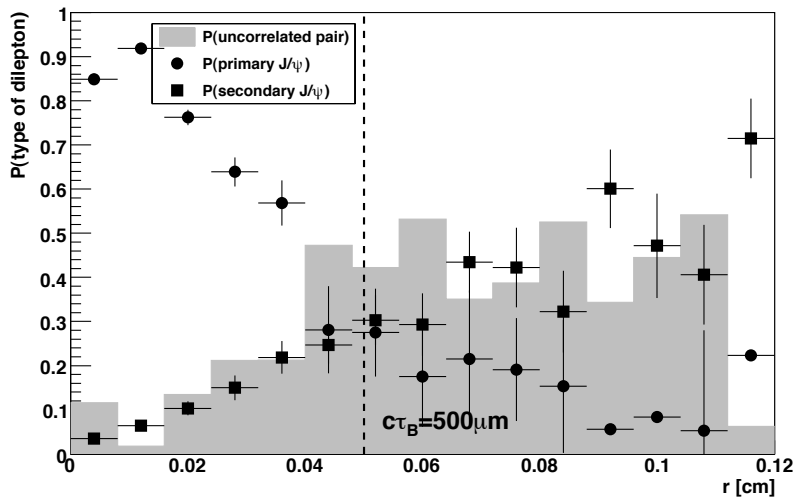


Figure 5.22: The probability $P_i(r)$ that an entry in the invariant mass spectrum with a mass between $3.0 \text{ GeV}/c^2$ and $3.2 \text{ GeV}/c^2$ was caused by a primary or a secondary J/ψ or by an uncorrelated pair. The entries from secondary production dominate for $r > 0.06 \text{ cm}$.

5.7 Conclusion

The aim of the studies presented in this chapter was to develop and test an analysis algorithm within the existing *aliroot* framework. The implementation was done as an *AliAnalysisTask*, the common software platform for analysis within ALICE. Various cuts, concerning the track quality and the physics of the examined process

have been implemented and evaluated with respect to their implications of the efficiency of the analysis. Since the framework still undergoes rapid changes and so far no measured data for comparison is available, most of the studies concentrated on the technical implementation, wherever results on the efficiency of cuts are given, these refer only to the used version of *aliroot v4-04-Release*.

First the possibilities to select tracks according to specific quality criteria were studied. To understand the meaning of the specific parameters the general layout and working principle of the reconstruction software was described. The framework for data storage in *aliroot* offers a large variety of quality parameters to select tracks according to the reliability of the contained information.

Further on the most important cuts concerning the physics have been studied, namely the cut on the transverse momentum and the particle identification. The cut on transverse momentum as it removes all low momentum tracks, significantly increases the signal to background ratio for the J/ψ measurement, however for $p_T > 1$ GeV/c it also reduces the acceptance for the J/ψ by 30%. The framework for particle identification based on a Bayesian approach for the combination of the different detectors is implemented but since the major part, namely the response functions for the various detectors were not correctly implemented, a parameterization in combination with the knowledge on the real particle specie was used for the analysis.

In addition topological cuts were implemented, making use of the excellent vertex and track reconstruction capabilities of the ALICE central barrel. For all topological studies a relatively new package, called *AliKFParticle*, was used. Thus this study represents one of the first complex implementations of this package. For the analysis of primary J/ψ 's the possibility to select electron pairs according to their opening angle and their distance of closest approach have been studied. Both parameters according to these studies do not significantly increase the performance of the measurements.

Although the distance of closest approach is not well suited to increase the performance of the measurement it is of great importance for the detection of the secondary vertex. It was demonstrated that the point where the electron and the positron track come closest is a good approximation for the point of the decay of the b -meson. With this point one is able to determine the distance between the primary and secondary vertex. This distance is the most important parameter to separate primary from secondary J/ψ production. It was shown that in principle the secondary J/ψ production should dominate the distribution of r from approximately one life-time $c\tau = 500$ μm on.

There are two interfering effects to the measurement, the impact of the electron energy loss and the background from uncorrelated pairs. The specific electron energy loss affects the vertex determination since due to the emission of bremsstrahlung the curvature of the track is smaller compared to the undisturbed track, therefor the reconstructed track deviates from the nominal position. Further studies on the possibility to correct for the electron energy loss during the reconstruction should be performed in the future.

With the applied cuts it was not possible to completely suppress the background from uncorrelated pairs expected in central lead lead collisions. The remaining contribution is comparable to the contribution from secondary J/ψ production. However the relatively small statistics in the sample of uncorrelated pairs results in a relatively large uncertainty on the exact shape and size of the distribution of background pairs.

Chapter 6

Summary and outlook

The measurement of quarkonium is since more than 20 years after the original idea still among the hot topics of heavy-ion physics. Although recent measurements showed that the original picture of a total suppression of quarkonium in the quark gluon plasma had to be modified.

There is so far no common theoretical interpretation of the data accumulated by the NA60 and Phenix experiment. The most successful models in describing the data include apart from the suppression a mechanism for quarkonium production in later stages of the collision.

Different models, describing the current experimental status, significantly differ in the predictions for collision energies of 5.5 TeV per nucleon. Thus the expected quarkonium measurements with the ALICE detector will contribute significantly to resolve the theoretical puzzle.

To evaluate the expected performance of the quarkonium measurement under realistic assumptions a fast simulation framework was used to simulate the expected statistics for one ALICE running year. Within this framework the performance of the detector was studied with respect to the efficiency and the resolution. Especially the effects of the electron specific energy loss have been studied.

It has been shown that with its excellent electron identification capabilities of the TRD and the good momentum resolution of the Central Barrel after one year of lead-lead data taking a significant amount of signals for the J/ψ and the Υ family can be expected. The performance of the measurement has been studied with respect to the variation of many input parameters like the underlying multiplicity of the event, the elementary charm and beauty cross section and the performance of the electron identification. It has been demonstrated that within the expected variations of the input parameters the measurement of the quarkonium states is possible.

In addition to the performance studies an ESD-based analysis algorithm has been developed to reconstruct quarkonium in lead-lead collisions. Possible cuts, on the quality of the used tracks as well on the physical quantities have been studied according to their impact of the performance of the analysis.

As an extension the reconstructed electron and positron tracks are used to determine a possible secondary vertex. This vertex reconstruction can be used to separate primary from secondary J/ψ production. In this study there was a special emphasis on the impact of the electron energy loss and the possible impact of uncorrelated lepton pairs, originating from the underlying lead-lead event.

The electron specific energy loss does not only effect the momentum measurement, but seems to have an influence on the determination of the overall tracking parameters and thus also effects the vertex determination. As this result was rather unexpected it should be subject to further studies in the future with a special emphasis on possible ways to recover the electron energy loss.

Appendix A

Kinematic variables in heavy-ion collisions

In this section the definitions of kinematical variables used within this thesis shall be given.

- **Total energy E :**

The total energy E of a particle is defined via:

$$E^2 = m_0^2 + \vec{p}^2 \quad (\text{A.1})$$

m_0 denotes the rest mass of the particle and \vec{p} its three momentum vector.

- **Center of mass energy $\sqrt{s_{NN}}$:**

$\sqrt{s_{AB}}$ is defined as the available energy for particle production in a collision of two nuclei with A, B nucleons. It can be calculated using the total energy E_i and the momentum \vec{p}_i of a particle i .

$$\sqrt{s_{AB}} = \sqrt{(E_A + E_B)^2 - (p_A + p_B)^2} \quad (\text{A.2})$$

s is as the norm of a 4-vector Lorentz-invariant.

- **Transverse momentum p_T :**

The transverse momentum denotes the momentum perpendicular to the beam axis. It is defined as:

$$p_T = \sqrt{p_x^2 + p_y^2} \quad (\text{A.3})$$

with p_x, p_y as the momentum components in x and y direction (beam-axis parallel to z). With θ as the polar angle between the momentum vector and the beam axis p_T can be written as:

$$p_T = p \cdot \sin \theta \quad (\text{A.4})$$

By definition the transverse momentum is Lorentz-invariant under transformations in beam direction.

- **Transverse mass m_T :**

The transverse mass is defined as:

$$m_T = \sqrt{p_T^2 + m^2} \quad (\text{A.5})$$

with m as the rest mass of the particle.

- **Longitudinal momentum p_L :**

The longitudinal momentum denotes the momentum in longitudinal direction, parallel to the beam axis:

$$p_L = p_z \quad (\text{A.6})$$

or analogous to A.4

$$p_L = p \cdot \cos \theta. \quad (\text{A.7})$$

- **Rapidity y :**

The rapidity y is defined as:

$$y = \frac{1}{2} \ln \left(\frac{E + p_z}{E - p_z} \right) \quad (\text{A.8})$$

Since the rapidity contains the total energy, the particle has to be identified. Although the rapidity is not invariant under a Lorentz-transformation, it was defined such that a Lorentz-transformation results in an additive constant. The rapidity is connected with the longitudinal momentum of the particle:

$$p_L = \sinh y \quad (\text{A.9})$$

- **Pseudorapidity η :**

η is defined as:

$$\eta = -\ln \left[\tan \left(\frac{\theta}{2} \right) \right] = \frac{1}{2} \ln \left(\frac{|p| + p_z}{|p| - p_z} \right) \quad (\text{A.10})$$

In contrast to the rapidity it is defined even if the particle type is unknown. The measurement of the polar angle θ is sufficient to calculate the pseudorapidity. For $E \gg m_0$ the pseudorapidity approaches the rapidity $\eta \approx y$. Some useful relations for the pseudorapidity are:

$$|p| = p_T \cosh \eta \quad (\text{A.11})$$

$$p_z = p_T \sinh \eta \quad (\text{A.12})$$

- **Energy density ϵ :**

The energy density ϵ created in heavy-ion collisions can, as it cannot be directly measured, be approximated by various models. Here only the results of the Björken-scenario shall be described. The Björken scenario relates the energy density with the measured central rapidity density $\left(\frac{dN}{dy}\right)_{y=0}$ of the particles.

$$\epsilon_0 = \frac{\langle m_T \rangle}{\tau_0 A} \left(\frac{dN}{dy} \right)_{y=0} \quad (\text{A.13})$$

where A denotes the transverse area of the colliding nuclei, τ_0 the time the particles need to form out of the initial reaction and $\langle m_T \rangle$ denotes the average transverse mass. The formation time τ_0 is usually assumed to be 1 fm/c. Using this approximation the energy density at SPS and RHIC were calculated to be $\epsilon_0(\text{SPS}) \approx 3 \text{ GeV/fm}^3$ and $\epsilon_0(\text{RHIC}) \approx 5 \text{ GeV/fm}^3$.

Appendix B

TRD production in Frankfurt

The ALICE Transition Radiation Detector as described in section 3.3.3 is built in a joined effort of 11 different institutes from four different countries. Table B.1 shows all participating institutes and the corresponding production steps. Other parts, like for example the back panels of the readout chambers are produced by external companies. The construction was started in 2004, the aim is to complete the TRD production until the end of 2008, such that the detector is fully operational for the first heavy-ion run.

During the operation of the LHC only short terms for maintaining the accelerator and the detectors of three month per year are planned. Given the strong entanglement of the various detector parts, these maintenance terms will not be long enough to replace broken parts of the detector after the installation. This puts strong requirements on the quality of the individual detector parts. To guarantee the full functionality over a period of 10-15 years of operation, any part of the detector has to be tested after each production step.

In the following two of the production steps performed at Frankfurt will be described: The production of the readout chambers and the production of the pad planes.

B.1 TRD readout chamber production

In section 3.3.3 and figure 3.7 it was already shown that the TRD consists of 540 chambers organized in 18 super-modules. Each super-module houses 30 readout-chambers (ROC), arranged in 6 layers in radial direction (L0-L5) and five stacks in z-direction. The distribution of the different types of ROC's to the various production sites is shown in table B.2. Since the dimensions of the ROC's increase with the layer, causing different tooling for any layer, most of the sites concentrate on one or two types of chambers. An exclusion is JINR Dubna producing all chambers of type C0 (central stack at midrapidity).

The IKF is responsible to produce 68 ROC's. Compared to the other german sites for ROC production, PI and GSI, the IKF is, in terms of total space as well as

Table B.1: Institutes participating in the TRD project and the corresponding assigned task.

Institute	Assigned task	Period
University of Athens	high voltage system	2004-2008
NIPNE Bucharest	chamber production	2004-2008
GSI Darmstadt	chamber production	2004-2008
IKP, University of Darmstadt	pad plane production	2007-2008
JINR Dubna	chamber production	2004-2008
IKF, Frankfurt University	chamber production	2005-2008
	pad plane production	2004-2007
	electronic integration	2007-2008
Kirchhoff Institute, Heidelberg	front-end electronics	2004-2008
	optical readout interface	2004-2008
PI, University of Heidelberg	front and side profiles	2004-2008
	chamber production	2004-2008
	low voltage system	2006-2008
	cooling system	2006-2008
Fachhochschule Köln	detector control system	2004-2008
IKP, Münster University	radiator production	2004-2008
	super-module integration	2007-2008
	cooling pipes	2007-2008
ZTT, Fachhochschule Worms	communication software	2004-2008

Table B.2: Distribution of the different types of readout-chambers to the five production sites (total amount of pieces to produce excluding spares).

ROC-type	production site	pieces in total
L(0-5)C0	JINR	$5 \times 18 = 90$
L0C1	IKF	68
L0C1	PI	4
L1C1	PI	72
L2C1	NIPNE + JINR	50 + 22
L3C1	NIPNE + GSI	50 + 22
L4C1	GSI	72
L5C1	GSI	72

in terms of available manpower, the smallest production site. One advantage was that the IKF was scheduled to start the production 1 year later than the other sites, thus it was possible to adopt most of the necessary tooling as well as the layout of the production site and schedules for production. In addition, due to the limited space for storage at the IKF it was decided to produce the smallest ROC's, type LOC1 at the IKF.

The layout of the ROC's was described in 3.3.3, the ROC production is described in detail in [Adl05b]. To ensure a similar behavior of all chambers the production manual has to be strictly followed at each production site. Basically the chamber production can be split into five parts:

1. back panel manufacturing
2. frame assembly
3. application of wires
4. chamber performance test
5. final assembly

The back panel consists of a honeycomb structure made of Nomex¹ with carbon fiber sheets on both sides, combining excellent stability with minimal material budget. Onto this back panel the pad plane is glued. The pad plane consists of three different printed circuit boards (PCB), each PCB holds the pads on one side and flat ribbon cables on the other side. The problem is, that the gas amplification of the chamber is very sensitive to the length of the amplification region. For this reason it has to be ensured that the pad plane is flat, with maximum deviations of 20 μm . To guarantee the flatness of the pad plane, the PCB's are soaked onto a especially designed flat vacuum table (see figure B.1, left). Then the back panel is glued to the PCB's, the layer of glue is relatively thick (≈ 0.1 mm) such that any deviation from flatness of the back panel is taken up by the glue and not transferred to the pad plane. After the glueing procedure the PCB's have to be cut on the edges and the connectivity of the flat ribbon cables has to be checked.

The frame of the chamber consists of the radiator, two Wacosit² L-profiles strengthened with aluminum, and two Wacosit front profiles. As the back panel the frame has to be build exactly according to specifications, to prevent deformations of the chamber resulting in gain uniformities. To ensure the exact measures all parts are checked for possible deformations. Then the profiles are fixed to an especially designed table (see figure B.1, right), such that all parts are within their defined position. Then the radiator is glued to the profile, giving the frame stability. The glueing has to be done with care, to ensure the gas tightness of the chamber.

The most delicate part of the chamber construction is the wiring of the chambers. First the cathode wire plane is glued to the frame. The cathode wires are made

¹A fiber polymer with very high strength and low weight.

²A special kind of plastic, providing excellent stability and easy machining.

of beryllium coated with copper with an average diameter of $75\ \mu\text{m}$. The winding is done on the especially designed winding machine. The machine shown in figure B.3 is able to control the wire tension as well as the wire pitch. For the winding two aluminum frames are used, such that two wire planes at a time are produced. The cathode wires are wind with a nominal tension of 120 cN and a wire pitch of 2.5 mm. After the winding process the wires are glued to the frame and soldered to copper strips to ensure connectivity. The anode wire plane consists of gold coated tungsten wires with an average diameter of $20\ \mu\text{m}$. The wire pitch is 5 mm, the tension 40 cN, which is 80% of the breaking tension. To avoid breaking wires, even gentle touches have to be strictly avoided.

The wired frame is then taped to the back panel and a first test is performed. The testing procedure is described in [Kra06]. After the successful test the back panel is glued to the frame and a second final test is performed.

These construction steps and the corresponding tooling had to be distributed between the three available labs at the IKF. The main consideration for the distribution were the requirements on cleanliness. The back panel glueing and the frame assembly do not require a clean environment, they can be cleaned afterwards, thus the two construction steps were placed in one lab. On the contrary the winding of the wires as well as the glueing of the wires requires an almost dust-free and dry environment.

Dust in the chamber can, under high-voltage, lead to the formation of bridges between anode and cathode wires. The dust is attracted by high field gradients. If a piece of dust binds to a wire, a peak is created, causing a high field gradient, leading to a more attractive potential for other dust grains. Like this a growing bridge of dust grains leading from an anode wire to either a cathode wire or the pad plane are formed. These dust bridges can be conductive and thus lead to dark currents, increasing the noise. In a worst case scenario, a wire can break due to a high current caused by a dust bridge. This will result in an unusable chamber.

Another factor that has to be controlled during the production is the humidity of the air. The glue used for the chamber production binds water during hardening. If too much water is bound on the surface of the glue, the surface resistivity decreases, which under high voltage leads to dark current, again leading to an increased noise. For this reason the humidity during the glueing of the wires has to be below 40%, consequently the whole room containing the winding machine and the table to glue the wires is humidity controlled and the air is filtered.

The final glueing as well as cleaning of the wired chamber and repairs, are performed in the third lab, on the 1.5 t stone table. The stone table provides excellent flatness and a low vibration environment (see figure B.2). On top of the table a laminar flow box was installed to provide a dust free environment, important for the cleaning procedure. At this point the humidity is no longer critical, since no direct glueing of the wires happens.

The biggest change that was done in the production in Frankfurt, compared to the production at the PI and GSI was the production schedule. As already described above with one wiring procedure, two planes of wires are produced. Each plane is



Figure B.1: The table for the frame assembly (right) and the vacuum table for the gluing of the back panel (left). The aluminum plates are especially designed and machined with very high precision of a maximum deviation of less than 0.1 mm.

fixed to one half-frame, such that the frames can be separated without breaking the wires. At PI and GSI one half frame is directly used and the wires are glued to a chamber, the second frame is stored for the next chamber. Then the next wiring with the anode wires is performed, again two plains are produced, one is immediately used, the other one stored. This production schedule, taking into account all additional production steps results in one chamber per production cycle. At least three of the rather large and heavy aluminum half-frames have to be handled. Since the wired frames should not be exposed to a dusty environment, the storage room has to be as clean as the room for winding. At GSI and PI, the frames are directly stored within the rather large room containing the winding machine. At IKF the room containing the winding machine is too small to securely store wired frames. For this reason the schedule was changed from a one chamber per cycle to a two chamber per cycle schedule. Instead of storing the large frames, the much smaller chamber are stored within an especially designed dust-free box. Both wire planes produced within one winding are directly glued to two chambers. One chamber is stored and after the winding, the anode plane is glued to the other chamber. Then the previously stored chamber is equipped with the anode plane. In this schedule only two frames are needed, which in addition can be left on the winding machine for most of the time.

On average, to meet the overall TRD production schedule, 0.75 chambers per



Figure B.2: The extreme precise and vibration-less stone table. The laminar flow box on top of it provides an almost dust free air flow. The table is used for the final assembly of the chambers and, due to the small vibrations, for repairs.

week have to be produced. A rate which could be reached in 2005 and 2006, such that no major delays have been accumulated.



Figure B.3: The winding machine with the wire tension meter (blue) and a large aluminum frame. On the ceiling a special lifting device for the heavy aluminum frames (~ 100 kg) was mounted.

B.2 TRD pad plane production

The second major TRD production task performed at the IKF was the soldering of the pad planes. This task already started at the end of 2003. Table B.3 summarizes the different types of PCB's that have to be produced. In total for the complete TRD 1512 PCB's are needed (plus additional 10% spares). In total about 70.000 cables have to be soldered. Between 2004 and the end of 2006 more than 1000

Table B.3: Different types of PCB's, the amount of pieces to produce and the number of cables that have to be soldered to the PCB's (spare PCB's are not taken into account).

type of chamber	PCB	number of PCB's	cables per PCB
(L0-L5)C0	type 1	$6 \times 18 = 108$	48
	type 2	$6 \times 18 = 108$	48
(L0-L5)C1	type 1	$24 \times 18 = 432$	48
	type 2	$24 \times 18 = 432$	32
	type 3	$24 \times 18 = 432$	48

PCB's, representing 2/3 of the total production, were produced at the IKF. At the beginning of 2007 another major task was started at the IKF, the integration of the readout electronics. Due to this new task the PCB production was moved to the University of Darmstadt.

Soldering the flat ribbon cables directly to the PCB is a rather unusual design. Industrial designs use connectors soldered in reflow processes. There is one major reason why this design is not used for the TRD: the constraint to put as less material into the way of the particles as possible. This constraint has various implications: First, the connectors themselves add non-negligible additional material to the detector. Second the PCB's are glued to the back panel. The cutouts for the cables due to stability reasons have to be as small as possible, connectors would require significantly larger cutouts. Third reason is that the PCB's are on the one hand rather large (largest PCB: 55×121 cm), on the other hand due to the constraint on radiation length very thin (0.25 mm). There are only few reflow-soldering machines available for PCB's of that size. Due to the low thickness there is a rather high probability that the PCB's, due to the exposure to high temperatures, start to warp within a reflow-oven. To avoid warping it was decided to use flat ribbon cables, soldered with a special dedicated soldering machine, enabling to solder all fibers of the flat ribbon cable at a time, without applying too much heat.

The whole production process consists of five steps:

1. Entrance control of the PCB's
2. Application of solder to the PCB's
3. Positioning of the flat ribbon cables
4. Soldering
5. Connectivity test

The entrance control ensures that all PCB's are cut to specifications and undamaged. Each PCB is marked by a unique serial number and the side of the pads

is covered with a foil to prevent scratches on the pads. For most of the PCB's this control was performed at the PI in Heidelberg.

The application of the solder to the footprints on the cable side of the PCB, is the most delicate and time consuming part of the production. The amount of solder has to be adjusted such, that cold joints are excluded, at the same time short-circuits, caused by too much solder, have to be avoided as well.

Applying the flat ribbon cables is another time consuming step. Due to the, compared to industrial standards, low quantities, the application had to be done by hand. The cables are fixed to the PCB by a small adhesive strip. The correct place is indicated by little marks printed on the PCB. Displaced cables can lead to short-circuits between pads or in a worst case might break when they are bent upwards during the insertion into the back panel.

After all cables are in place they are soldered using a special soldering machine (see figure B.4), providing exact control over the heating temperature and the soldering time. To prevent pollution of the soldering iron with solder, the fibers of the flat ribbon cables are covered by a capton foil strip.



Figure B.4: The solder machine used for soldering the flat ribbon cables to the PCB. The correct position of the soldering iron with respect to the cables is ensured by latches.

The last step of the production chain is to test the connectivity of the cables. Since a test stand contacting each individual pad would be too complex to build, a test system measuring the capacity has been developed [Leh04]. The idea is that each cable connected to a pad, has a certain capacity. The capacity of each pad is measured. A dedicated software evaluates the individual capacities, and calculates the mean value. If one of the pads is not connected to the cable, its capacity is significantly lower than the mean of all pads. If a short circuit between two or more

pads is present, the capacity of connected pads adds up, resulting in a significant larger capacity. In addition the capacity of shorted pads is exactly the same for both pads, while the capacity for individual pads differs slightly. These criteria are used to detect possible errors. One disadvantage of this measurement is that the measured capacities are very small, on the order of a few \sim nF. These small capacities are very sensitive to the material beneath the pads and to the distance of the pads to the material. To ensure equal conditions a large aluminum plate is used with a 1 mm plastic sheet on top. The PCB's are put on the plastic sheet, such that the pads and the aluminum plate form a plate capacitor. To ensure the flatness and parallelism of the PCB with respect to the aluminum plate, weight is applied on the PCB during the measurement.

The fabrication of each individual PCB was documented. Errors detected during the test were documented and used to optimize the fabrication process. Possible errors were unconnected pads and shorted pads. Each type of error could again be subdivided into errors caused by the soldering process and errors due to the PCB production. The errors due to the PCB production dominantly happened at the etching of the PCB, most of these errors could be repaired. The rate of these types of errors was 8% compared to the errors due to the soldering.

Errors due to the soldering were found to be highly correlated with the amount of solder. As already discussed, too much solder leads to short circuits while too little solder can cause cold joints. Especially cold joints can lead to serious damage in the complete chamber later on. If a pad has no electric connection to the outside, it is floating. Due to the free charges in the gas, the pad charges up, causing distortions of the amplification field. At some point the charge on the pad might cause a spark to the neighboring pads. The sudden current may damage the readout electronics connected to this pad, in a worst case an avalanche is created, destroying large sectors of a chamber. To avoid such avalanches the connectivity of the pads has to be ensured, for this reason the amount of solder is chosen a bit higher than necessary. The disadvantage is that doing so, the probability to create a short circuit between neighboring pads is increased. Consequently among the detected errors more than 90% were short circuits and only a small fraction could be attributed to badly or not soldered pads. In general the average error rate per PCB was 1.3 during the main production phase in 2005.

Apart from the amount of errors the total time needed for the whole process is an important factor. Most of the work was done by student and technical assistants. Thus the overall time was directly related to cost. In addition, since the IKF was the only supplier for all five chamber production site, it had to be assured that all sites could be served with PCB's in time. Figure B.5 shows the amount of PCB's produced per month and the average error rate. Only the data for the years 2004 and 2005 are given since from autumn 2005 on the ROC production started and the working assistants were shared. Thus a clear distinction with respect to the deployed man-hours cannot be made. The average production rate was 23.7 PCB's per month in 2004 and 48.5 PCB's per month in 2005, the average time needed to produce one PCB was 8.6 hours in 2004 and 3.8 hours in 2005.

There are several reasons why the production ran more efficient in 2005 compared to 2004. The first and most obvious reason is that the whole production started in 2004, so it took some time until all assistants were properly trained. Also the different processes had to be optimized. The test system was installed in May 2004, it enabled direct checks of the performed work and the test results could be used to further optimize the production process. Another huge increase in performance happened between the end of 2004 and the beginning of 2005. At that time the production, as well as the whole institute moved from the old building (Frankfurt Rebstock) to a new building (Campus Riedberg), offering more space for the production and a much more convenient working environment. The space was used to double the places for the solder application and another dedicated table for the placing of the cables was installed. In addition more racks for the temporary storage of the PCB's between the production steps could be installed, enabling a more structured process.

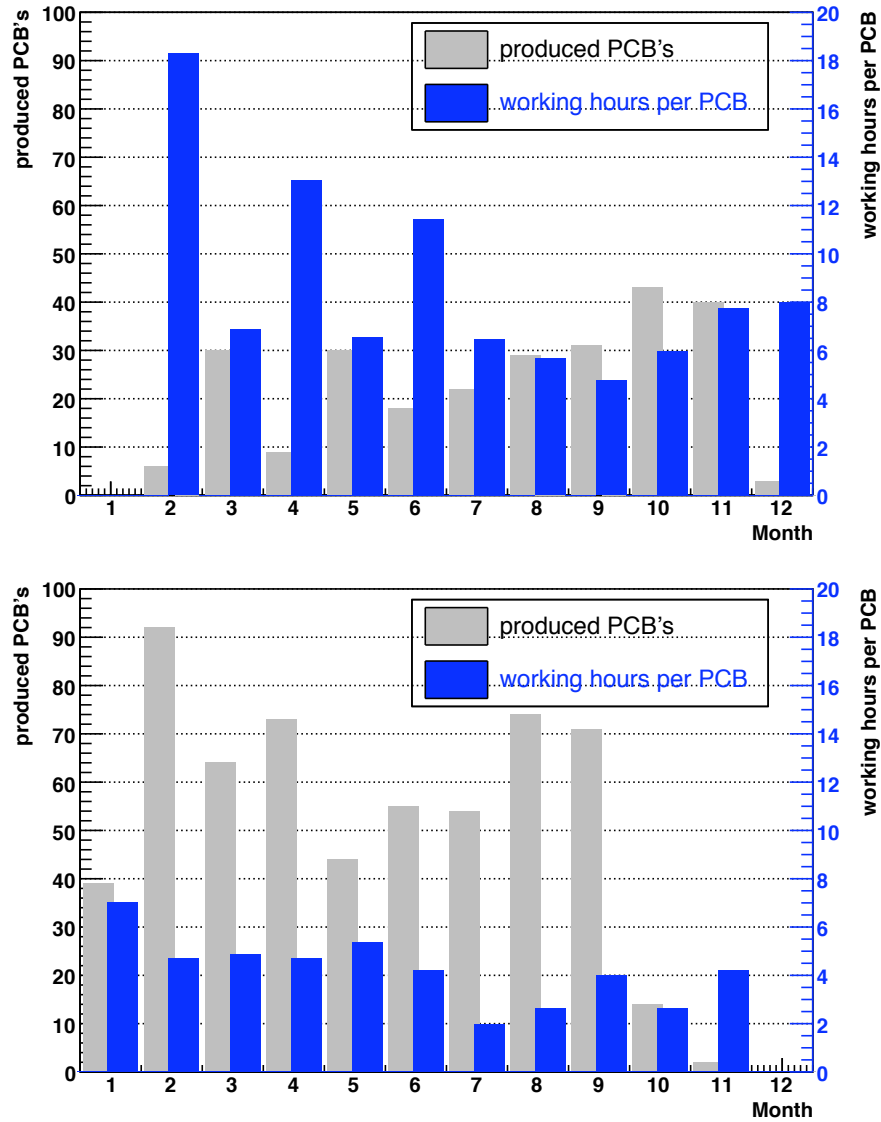


Figure B.5: TRD pad plane production at the IKF in 2004 (top) and 2005 (bottom) showing the total amount of production per month, and the man-working-hours needed per peace.

Bibliography

- [Abe88] F. Abe *et al.* [CDF Collaboration],
“Transverse momentum distributions of charged particles produced in $p\bar{p}$ interactions at $\sqrt{s} = 630$ GeV and 1800 GeV,”
Phys. Rev. Lett. **61** (1988) 1819.
- [Abe95] F. Abe *et al.* [CDF Collaboration],
“Identification of top quarks at CDF using kinematic variables,”
Phys. Rev. D **52**, 2605 (1995).
- [Abe97a] F. Abe *et al.* [CDF Collaboration],
“ J/ψ and $\psi(2S)$ production in $p\bar{p}$ collisions at $\sqrt{s} = 1.8$ TeV,”
Phys. Rev. Lett. **79** (1997) 572.
- [Abe97b] F. Abe *et al.* [CDF Collaboration],
“Production of J/ψ mesons from χ_c meson decays in $p\bar{p}$ collisions at $\sqrt{s} = 1.8$ TeV,”
Phys. Rev. Lett. **79** (1997) 578.
- [Abr91] M. Abreu, and C Baglin, and A Baldit,
“Proposal study of muon pairs and vector mesons produced in high energy Pb-Pb interactions”,
"CERN-SPSLC-91-55. SPSLC-P-265-Rev-", (1991).
- [Abr02] M. C. Abreu *et al.* [NA50 Collaboration],
“Scaling of charged particle multiplicity in Pb Pb collisions at SPS energies,”
Phys. Lett. B **530** (2002) 43.
- [Aco01] D. Acosta *et al.* [CDF Collaboration],
“Upsilon production and polarization in $p\bar{p}$ collisions at $\sqrt{s} = 1.8$ -TeV,”
Phys. Rev. Lett. **88** (2002) 161802.
- [Aco04] D. E. Acosta *et al.* [CDF Collaboration],
“Measurement of the J/ψ meson and b -hadron production cross sections in $p\bar{p}$ collisions at $\sqrt{s} = 1960$ GeV,”
Phys. Rev. D **71** (2005) 032001, [arXiv:hep-ex/0412071].

- [Acc04] A. Accardi *et al.*,
“Hard probes in heavy ion collisions at the LHC: PDFs, shadowing and p A collisions,”
arXiv:hep-ph/0308248.
- [Ada06a] A. Adare *et al.* [PHENIX Collaboration],
“J/psi production vs transverse momentum and rapidity in p + p collisions at $s^{*(1/2)} = 200\text{-GeV}$,”
Phys. Rev. Lett. **98** (2007) 232002 [arXiv:hep-ex/0611020].
- [Ada06b] A. Adare *et al.* [PHENIX Collaboration],
“J/psi production vs centrality, transverse momentum, and rapidity in Au + Au collisions at $s(\text{NN})^{*(1/2)} = 200\text{-GeV}$,”
Phys. Rev. Lett. **98** (2007) 232301 [arXiv:nucl-ex/0611020].
- [Adc01] K. Adcox *et al.* [PHENIX Collaboration],
“Suppression of hadrons with large transverse momentum in central Au + Au collisions at $s^{*(1/2)}(\text{N N}) = 130\text{-GeV}$,”
Phys. Rev. Lett. **88** (2002) 022301 [arXiv:nucl-ex/0109003].
- [Adc03] K. Adcox *et al.* [PHENIX Collaboration],
“PHENIX detector overview,”
Nucl. Instrum. Meth. A **499** (2003) 469.
- [Adl02] C. Adler *et al.* [STAR Collaboration],
“Centrality dependence of high p(T) hadron suppression in Au + Au collisions at $s(\text{NN})^{*(1/2)} = 130\text{-GeV}$,”
Phys. Rev. Lett. **89** (2002) 202301 [arXiv:nucl-ex/0206011].
- [Adl03] S. S. Adler *et al.* [PHENIX Collaboration],
“Absence of suppression in particle production at large transverse momentum in $s(\text{NN})^{*(1/2)} = 200\text{-GeV}$ d + Au collisions,”
Phys. Rev. Lett. **91** (2003) 072303 [arXiv:nucl-ex/0306021].
- [Adl03a] S. S. Adler *et al.* [PHENIX Collaboration],
“J/psi production in Au Au collisions at $s(\text{NN})^{*(1/2)} = 200\text{-GeV}$ at the Relativistic Heavy Ion Collider,”
Phys. Rev. C **69** (2004) 014901 [arXiv:nucl-ex/0305030].
- [Adl03b] S. S. Adler *et al.* [PHENIX Collaboration],
“J/psi production from proton proton collisions at $s^{*(1/2)} = 200\text{-GeV}$,”
Phys. Rev. Lett. **92** (2004) 051802 [arXiv:hep-ex/0307019].
- [Adl05a] S. S. Adler *et al.* [PHENIX Collaboration],
“J/psi production and nuclear effects for d + Au and p + p collisions at $s(\text{NN})^{*(1/2)} = 200\text{-GeV}$,”
Phys. Rev. Lett. **96** (2006) 012304 [arXiv:nucl-ex/0507032].

- [Adl05b] C. Adler, [ALICE Collaboration],
“TRD Chamber Construction Manual”,
<http://www.physi.uni-heidelberg.de/~adler/TRD/ConstructionManual/TRD-CCM.pdf>
- [Aff00] A. A. Affolder *et al.* [CDF Collaboration],
“Measurement of J/ψ and $\psi(2S)$ polarization in $p\bar{p}$ collisions at $\sqrt{s} = 1.8$ TeV,”
Phys. Rev. Lett. **85** (2000) 2886 [arXiv:hep-ex/0004027].
- [Ago02] S. Agostinelli *et al.* [GEANT4 Collaboration], “GEANT4: A simulation toolkit,”
Nucl. Instrum. Meth. A **506** (2003) 250.
- [Ale04] B. Alessandro *et al.* [NA50 Collaboration],
“A new measurement of J/ψ suppression in Pb - Pb collisions at 158-GeV per nucleon,”
Eur. Phys. J. C **39** (2005) 335 [arXiv:hep-ex/0412036].
- [Ale05] B. Alessandro *et al.* [NA50 Collaboration],
Eur. Phys. J. C **39** (2005) 335.
- [Ale06a] B. Alessandro *et al.* [NA50 Collaboration],
“ ψ production in Pb - Pb collisions at 158-GeV/nucleon,”
Eur. Phys. J. C **49** (2007) 559 [arXiv:nucl-ex/0612013].
- [Ale06b] B. Alessandro *et al.* [ALICE Collaboration],
“ALICE: Physics performance report, volume II,”
J. Phys. G **32** (2006) 1295.
- [Ali03] L. Betev, P. Chochula *et al.*,
“Definition of the ALICE Coordinate System and Basic Rules for Sub-detector Components Numbering”,
ALICE-INT-2003-038
- [Ale06c] B. Alessandro *et al.* [ALICE Collaboration],
“ALICE: Physics performance report, volume II,”
Chapter 6.6, J. Phys. G **32** (2006) 1295.
- [Ale06d] B. Alessandro *et al.* [ALICE Collaboration],
“ALICE: Physics performance report, volume II,”
Chapter 6.7, J. Phys. G **32** (2006) 1295.
- [Ali07] <http://aliweb.cern.ch/offline/>
- [Ali01] [Alice Collaboration],
“ALICE Transition Radiation Detector, Technical Design Report”,
CERN/LHCC 2001-021.

- [Ali99] [ALICE Collaboration],
“ALICE technical design report of the dimuon forward spectrometer”,
CERN-LHCC-99-22
- [ALICE Collaboration],
“ALICE technical design report of the inner tracking system (ITS)”,
CERN-LHCC-99-12
- [ALICE Collaboration],
“ALICE technical design report of the zero degree calorimeter (ZDC)”,
CERN-LHCC-99-05
- [ALICE Collaboration],
“ALICE technical design report of the photon spectrometer (PHOS)”,
CERN-LHCC-99-04
- [ALICE Collaboration],
“ALICE: Addendum to the technical design report of the Photon Multiplicity
Detector (PMD)”,
CERN-LHCC-2003-038
<https://edms.cern.ch/document/575585/1>
- [ALICE Collaboration],
“ALICE technical design report on forward detectors: FMD, T0 and V0”,
CERN-LHCC-2004-025;
<https://edms.cern.ch/document/498253/1>
- [Ali05] [ALICE Collaboration],
“ALICE technical design report of the computing”,
CERN-LHCC-2005-018
[http://aliceinfo.cern.ch/Collaboration/Documents/
TDR/Computing.html](http://aliceinfo.cern.ch/Collaboration/Documents/TDR/Computing.html)
- [Ali00] [ALICE Collaboration],
“ALICE technical design report of the time of flight system (TOF)”,
CERN-LHCC-2000-012; [https://edms.cern.ch/document/
460192/1](https://edms.cern.ch/document/460192/1)
- [Ali05] [ALICE Collaboration],
“ALICE technical design report of the Trigger, High Level Trigger, Control
System”,
ALICE-DOC-2004-001
<https://edms.cern.ch/document/456354/1%20>
- [All03] C. R. Allton, S. Ejiri, S. J. Hands, O. Kaczmarek, F. Karsch, E. Laermann
and C. Schmidt,
“The equation of state for two flavor QCD at non-zero chemical potential,”
Phys. Rev. D **68** (2003) 014507 [arXiv:hep-lat/0305007].

- [Ame94] N. S. Amelin, H. Stoecker, W. Greiner, N. Armesto, M. A. Braun and C. Pajares,
“Monte Carlo model for multiparticle production at ultrarelativistic energies,”
Phys. Rev. C **52** (1995) 362.
- [Ame01] N. S. Amelin, N. Armesto, C. Pajares and D. Sousa,
“Monte Carlo model for nuclear collisions from SPS to LHC energies,”
Eur. Phys. J. C **22** (2001) 149 [arXiv:hep-ph/0103060].
- [Amu95] J. F. Amundson, O. J. P. Eboli, E. M. Gregores and F. Halzen,
“Colorless States in Perturbative QCD: Charmonium and Rapidity Gaps,”
Phys. Lett. B **372** (1996) 127 [arXiv:hep-ph/9512248].
- [Amu96] J. F. Amundson, O. J. P. Eboli, E. M. Gregores and F. Halzen,
“Quantitative tests of color evaporation: Charmonium production,”
Phys. Lett. B **390** (1997) 323 [arXiv:hep-ph/9605295].
- [And03] A. Andronic, P. Braun-Munzinger, K. Redlich and J. Stachel,
“Statistical hadronization of charm in heavy-ion collisions at SPS, RHIC and LHC,”
Phys. Lett. B **571** (2003) 36 [arXiv:nucl-th/0303036].
- [And04] A. Andronic [ALICE TRD Collaboration],
“Electron identification performance with ALICE TRD prototypes,”
Nucl. Instrum. Meth. A **522** (2004) 40 [arXiv:physics/0402131].
- [And06] A. Andronic, P. Braun-Munzinger, K. Redlich and J. Stachel,
“Statistical hadronization of heavy quarks in ultra-relativistic nucleus nucleus collisions,”
Nucl. Phys. A **789** (2007) 334 [arXiv:nucl-th/0611023].
- [And07] A. Andronic, P. Braun-Munzinger, K. Redlich and J. Stachel,
“Evidence for charmonium generation at the phase boundary in ultra-relativistic nuclear collisions,”
arXiv:nucl-th/0701079.
- [And07a] A. Andronic, private communication.
- [Ant06] D. Antonczyk *et al.* [ALICE TPC Collaboration],
“Performance studies with an ALICE TPC prototype,”
Nucl. Instrum. Meth. A **565** (2006) 551.
- [Ang06] V. Angelov [ALICE TRD Collaboration],
“Design and performance of the ALICE TRD front-end electronics,”
Nucl. Instrum. Meth. A **563** (2006) 317.

- [Arm94] N. Armesto, M. A. Braun, E. G. Ferreira and C. Pajares,
“Strangeness Enhancement And String Fusion In Nucleus-Nucleus Collisions,”
Phys. Lett. B **344** (1995) 301.
- [Arm00] N. Armesto and C. Pajares,
“Central rapidity densities of charged particles at RHIC and LHC,”
Int. J. Mod. Phys. A **15** (2000) 2019 [arXiv:hep-ph/0002163].
- [Arm07] R. Arnaldi *et al.* [NA60 Collaboration R Arnaldi],
“J/psi suppression in In In collisions at 158-GeV/nucleon,”
Nucl. Phys. A **783** (2007) 261 [arXiv:nucl-ex/0701033].
- [Arn83] G. Arnison *et al.* [UA1 Collaboration],
“Experimental observation of isolated large transverse energy electrons with associated missing energy at $s^{**}(1/2) = 540\text{-GeV}$,”
Phys. Lett. B **122** (1983) 103.
- [Asa04] M. Asakawa, T. Hatsuda,
“J/Ψ and η_c in the Deconfined Plasma from Lattice QCD”,
Phys. Rev. C **92** (2004) 012001
- [Atl07] <http://atlas.web.cern.ch/Atlas/index.html>
<http://atlasexperiment.org/>
- [Aub02] B. Aubert *et al.* [BABAR Collaboration],
“Measurement of the CP-violating asymmetry amplitude $\sin 2\beta$,”
Phys. Rev. Lett. **89** (2002) 201802 [arXiv:hep-ex/0207042].
- [Aub07] B. Aubert *et al.* [BABAR Collaboration],
“Evidence for D0 - anti-D0 mixing,”
Phys. Rev. Lett. **98** (2007) 211802 [arXiv:hep-ex/0703020].
- [Aub74] J. J. Aubert *et al.* [E598 Collaboration],
“Experimental Observation Of A Heavy Particle J,”
Phys. Rev. Lett. **33** (1974) 1404.
- [Aug74] J. E. Augustin *et al.* [SLAC-SP-017 Collaboration],
“Discovery Of A Narrow Resonance In E+ E- Annihilation,”
Phys. Rev. Lett. **33** (1974) 1406.
- [Bag90] C. Baglin *et al.* [NA38 Collaboration],
“THE PRODUCTION OF J / PSI IN 200-GeV/NUCLEON OXYGEN URANIUM INTERACTIONS,”
Phys. Lett. B **220** (1989) 471.
- [Bag91] C. Baglin *et al.* [NA38 Collaboration],
“Study of J / psi production in p U, O U and S U interactions at 200-GeV per

- nucleon,”
Phys. Lett. B **255** (1991) 459.
- [Ban83] M. Banner *et al.* [UA2 Collaboration],
“Observation of single isolated electrons of high transverse momentum in events with missing transverse energy at the CERN anti-p p collider,”
Phys. Lett. B **122** (1983) 476.
- [Bal06] R. Bailhache and C. Lippmann [ALICE TRD Collaboration],
“New test beam results with prototypes of the ALICE TRD,”
Nucl. Instrum. Meth. A **563** (2006) 310.
- [Bai06] J. Baines *et al.*,
“Heavy quarks (Working Group 3): Summary report,”
arXiv:hep-ph/0601164.
- [Bal00] A. Baldit *et al.*,
“Study of prompt dimuon and charm production with proton and heavy ion beams at the CERN SPS,”
CERN-SPSC-P-316;
- [Bar79] V. D. Barger, W. Y. Keung and R. J. N. Phillips,
“On Psi And Upsilon Production Via Gluons,”
Phys. Lett. B **91** (1980) 253.
- [Bed04] M. Bedjidian *et al.*,
“Hard probes in heavy ion collisions at the LHC: Heavy flavour physics,”
arXiv:hep-ph/0311048.
- [Bed07] M. Bedjidian and O. Kodolova,
“Quarkonia Measurements In Heavy-Ion Collisions In Cms,”
J. Phys. G **34** (2007) N143.
- [Beo98] S. Beole *et al.* [ALICE Collaboration],
“ALICE technical design report: Detector for high momentum PID,”
CERN-LHCC-98-19
- [Ber07] A. Bercuci, private communication.
- [Ber80] E. L. Berger and D. L. Jones,
“Inelastic Photoproduction Of J/Psi And Upsilon By Gluons,” Phys. Rev. D
23 (1981) 1521.
- [Bet02] R. R. Betts,
“Heavy-Ion Physics with CMS,”
J. Phys. G **34** (2007) S519.

- [Bia76] A. Bialas, M. Bleszynski and W. Czyz,
“Multiplicity Distributions In Nucleus-Nucleus Collisions At High-Energies,”
Nucl. Phys. B **111** (1976) 461.
- [Bos03] R. Esteve Bosch, A. Jimenez de Parga, B. Mota and L. Musa,
“The ALTRO chip: A 16-channel A/D converter and digital processor for gas detectors,”
IEEE Trans. Nucl. Sci. **50** (2003) 2460.
- [Bra94] E. Braaten and S. Fleming,
“Color octet fragmentation and the psi-prime surplus at the Tevatron,”
Phys. Rev. Lett. **74** (1995) 3327 [arXiv:hep-ph/9411365].
- [Bra03] R. Bramm *et al.* [ALICE Collaboration],
“High-level trigger system for the LHC ALICE experiment,”
Nucl. Instrum. Meth. A **502** (2003) 441.
- [Bra05] J. Bracinik [H1 and ZEUS Collaborations],
“Charm Fragmentation At Hera,”
PoS **HEP2005**, 064 (2006).
- [Bra04] N. Brambilla *et al.* [Quarkonium Working Group],
“Heavy quarkonium physics,”
arXiv:hep-ph/0412158.
- [Bra05] R. Bramm,
“ALTRO and TPC performance of ALICE,”
arXiv:physics/0501052.
- [Bro01] W. Broniowski and W. Florkowski, “Geometric relation between centrality and the impact parameter in relativistic heavy ion collisions,”
Phys. Rev. C **65** (2002) 024905 [arXiv:nucl-th/0110020].
- [Bro99] I.N. Bronstein, K.A. Semendjajew, G. Musiol, H. Mühlig,
“Taschenbuch der Mathematik”,
Verlag Harri Deutsch, 1999.
- [Brow90] F. R. Brown *et al.*,
“On the existence of a phase transition for QCD with three light quarks,”
Phys. Rev. Lett. **65** (1990) 2491.
- [Bru87] R. Brun, F. Bruyant, M. Maire, A. C. McPherson and P. Zancarini,
“GEANT3,”
CERN-DD/EE/84-1
- [Cac95] M. Cacciari, M. Greco, M. L. Mangano and A. Petrelli,
“Charmonium Production At The Tevatron,”
Phys. Lett. B **356** (1995) 553 [arXiv:hep-ph/9505379].

- [Cac96] M. Cacciari and M. Kramer,
“Color-Octet Contributions to J/ψ Photoproduction,”
Phys. Rev. Lett. **76** (1996) 4128 [arXiv:hep-ph/9601276].
- [Cac07] M. Cacciari,
“pQCD calculations of heavy quark and J/psi production,”
arXiv:hep-ph/0702211.
- [Car04] F. Carminati *et al.* [ALICE Collaboration],
“Alice: Physics Performance Report, Volume I”,
J. Phys. G **30** (2004) 1517.
- [Car04b] F. Carminati *et al.* [ALICE Collaboration],
“Alice: Physics Performance Report, Volume I”, table 3.30,
J. Phys. G **30** (2004) 1517.
- [Cas00] W. Cassing, E. L. Bratkovskaya and S. Juchem,
“Excitation functions of hadronic observables from SIS to RHIC energies,”
Nucl. Phys. A **674** (2000) 249 [arXiv:nucl-th/0001024].
- [Cho94] P. L. Cho and M. B. Wise,
“Spin Symmetry Predictions For Heavy Quarkonia Alignment,”
Phys. Lett. B **346** (1995) 129 [arXiv:hep-ph/9411303].
- [Cho95a] P. L. Cho and A. K. Leibovich,
“Color octet quarkonia production,”
Phys. Rev. D **53** (1996) 150 [arXiv:hep-ph/9505329].
- [Cho95b] P. L. Cho and A. K. Leibovich,
“Color-octet quarkonia production II,”
Phys. Rev. D **53** (1996) 6203 [arXiv:hep-ph/9511315].
- [Cms07] <http://cms.cern.ch/>
- [Cor02] P. Cortese *et al.* [ALICE Collaboration],
“ALICE: Addendum to the technical design report of the time of flight system (TOF),”
<https://edms.cern.ch/document/460192/1>
- [Cro01] P. Crochet and P. Braun-Munzinger,
“Investigation of background subtraction techniques for high mass dilepton physics,”
Nucl. Instrum. Meth. A **484** (2002) 564 [arXiv:nucl-ex/0106008].
- [Cro06] P. Crochet [ALICE Collaboration],
“(Di)lepton physics with ALICE,” Nucl. Phys. A **774** (2006) 915.

- [Dat04] S. Datta *et al.*,
"Behavior of Charmonium Systems after Deconfinement"
Phys. Rev. D **69**, (2004) 094507
- [Del00] G. Dellacasa *et al.* [ALICE Collaboration],
"ALICE technical design report of the time projection chamber,"
- [Del99] G. Dellacasa *et al.* [ALICE Collaboration],
"ALICE technical design report: Photon multiplicity detector (PMD),"
<https://edms.cern.ch/document/398931/1%20>
- [dEn03] D. d'Enterria,
"Hard scattering cross sections at LHC in the Glauber approach: From p p to
p A and A A collisions,"
arXiv:nucl-ex/0302016.
- [Dig01] S. Digal, P. Petreczky and H. Satz,
"String breaking and quarkonium dissociation at finite temperatures,"
Phys. Lett. B **514** (2001) 57 [arXiv:hep-ph/0105234].
- [Dig06] S. Digal, P. Petreczky and H. Satz, in preparation
- [Dol93] B. Dolgoshein,
"Transition radiation detectors,"
Nucl. Instrum. Meth. A **326** (1993) 434.
- [Eic78] E. Eichten, K. Gottfried, T. Kinoshita, K. D. Lane and T. M. Yan,
"Charmonium: The Model,"
Phys. Rev. D **17**, 3090 (1978) [Erratum-ibid. D **21**, 313 (1980)].
- [Eic80] E. Eichten,
"Recent Theoretical Developments For Heavy Quark - Anti-Quark Systems.
(Talk),"
Harvard Univ. Cambridge - HUTP-80-A084 (80,REC.JUN. 81) 14p
- [Eng80] J. Engels, F. Karsch, H. Satz and I. Montvay,
"High Temperature SU(2) Gluon Matter On The Lattice,"
Phys. Lett. B **101** (1981) 89.
- [Esk98] K. J. Eskola, V. J. Kolhinen and C. A. Salgado,
"The scale dependent nuclear effects in parton distributions for practical ap-
plications,"
Eur. Phys. J. **C9** (1999) 61.
- [Fab75] C. W. Fabjan and W. Struczinski,
"Coherent Emission Of Transition Radiation In Periodic Radiators,"
Phys. Lett. B **57** (1975) 483.

- [Fav01] C. Favuzzi, N. Giglietto, M. N. Mazziotta and P. Spinelli,
“Transition Radiation Detectors For Particle Physics And Astrophysics,”
Riv. Nuovo Cim. **24N5-6** (2001) 1.
- [Fas03] A. Fasso *et al.*,
“The physics models of FLUKA: Status and recent development,”
*In the Proceedings of 2003 Conference for Computing in High-Energy and
Nuclear Physics (CHEP 03), La Jolla, California, 24-28 Mar 2003, pp
MOMT005* [arXiv:hep-ph/0306267].
- [Fer98] E. G. Ferreira, C. Pajares and D. Sousa,
“String fusion model results on Pb Pb central collisions at SPS energies,”
Phys. Lett. B **422** (1998) 314.
- [Fer05] A. Ferrari, P. R. Sala, A. Fasso and J. Ranft,
“FLUKA: A multi-particle transport code (Program version 2005),”
- [Fod01] Z. Fodor and S. D. Katz,
“Lattice determination of the critical point of QCD at finite T and mu,”
JHEP **0203** (2002) 014 [arXiv:hep-lat/0106002].
- [Fri77] H. Fritzsche,
“Producing Heavy Quark Flavors In Hadronic Collisions: A Test Of Quantum
Chromodynamics,”
Phys. Lett. B **67** (1977) 217.
- [Fru00] R. Frühwirth *et al.*,
“Data analysis techniques for high-energy physics”,
Second edition, Cambridge Univ. Press (2000).
- [Gin45] V. Ginzburg, I. Frank,
“Radiation of a uniformly moving electron due to its transition from one
medium into another”,
Journ. Phys. USSR, v.9, **353**, (1945).
- [Gin80] V. L. Ginzburg and V. N. Tsytovich,
“On The Derivation Of The Transition Radiation Intensity,”
Phys. Lett. A **79** (1980) 16.
- [Gin79] V. L. Ginzburg and V. N. Tsytovich,
“Several Problems Of The Theory Of Transition Radiation And Transition
Scattering,”
Phys. Rept. **49** (1979) 1.
- [Gla70a] S. L. Glashow, J. Iliopoulos and L. Maiani,
“Weak Interactions with Lepton-Hadron Symmetry,”
Phys. Rev. D **2** (1970) 1285.

- [Gla87] R. J. Glauber,
“HIGH-ENERGY COLLISION THEORY,”
*In *Lo, S.Y. (ed.): Geometrical pictures in hadronic collisions**, 83-182. (see
Book Index)
- [Gla70b] R. J. Glauber and G. Matthiae,
“High-energy scattering of protons by nuclei,”
Nucl. Phys. B **21** (1970) 135.
- [Gla07] P. Glasel [ALICE TPC Collaboration],
“The ALICE TPC: An innovative device for heavy ion collisions at LHC,”
Nucl. Instrum. Meth. A **572** (2007) 64.
- [Gol59] P. Goldsmith, J. V. Jelley,
Phil. Mag. 4, **836**, 1959.
- [Gra03] L. Grandchamp, R. Rapp and G. E. Brown,
“In-medium effects on charmonium production in heavy-ion collisions,”
Phys. Rev. Lett. **92** (2004) 212301 [arXiv:hep-ph/0306077].
- [Gra07] N. Grau [ATLAS Collaboration],
“The Heavy Ion Physics Program with ATLAS at the LHC,”
arXiv:0706.1983 [nucl-ex].
- [Gro05] J. F. Grosse-Oetringhaus,
“Determination of the Physics Performance of the ALICE Central Barrel using a distributed GRID Computing Environment”,
Diploma thesis, IKP Münster (2005).
- [Gun07] T. Gunji [PHENIX Collaboration],
“Centrality dependence of J/ψ production in Au + Au and Cu + Cu collisions by the PHENIX experiment at RHIC,”
J. Phys. G **34** (2007) S749 [arXiv:nucl-ex/0703004].
- [Gyu94] M. Gyulassy and X. N. Wang,
“HIJING 1.0: A Monte Carlo program for parton and particle production in high-energy hadronic and nuclear collisions,”
Comput. Phys. Commun. **83** (1994) 307 [arXiv:nucl-th/9502021].
- [Har93] J. W. Harris [STAR Collaboration],
“The STAR experiment at the relativistic heavy ion collider,”
Nucl. Phys. A **566** (1994) 277C.
- [Haw93] C. M. Hawkes,
“Heavy flavor production at LEP: $\Gamma(b \text{ anti-}b)$, $\Gamma(c \text{ anti-}c)$ and heavy quark fragmentation,”
Prepared for Advanced Study Conference on Heavy Flavors, Pavia, Italy, 3-7 Sep 1993

- [Her77] S. W. Herb *et al.*,
“Observation of a dimuon resonance at 9.5-GeV in 400-GeV proton - nucleus collisions,”
Phys. Rev. Lett. **39**, 252 (1977).
- [Hug92] V. W. Hughes and G. K. Mallot,
“NA38 proposal,”
CERN-SPSLC-92-21. SPSLC-M-492, (1992).
- [Iid05] H. Iida *et al.*,
“ J/Ψ at high temperatures in anisotropic lattice QCD”
PoS, **LAT2005** (2005) 184
- [Iva06] M. Ivanov, I. Belikov, P. Hristov and K. Safarik,
“Track reconstruction in high density environment,”
Nucl. Instrum. Meth. A **566** (2006) 70.
- [Jac99] J. D. Jackson,
“Classical Electrodynamics”,
John Wiley Sons, Inc., 1999.
- [Kac03] O. Kaczmarek, S. Ejiri, F. Karsch, E. Laermann and F. Zantow,
“Heavy quark free energies and the renormalized Polyakov loop in full QCD,”
Prog. Theor. Phys. Suppl. **153** (2004) 287 [arXiv:hep-lat/0312015].
- [Kar95] F. Karsch,
“The Phase transition to the quark gluon plasma: Recent results from lattice calculations,”
Nucl. Phys. A **590** (1995) 367C [arXiv:hep-lat/9503010].
- [Kar05] F. Karsch, D. Kharzeev and H. Satz,
“Sequential charmonium dissociation,”
Phys. Lett. B **637** (2006) 75 [arXiv:hep-ph/0512239].
- [Kar07] V. Kartvelishvili [ATLAS Collaboration],
“Electron Bremsstrahlung Recovery In Atlas,”
Nucl. Phys. Proc. Suppl. **172** (2007) 208.
- [Kha96] D. Kharzeev, C. Lourenco, M. Nardi and H. Satz,
“A quantitative analysis of charmonium suppression in nuclear collisions,”
Z. Phys. C **74** (1997) 307 [arXiv:hep-ph/9612217].
- [Kis07] I. Kisel, S. Gorbunov,
www.gsi.de/documents/DOC-2007-May-14-1.pdf
- [Kol06] T. Kollegger,
“Search for upsilons in heavy-ion collisions with the STAR detector,”
PhD. thesis, University of Frankfurt (2006).

- [Kra06] F. Kramer,
“Studie zur Messung von Quarkonia mit dem ALICE-TRD und Aufbau eines Teststandes für seine Ausleskammern”,
Diploma thesis, University of Frankfurt (2006).
- [Kut80] J. Kuti, J. Polonyi and K. Szlachanyi,
“Monte Carlo Study Of SU(2) Gauge Theory At Finite Temperature,”
Phys. Lett. B **98** (1981) 199.
- [Leh04] T. Lehmann,
“Vorbereitungen für die Qualitätstests der ALICE-TRD-Kammern”,
Diplomarbeit, Universität Heidelberg (2004)
- [Leo94] W. R. Leo,
“Techniques for Nuclear and Particle Physics Experiments”,
Springer-Verlag, 1994.
- [Lhb07] <http://lhcb.web.cern.ch/lhcb/>
- [Lin03] V. Lindenstruth *et al.*,
“Online pattern recognition for the ALICE High Level Trigger,”
IEEE Trans. Nucl. Sci. **51** (2004) 3 [IEEE Trans. Nucl. Sci. **51** (2004) 383]
[arXiv:physics/0310052].
- [Lip04] C. Lippmann [ALICE TRD Collaboration],
“Position resolution and electron identification with prototypes of the ALICE TRD,”
Nucl. Instrum. Meth. A **535** (2004) 457.
- [Mah04] T. Mahmoud,
“Development of the readout chamber of the ALICE transition radiation detector and evaluation of its physics performance in the quarkonium sector,”
PhD. thesis, University of Heidelberg, 2004.
- [Man88] B. Mansoulie *et al.*,
“THE D0 TRANSITION RADIATION DETECTOR,”
Nucl. Instrum. Meth. A **265** (1988) 157.
- [Mar05] G. Martinez [ALICE Collaboration],
“Physics of the muon spectrometer of the ALICE experiment,”
J. Phys. Conf. Ser. **50** (2006) 361 [arXiv:hep-ex/0505021].
- [Mar06] G. Martinez,
“ALICE potential for open heavy-flavour physics”,
J. Phys. G: Nucl. Part. Phys., Proceedings Quark Matter 2006
- [Mat86] T. Matsui and H. Satz,
“J/psi Suppression by Quark-Gluon Plasma Formation,”
Phys. Lett. B **178** (1986) 416.

- [Mil07] M. L. Miller, K. Reyers, S. J. Sanders and P. Steinberg,
“Glauber modeling in high energy nuclear collisions,”
arXiv:nucl-ex/0701025.
- [Mon] <http://monarc.web.cern.ch/MONARC>
- [Mor98] D. P. Morrison *et al.* [PHENIX Collaboration],
“The PHENIX experiment at RHIC,”
Nucl. Phys. A **638** (1998) 565 [arXiv:hep-ex/9804004].
- [Mus03] L. Musa [ALICE Collaboration],
“The Time Projection Chamber For The Alice Experiment,”
Nucl. Phys. A **715** (2003) 843.
- [Nic03] A. Nicolaucig, M. Ivanov and M. Mattavelli,
“Lossy compression of TPC data and trajectory tracking efficiency for the
ALICE experiment,”
Nucl. Instrum. Meth. A **500** (2003) 412.
- [Rap05] R. Rapp,
“Quark coalescence and charm(onium) in QGP,”
Eur. Phys. J. C **43** (2005) 91 [arXiv:hep-ph/0502208].
- [Sat05] H. Satz,
“Colour deconfinement and quarkonium binding,”
J. Phys. G **32** (2006) R25 [arXiv:hep-ph/0512217].
- [Sat06a] H. Satz,
“Quarkonium binding and dissociation: The spectral analysis of the QGP,”
Nucl. Phys. A **783**, 249 (2007) [arXiv:hep-ph/0609197].
- [Sat06b] H. Satz,
“Charm and beauty in a hot environment,”
arXiv:hep-ph/0602245.
- [Sax06] D. H. Saxon,
“Particle production and fragmentation at HERA,”
arXiv:hep-ex/0601013.
- [Sco07] E. Scomparin [NA60 Collaboration],
“J/psi production in In In and p A collisions,”
arXiv:nucl-ex/0703030.
- [Shu03] P. Shukla,
“The Glauber model and the heavy ion reaction cross section,”
Phys. Rev. C **67** (2003) 054607 [arXiv:nucl-th/0302030].

- [Shu78] E. V. Shuryak,
“Quark-Gluon Plasma And Hadronic Production Of Leptons, Photons And
Psions,”
Phys. Lett. B **78** (1978) 150 [Sov. J. Nucl. Phys. **28** (1978 YAFIA,28,796-
808.1978) 408.1978 YAFIA,28,796].
- [Sjo06] T. Sjostrand, S. Mrenna and P. Skands,
“PYTHIA 6.4 physics and manual,”
JHEP **0605** (2006) 026 [arXiv:hep-ph/0603175].
- [Sto07] R. Stock, private communication.
- [Sus79] L. Susskind,
“Lattice Models Of Quark Confinement At High Temperature,”
Phys. Rev. D **20** (1979) 2610.
- [The05] R. L. Thews and M. L. Mangano,
“Momentum spectra of charmonium produced in a quark-gluon plasma,”
Phys. Rev. C **73** (2006) 014904 [arXiv:nucl-th/0505055].
- [Ume00] T. Umeda, R. Katayama, O. Miyamura and H. Matsufuru,
“Study of charmonia near the deconfining transition on an anisotropic lattice
with O(a) improved quark action,”
Int. J. Mod. Phys. A **16** (2001) 2215 [arXiv:hep-lat/0011085].
- [Vog99] R. Vogt,
“Relation of hard and total cross sections to centrality,”
Heavy Ion Phys. **9** (1999) 339 [arXiv:nucl-th/9903051].
- [Vog01] R. Vogt [Hard Probe Collaboration],
“The A dependence of open charm and bottom production,”
Int. J. Mod. Phys. E **12** (2003) 211 [arXiv:hep-ph/0111271].
- [Vog04] R. Vogt,
“Open and hidden charm production at RHIC and LHC,”
J. Phys. G **31** (2005) S773 [arXiv:hep-ph/0412303].
- [Wil07] A. Wilk, private communication.
- [Wil08] A. Wilk, thesis in preparation.
- [Wos07] B. Wosiek [ATLAS Collaboration],
“Heavy ion physics with the ATLAS detector,”
Acta Phys. Polon. B **38** (2007) 1047.
- [Woo46] R.D. Woods and D.S. Saxon,
Phys. Rev. **95** 577 (1954).

- [Yan06] L. Yan, P. Zhuang and N. Xu,
“Competition between J/psi suppression and regeneration in quark-gluon
plasma,”
Phys. Rev. Lett. **97** (2006) 232301 [arXiv:nucl-th/0608010].
- [Yao06] W. M. Yao *et al.* [Particle Data Group],
“Review of particle physics,”
J. Phys. G **33** (2006) 1.

Acknowledgements – Danksagung

Mein erster und auch größter Dank geht an meinen Betreuer Christoph Blume. Besonders danke ich Ihm, für sein Vertrauen, seine guten Ratschläge und die Bereitschaft auf die speziellen Erfordernisse eines Doktoranden mit Familie einzugehen. Daran schließt sich direkt mein Dank an Harald Appelshäuser an, der ebenso bereit war, mich und meine Familie besonders während der letzten zwei Jahre zu unterstützen. Auch ihm verdanke ich viele Anregungen und wertvolle Ratschläge in Bezug auf meine Arbeit.

Danke an Matthias Hartig, der mich nun schon (mit Pausen) seit meines Diploms begleitet und der mir immer gute Ratschläge geben konnte. Mal sehen, wann wir wieder in einem Büro sitzen.

Der nächste Dank geht an alle meine Frankfurter Kollegen, besonders erwähnen möchte ich hier das TRD-Team: Werner Amend, Arnold Wiesenäcker, Hannelore Hinke, Frederick Kramer, Michael Kliemant und die vielen studentischen Hilfskräfte ohne die einfach nichts laufen würde.

Danke für die angenehme Atmosphäre und viele interessante Diskussionen in Frankfurt an: Tom Dietel, Mateusz Ploskon, Dariusz Antonczyk, Peter Dinkelaker, Thorsten Kollegger, Andreas Wetzler, Constantin Loizides, Roland Bramm, Boris Wagner, Dominik Wegerle, Stefan Kniege, Simone Schuchmann, Andreas Fick, Konstantin Antipin, Tim Schuster, Claudia Strabel, Reinhard Stock, Rainer Renfordt, Marek Gadzicki, Herbert Ströbele und Milica Utvic.

Vielen Dank an Henner Büsching für die Korrektur so mancher sprachlichen Ungenauigkeit.

Für die Unterstützung beim Aufbau des TRD-Labors möchte ich mich neben meinen Frankfurter Kollegen besonders bei Clemens Adler, Jörg Hehner, Heinz Daus und Herbert Stelzer bedanken.

Vielen Dank an Peter Eschenbrenner, Martina Lang, Bettina Kömpel, Claudia Freudenberger und Ulrich Köpf für die Hilfe bei allen möglichen organisatorischen Problemen.

Außerhalb Frankfurts geht mein Dank an alle Kollegen von ALICE, hierbei ein besonderes Dankeschön für die vielen Anregungen, Korrekturen und Hilfestellungen an Tariq Mahmoud, Ken Oyama, Anton Andronic, Johanna Stachel, Jan

Fiete Grosse-Oetringhaus, Philippe Crochet, Gines Martinez, Silvia Masciocchi, Sergey Gorbunov, Christian Schmidt, Kai Schweda und Christian Lippmann.

Diese ganze Arbeit sowie mein Studium wäre niemals möglich gewesen ohne die beständige und bedingungslose Unterstützung durch meine Eltern, dafür und noch für viel mehr, Danke.

Mein letzter Dank geht an meine wunderbare Frau und unsere kleine Υ -Familie, Hannah, Jakob und Clemens. Ohne euch wäre ich nicht der, der ich bin, ihr macht einen glücklichen Menschen aus mir und dafür kann ich euch nicht genug danken!